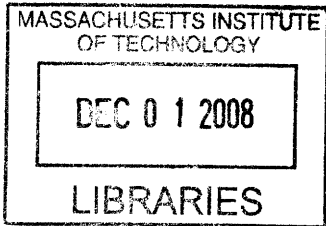


# Development of Novel Diagnostics and Therapeutics for Amyotrophic Lateral Sclerosis

by

**Seth A. Townsend**

Bachelor of Science, Biomedical Engineering  
Johns Hopkins University, 2004



Submitted to the Biological Engineering Department  
in partial fulfillment of the requirements for the degree of

**Doctorate of Philosophy in Biological Engineering**

at the

**Massachusetts Institute of Technology**

June, 2008

© 2008 Massachusetts Institute of Technology  
All rights reserved

Signature of Author .....  
Seth A. Townsend  
Biological Engineering Department

Certified by .....  
Robert Langer, ScD  
Thesis Supervisor

Certified by .....  
Robert H. Brown, MD-DPhil  
Thesis Supervisor

Accepted by .....  
Douglas A. Lauffenburger, PhD  
Director, Biological Engineering Department

**ARCHIVES**

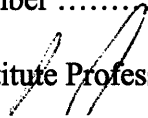


This doctoral thesis has been examined by a committee of the Biological Engineering Department as follows:

Chairperson, Graduate Thesis Committee .....  
Darrell J. Irvine, PhD  
Eugene Bell Associate Professor of Tissue Engineering



Thesis Supervisor, Committee Member .....  
Robert Langer, ScD  
Institute Professor, Massachusetts Institute of Technology



Thesis Committee Member .  
.....  
Robert H. Brown, MD-DPhil  
Director, Day Neuromuscular Laboratory, Massachusetts General Hospital  
Professor, Harvard Medical School



# Development of Novel Diagnostics and Therapeutics for Amyotrophic Lateral Sclerosis

by

**Seth A. Townsend**

Submitted to the Biological Engineering Department in partial fulfillment of the requirements for the degree of Doctorate of Philosophy in Biological Engineering

## Abstract

Amyotrophic lateral sclerosis (ALS) is a neurodegenerative disease with diagnostics and treatments that are ineffective at stopping the progression. This thesis examines new ways of both diagnosing and treating ALS, including 1) a gadolinium tetanus toxin C fragment (Gd-TTC) biomarker for axonal retrograde transport, 2) TTC-conjugated biodegradable nanoparticles, and 3) poly(glycerol-co-sebacate) acrylate (PGSA) and 3D scaffolds for human embryonic stem cell (hESC) and neuronal encapsulation.

A Gd-TTC conjugate was developed and characterized that was shown to be highly visible under MRI and preserved the functionality of the native TTC protein *in vitro*. Live animal MRI imaging and immunofluorescent staining of the spinal cord showed that the conjugate was transported to the central nervous system (CNS) and localized in motor neurons. H&E staining and biodistribution studies showed that Gd-TTC was well tolerated and bioavailable. Quantification of MRI and staining images showed that Gd-TTC was retrograde transported and that this rate decreased during the disease progression of ALS in a transgenic mouse model, suggesting that Gd-TTC could be used as a biomarker for neurodegenerative diseases.

TTC-conjugated nanoparticles were developed by synthesizing PLGA-PEG-biotin and using biotin binding proteins (avidin, streptavidin, and neutravidin) to specifically conjugate TTC to the nanoparticle surface. TTC nanoparticles were shown to selectively target neurons and not other cell types *in vitro*. Subsequent *in vivo* experiments showed that nanoparticles were well tolerated and that TTC was co-localized with neurons unilaterally, suggesting that TTC-conjugated nanoparticles may be a useful drug delivery system.

Porous PGSA scaffolds were prepared and characterized by porosity, swelling, mass loss, toxicity and mechanical properties, and subsequently used to encapsulated hESC and neuroblastoma cells *in vitro*. Neuroblastoma cells proliferated and formed matrix fibrils, and fluorescent staining of undifferentiated hESCs showed the presence of all three germ layers. *In vivo* experiments showed that porous PGSA scaffolds were well-tolerated and promoted vascular ingrowths.

Thesis Supervisors: Robert Langer, ScD (Institute Professor, MIT) and Robert H. Brown, MD-DPhil (Director Day Neuromuscular Laboratory, MGH, and Professor, Harvard Medical School)

## Acknowledgements

I would like to thank the many people who have supported me and who have made this thesis successful. I would like to thank my thesis advisors and committee members, Bob Langer, Robert Brown, and Darrell Irvine, who have provided the right balance of freedom to conduct independent experiments, and the guidance to carry them out, and who have shown me an example of great leadership and science. I would also like to thank my advisors from my undergraduate studies at Johns Hopkins, Art Shoukas and Dan Berkowitz, who have helped me to develop the foundations that I took with me to graduate school, and who continue to be great mentors and role models. I would like to thank the many people who I have worked with in the Langer lab: Frank Gu and Ben Tepy for their help with nanoparticles and targeted delivery, Greg Zugates and Jason Fuller for all of our discussion, Sharon Gerecht who taught me about stem cells, Frank Alexis and Will Neely for help with the HPLC, Karen Daniel for help with MRI, Mikhail Shapiro for help with protein gels, Dan Anderson for guidance, and all of the others in the lab who have led to this work. I would like to thank the undergraduate and graduate students who have worked with me: Heather Pressler for help with cell culture, Hannah Zhou for HPLC, Martin Schulz for help with staining and Matrigel hESC encapsulation, and Gilad Evrony, who is innovative, creative, and who took a lead role in a number of projects that we worked on together. I would also like to thank my family: Martha Loeffler, my mother; Teresa Townsend, my sister; and John and Cecelia Loeffler, my grandparents, who have supported me all these years and who have given me an interest in learning and science. I would like to thank you, for being there in good times and bad, and for giving me the strength to push on through hard times in my thesis and personal life, and for always standing by my side. I couldn't have done this without you!

As with any science today, we are moving into an age of strong collaboration in which interdisciplinary teams work together and solve high impact problems. It is out of this approach that the field of biological engineering has emerged. My goal is that this thesis will make lasting contributions to science and clinical medicine. To this end, I have worked as an integral part of a highly multi-disciplinary team of researchers. Some of the work in this thesis has been published in peer reviewed journals, and more is in the form of manuscripts. I want to recognize the contribution of each researcher that has taken part in this work and this goal with me. I have listed the contribution of each researcher in the Appendix A, for both published work and manuscripts that are planned to be submitted.

2.3.9 Transcardial perfusion and spinal cord isolation.....	41
2.3.10 14T MRI spinal cord imaging (ex vivo) .....	41
2.3.11 Hematoxylin and Eosion staining .....	41
2.3.12 Immunohistochemistry staining for TTC and NeuN.....	42
2.3.13 Biodistribution (in vivo) and neutron irradiation analysis .....	42
2.3.14 Image analysis and quantification .....	43
2.4.0 RESULTS AND DISCUSSION .....	44
2.4.1 Conjugation of gadolinium to TTC .....	44
2.4.2 Characterization of Magnetic Relaxivity .....	44
2.4.3 Neuronal binding of Gd-TTC in vitro .....	45
2.4.4 Live animal 9.4T MRI imaging .....	46
2.4.5 Ex Vivo 14T MRI imaging (high resolution).....	47
2.4.6 Immunohistochemistry and Hematoxylin/Eosion Staining.....	47
2.4.7 Biodistribution (in vivo).....	48
2.4.8 Gd-TTC as a Biomarker for ALS (in vivo).....	50
2.5.0 CONCLUSIONS.....	52
2.6.0 ACKNOWLEDGEMENTS .....	52
2.7.0 FIGURES AND FIGURE LEGENDS.....	53
2.7.1 Figure 1 – Synthesis and characterization of Gd-TTC .....	53
2.7.2 Figure 2 –MRI imaging of Gd-TTC injected wildtype mice.....	57
2.7.3 Figure 3 – Immunohistological staining for TTC .....	59
2.7.4 Figure 4 – Haematoxylin and Eosin Staining and in vivo biodistribution.....	63
2.7.5 Figure 5 – Gd-TTC as a biomarker for retrograde transport in ALS mice.....	65

**CHAPTER 3: TETANUS TOXIN C FRAGMENT CONJUGATED NANOPARTICLES FOR TARGETED DRUG DELIVERY TO NEURONS <sup>85</sup> ..... 67**

3.1.0 ABSTRACT .....	67
3.2.0 INTRODUCTION .....	68
3.3.0 METHODS .....	70
3.3.1 Preparation of PLGA-PEG-COOH .....	70
3.3.2 NMR analysis.....	70
3.3.3 Preparation of nanoparticles (nanoprecipitation).....	70
3.3.4 Protein attachment to nanoparticles.....	71
3.3.5 Preparation of BSA-FITC and TTC-FITC .....	72
3.3.6 Biotinylation of BSA and TTC.....	72
3.3.7 Biotinylation quantification .....	72
3.3.8 Nanoparticle characterization and schematic .....	73
3.3.9 Flow cytometry.....	73
3.3.10 Cell culture.....	74
3.3.11 Statistics .....	74
3.4.0 RESULTS AND DISCUSSION .....	75
3.4.1 Biotin binding proteins for nanoparticle conjugation.....	75
3.4.2 NMR characterization.....	75
3.4.3 Protein conjugation to nanoparticles.....	76
3.4.4 Comparison of different biotin binding proteins .....	78
3.4.5 Protein functionality and specificity .....	79
3.4.6 Nanoparticle aggregation .....	79
3.4.7 In vitro cell specificity.....	80
3.4.8 Characterization of nanoparticles .....	81
3.5.0 CONCLUSIONS.....	82
3.6.0 ACKNOWLEDGEMENTS .....	82
3.7.0 TABLES AND FIGURES.....	83
3.7.2 Figure 2: Protein conjugation to PLGA-PEG-biotin nanoparticles.....	85
3.7.3 Figure 3: TTC protein functionality and nanoparticle size optimization.....	87
3.7.4 Figure 4: In vitro cell binding of TTC-conjugated nanoparticles.....	89
3.7.5 Table 1: Nanoparticle binding to cells.....	92

# Table of Contents

<b>ABSTRACT</b> .....	<b>5</b>
<b>ACKNOWLEDGEMENTS</b> .....	<b>6</b>
<b>TABLE OF CONTENTS</b> .....	<b>7</b>
<b>CHAPTER 1: INTRODUCTION</b> .....	<b>13</b>
1.1.0 AMYOTROPHIC LATERAL SCLEROSIS.....	13
1.1.1 Background.....	13
1.1.2 Causes.....	13
1.1.3 Symptoms .....	14
1.1.4 Diagnostics .....	15
1.1.5 Treatments .....	15
1.1.6 Experimental approaches .....	16
1.2.0 MAGNETIC RESONANCE IMAGING .....	17
1.2.1 Overall background.....	17
1.2.2 Methods of Imaging.....	18
1.2.3 Research involving ALS.....	19
1.3.0 DRUG DELIVERY .....	20
1.3.1 Background.....	20
1.3.2 Biodegradable Polymers.....	20
1.3.3 Blood Brain Barrier (BBB).....	21
1.3.4 Microparticles and nanoparticles.....	22
1.4.0 RETROGRADE TRANSPORT .....	23
1.4.1 Background.....	23
1.4.2 Molecules that use retrograde transport.....	23
1.4.3 Use as a delivery vehicle.....	24
1.4.4 Retrograde transport and ALS.....	24
1.5.0 STEM CELLS .....	25
1.5.1 Background and derivation.....	25
1.5.2 Ethical considerations.....	26
1.5.3 Differentiation (including neuronal).....	26
1.5.4 Undifferentiation.....	27
1.5.5 Applications of stem cells for ALS .....	28
1.5.6 Hydrogels and scaffolds.....	29
1.6.0 OVERALL GOALS.....	31
1.7.0 FORMAT OF THIS DOCUMENT .....	32
<b>CHAPTER 2: DEVELOPMENT OF A GADOLINIUM TETANUS TOXIN C FRAGMENT CONJUGATE BIOMARKER FOR <i>IN VIVO</i> MRI VISUALIZATION OF AXONAL RETROGRADE TRANSPORT IN AN AMYOTROPHIC LATERAL SCLEROSIS MOUSE MODEL</b> .....	<b>33</b>
2.1.0 ABSTRACT .....	33
2.2.0 INTRODUCTION .....	34
2.3.0 METHODS .....	37
2.3.1 Synthesis of Gd-TTC and Gd-BSA .....	37
2.3.2 Protein characterization .....	37
2.3.3 Culture of N18-RE-105 neuroblastoma cells.....	38
2.3.4 Cell binding assay and flow cytometry .....	38
2.3.5 MRI relaxivity measurements.....	39
2.3.6 MRI imaging of Protein Contrast (1.5T).....	39
2.3.7 Animal study approval and injections.....	40
2.3.8 9.4T MRI live animal imaging (in vivo).....	40



3.7.6 Table 2: Nanoparticle characterization.....	93
<b>CHAPTER 4: A POROUS PHOTOCURABLE ELASTOMER FOR CELL ENCAPSULATION AND CULTURE</b> <sup>172</sup> .....	<b>95</b>
4.1.0 ABSTRACT .....	95
4.2.0 INTRODUCTION .....	96
4.3.0 METHODS .....	98
4.3.1 Cell culture and media.....	98
4.3.2 Synthesis of PGSA.....	98
4.3.3 Formation of porous PGSA scaffolds .....	99
4.3.4 In vitro swelling and material loss.....	99
4.3.5 Mechanical tests.....	100
4.3.6 In vitro toxicity.....	101
4.3.7 Environmental Scanning Electron Microscope (ESEM).....	101
4.3.8 Porosity analysis.....	102
4.3.9 In vivo biocompatibility .....	102
4.3.10 Histology.....	103
4.3.11 Immunofluorescence .....	103
4.3.12 Inflammatory response and in-growth characterization.....	103
4.3.13 Statistics .....	104
4.4.0 RESULTS.....	105
4.4.1 Characterization of PGSA scaffold porosity.....	105
4.4.2 Swelling and mass loss properties .....	105
4.4.3 Mechanical property characterization.....	106
4.4.4 Toxicity.....	106
4.4.5 N18-RE-105 cell encapsulation and culture (in vitro).....	107
4.4.6 Human embryonic stem cell encapsulation (in vitro) .....	108
4.4.7 Human ESC proliferation and differentiation (in vitro).....	108
4.4.8 Biocompatibility (in vivo).....	109
4.4.9 Scaffold ingrowth (in vivo).....	109
4.5.0 DISCUSSION .....	110
4.6.0 CONCLUSIONS.....	112
4.7.0 ACKNOWLEDGEMENTS .....	112
4.8.0 TABLE AND FIGURE CAPTIONS .....	113
4.8.1 Figure 1: Porous PGSA .....	113
4.8.2 Figure 2: Swelling, mass loss, and mechanical characterization.....	113
4.8.3 Figure 3: Toxicity of PGSA monomer and glycerol.....	115
4.8.4 Figure 4: Cell encapsulation within Porous PGSA .....	117
4.8.5 Figure 5: Differentiated hESCs .....	119
4.8.6 Figure 6: In vivo Biocompatibility.....	121
4.8.7 Figure 7: In vivo ingrowth.....	123
4.8.8 Table 1: Pore Characterization .....	125
4.8.9 Table 2: Mechanical properties of porous PGSA .....	125
4.8.10 Table 3: Compressive properties of porous PGSA .....	125
<b>CHAPTER 5: FUTURE DIRECTIONS.....</b>	<b>127</b>
5.1.0 ALS BIOMARKERS .....	127
5.2.0 DRUG DELIVERY TO THE CNS.....	128
5.3.0 NEURONAL STEM CELLS.....	129
<b>APPENDIX SUMMARY .....</b>	<b>131</b>
<b>APPENDIX A: AUTHORSHIP ON PUBLICATIONS AND MANUSCRIPTS.....</b>	<b>139</b>
<b>APPENDIX B: TETANUS TOXIN C CONJUGATED NANOPARTICLES FOR <i>IN VIVO</i> DELIVERY TO THE CENTRAL NERVOUS SYSTEM.....</b>	<b>141</b>
A.B.1.0 ABSTRACT.....	141

A.B.2.0 INTRODUCTION.....	142
A.B.3.0 METHODS.....	146
<i>A.B.3.1: Preparation of nanoparticles</i> .....	146
<i>A.B.3.2 Measurement of encapsulation efficiency and release kinetics</i> .....	146
<i>A.B.3.3 Animal study approval and injections</i> .....	147
<i>A.B.3.4 Transcardial perfusion and spinal cord isolation</i> .....	147
<i>A.B.3.5 Hematoxylin and Eosion staining</i> .....	148
<i>A.B.3.6 Immunohistochemistry staining for TTC and NeuN</i> .....	148
<i>A.B.3.7 Cell culture and nanoparticle incubations</i> .....	149
<i>A.B.3.8 Nanoparticle biodistribution (in vivo) and tissue preparation/processing</i> .....	150
A.B.4.0 RESULTS AND DISCUSSION.....	151
<i>A.B.4.1 Riluzole release kinetics from nanoparticles</i> .....	151
<i>A.B.4.2 Biocompatibility of TTC-conjugated nanoparticles</i> .....	151
<i>A.B.4.3 In vivo transport of TTC-conjugated nanoparticles</i> .....	152
<i>A.B.4.4 Localization of TTC-conjugated nanoparticles in motorneurons</i> .....	152
<i>A.B.4.5 Nanoparticle biodistribution (in vivo)</i> .....	153
A.B.5.0 CONCLUSIONS.....	154
A.B.6.0 ACKNOWLEDGEMENTS.....	155
A.B.7.0 FIGURES AND FIGURE LEGENDS.....	157
<i>A.B.7.1 Figure 1 – Riluzole nanoparticle release kinetics</i> .....	157
<i>A.B.7.2 Figure 2 – Haematoxylin and eosin staining of lumbar spinal cord sections following BSA-NP and TTC-NP injections</i> .....	159
<i>A.B.7.3 Figure 3 – Retrograde transport for TTC-conjugated nanoparticles to the lumbar spinal cord</i> .....	161
<i>A.B.7.4 Figure 4 – Immunohistological staining for TTC</i> .....	163
<i>A.B.7.5 Figure 5 – In vivo biodistribution</i> .....	165

**APPENDIX C: HUMAN EMBRYONIC STEM CELL ENCAPSULATION IN MATRIGEL FOR NEURONAL DIFFERENTIATION..... 167**

A.C.1.0 ABSTRACT.....	167
A.C.2.0 INTRODUCTION.....	168
A.C.3.0 METHODS.....	170
<i>A.C.3.1 Cell culture and media</i> .....	170
<i>A.C.3.2 Condition media production</i> .....	170
<i>A.C.3.3 Matrigel hESC encapsulation and fixation</i> .....	171
<i>A.C.3.4 Hematoxylin and Eosion (H&amp;E) staining</i> .....	171
<i>A.C.3.5 Immunofluorescence</i> .....	172
<i>A.C.3.6 Immunohistochemistry and peroxidase staining</i> .....	172
<i>A.C.3.7 Flow cytometry</i> .....	173
A.C.4.0 RESULTS AND DISCUSSION.....	174
<i>A.C.4.1 hESC encapsulation within Matrigel and morphology</i> .....	174
<i>A.C.4.2 Expression of differentiation markers after Matrigel encapsulation</i> .....	175
<i>A.C.4.3 Immunohistochemistry and neuronal differentiation</i> .....	175
<i>A.C.4.4 Flow cytometry of differentiation and neuronal markers</i> .....	176
A.C.5.0 CONCLUSIONS.....	177
A.C.6.0 ACKNOWLEDGEMENTS.....	177
A.C.7.0 FIGURE LEGENDS.....	178
<i>A.C.7.1 Figure 1 – Light microscopy of hESC encapsulated within Matrigel</i> .....	179
<i>A.C.7.2 Figure 2 – hESC encapsulated within Matrigel</i> .....	181
<i>A.C.7.3 Figure 3 – hESC encapsulated within Matrigel of different sizes affecting morphology</i> .....	183
<i>A.C.7.4 Figure 4 – Germ layer staining of hESC encapsulated within Matrigel after 4 days in culture</i> .....	185
<i>A.C.7.5 Figure 5 – Neuronal staining of hESC encapsulated in Matrigel</i> .....	187
<i>A.C.7.6 Figure 6 – Immunofluorescent and immunohistochemistry staining of hESC in Matrigel</i> ..	189
<i>A.C.7.7 Figure 7 – Flow cytometry of single cell hESC populations after Matrigel culture</i> .....	191

<b>APPENDIX D: CHEMICAL STRUCTURES AND PREDICTED NMR.....</b>	<b>193</b>
<i>Figure 1: PLGA-PEG-Biotin and PLGA-PEG-Biotin structure.....</i>	<i>193</i>
<i>Figure 2: NHS, EDC, and Sulfo-NHS Structure.....</i>	<i>193</i>
<i>Figure 3: Sulfo-NHS-Biotin and NH2-PEG-Biotin Structure.....</i>	<i>194</i>
<i>Figure 4: NH2-PEG-Biotin theoretical NMR.....</i>	<i>194</i>
<i>Figure 5: PLGA-COOH Theoretical NMR.....</i>	<i>195</i>
<i>Figure 6: PLGA-PEG-COOH Theoretical NMR.....</i>	<i>195</i>
<i>Figure 7: NH2-PEG-COOH Theoretical NMR.....</i>	<i>196</i>
<i>Figure 8: PLGA-PEG-Biotin Theoretical NMR.....</i>	<i>196</i>
<i>Figure 9: Biotin: Theoretical NMR.....</i>	<i>197</i>
<i>Figure 10: Summary predicted polymer NMR.....</i>	<i>197</i>
<b>APPENDIX E: SYNTHESIS OF PLGA-PEG-BIOTIN .....</b>	<b>198</b>
<b>APPENDIX F: SCHEMATICS OF MRI CONTRAST AGENT BIOMARKERS.....</b>	<b>199</b>
<b>APPENDIX G: ADDITIONAL ANALYSIS OF MRI RELAXIVITY .....</b>	<b>199</b>
<b>APPENDIX H: 4.7T MRI IMAGING (IN VIVO).....</b>	<b>201</b>
<b>APPENDIX I: 9.4T MRI IMAGING (IN VIVO).....</b>	<b>203</b>
<b>APPENDIX J: SPINAL CORD STAINING OF TTC TRANSPORT (EX VIVO).....</b>	<b>205</b>
<b>APPENDIX K: ADDITIONAL ANALYSIS OF IHC AND MRI TRANSPORT QUANTIFICATION .....</b>	<b>207</b>
<b>APPENDIX L: NANOPARTICLE PREPARATIONS TO CONTROL SIZE .....</b>	<b>209</b>
<b>APPENDIX M: IMMUNOHISTOCHEMISTRY STAINING OF TTC-CONJUGATED NANOPARTICLES .....</b>	<b>211</b>
<b>APPENDIX N: NANOPARTICLE PROTEIN ENCAPSULATION AND CONJUGATION.....</b>	<b>213</b>
<b>APPENDIX O: FLOW CYTOMETRY ANALYSIS OF BIOTIN BINDING PROTEINS.....</b>	<b>215</b>
<b>APPENDIX P: CELL BINDING OF TTC-CONJUGATED NANOPARTICLES USING NHS/EDC .....</b>	<b>215</b>
<b>APPENDIX Q: TTC NANOPARTICLES BINDING TO PROSTATE CANCER.....</b>	<b>217</b>
<b>APPENDIX R: TTC BINDING TO NEUROBLASTOMAS WITH POLYSTYRENE NANOPARTICLES .....</b>	<b>219</b>
<b>APPENDIX T: DIFFUSION THROUGH HYDROGELS .....</b>	<b>221</b>
<b>APPENDIX T: CANCER STEM CELLS .....</b>	<b>223</b>
<b>APPENDIX U: REFERENCES .....</b>	<b>224</b>



## **Chapter 1: Introduction**

### **1.1.0 Amyotrophic Lateral Sclerosis**

#### *1.1.1 Background*

Amyotrophic lateral sclerosis (ALS, or Lou Gehrig's disease) is a neurodegenerative disease affecting both upper and lower motor neurons in the central nervous system. There is currently no cure for ALS, and most people who are diagnosed with ALS usually will die within 3-5 years after loss of motor function and muscle atrophy. Approximately 5000 new cases of ALS are made each year in the US, primarily in patients who are older than age 50. Despite the low incidence rate of the disease, ALS has gained much public attention and is more well known by most people than other neurodegenerative diseases, largely because several famous people have been diagnosed with ALS (Lou Gehrig and Stephen Hawking, among others). Because of this, funding for basic science and clinical trials research is available with the goal of someday finding a cure to ALS.

#### *1.1.2 Causes*

The causes of ALS are not well understood. However, it is known that in a small fraction of patients (approximately 10%), ALS is caused by a genetic mutation. Of these cases that are caused genetically, most are recessively inherited, and approximately 20% of these cases are caused by mutations in the superoxide dismutase I (SOD1) gene. SOD1 is responsible for maintaining free radical and oxidation states, and for this reason, some of the current clinical trials that are being conducted have targeted these pathways.

This knowledge of SOD1 mutations has led to the generation of a number of transgenic animal models for ALS, including the G93A mouse model, a rat model, and an earthworm model. However, in the vast majority of cases of ALS, the cause of the disease is not known. Researchers suggest that environmental factors and apoptosis could play a role as possible risk factors for the disease, but more research is needed to understand relative and absolute contributions.

### *1.1.3 Symptoms*

The early symptoms of ALS often go unnoticed or are misdiagnosed as common signs of aging. These symptoms include the loss in strength and balance most often in the arms and legs, reduced balance and coordination, and difficulty walking. Less common early symptoms include a difficulty in speech and swallowing.

Late stage symptoms of ALS include total loss of motor function in the limbs, inability to walk, and reduced activity in other motor neuron function. This leads to difficulty swallowing, eating, talking, and breathing in patients with late stage ALS. Visible symptoms of the disease are associated with secondary symptoms such as muscle atrophy. However, ALS is not thought to affect other critical systems, and patients maintain their cognitive ability throughout the disease. For this reason, treatments that improve motor neuron function could have significant impacts on patient quality of life.

#### *1.1.4 Diagnostics*

A diagnosis of ALS is usually made after early symptoms have been present for extended periods. This is partially because ALS is rare, and many doctors misdiagnose the symptoms as signs of aging. An accurate and reliable diagnosis is further complicated because there is no single test for ALS. Instead, it is usually made by ruling out other conditions by conducting a series of tests. These tests include evaluating nerve conduction velocity, using an MRI to eliminate cancer as a possibility, and muscle or nerve biopsy. Even with these tests, the results and a series of physical examinations is used to make a final diagnosis, and often a patient has been seen by multiple neurologists before a diagnosis is made. It is clear that more effective and earlier diagnostics would help

#### *1.1.5 Treatments*

There is currently only one FDA-approved therapeutic for ALS, Riluzole, that prolongs survival by approximately six months in most patients. Riluzole is only successful in delaying the progression of ALS, but it is not a cure. It is largely believed that the mechanism of riluzole includes a decrease in the amount of glutamate released by neurons. Many researchers suggest that an earlier diagnostic test would enable more successful treatments. Additionally, if we better understand the cause of ALS and the mechanisms for progression, therapeutics could be developed to target certain pathways. Unfortunately, despite the large number of completed and ongoing trials, most of the completed clinical trials have been largely unsuccessful.

In addition to pharmaceutical therapeutics, ALS therapies rely largely on supportive care including breathing assistance and physical therapy. This treatment includes the use of mechanical assistance such as walkers and braces, as well as prescription therapeutics including drugs to reduce muscle fatigue. During late stage ALS, devices that assist with voice communication can be used as patients often lose their ability to talk coherently, as well as devices that assist with breathing such as respiratory ventilators. It is widely viewed that this care does not prevent disease progression but instead improves patient quality of life.

#### *1.1.6 Experimental approaches*

There are a number of experimental approaches that are being studied as possible treatments for ALS. At this time, they are not FDA approved, and are at various stages of development. Studies are aimed at treating all symptoms of ALS including reducing apoptosis, decreasing local free radical formation, and administering various neurotrophic factors. Additionally, FDA-approved drugs for other indications and diseases are being studied for possible benefit in ALS. Outside of the clinic, there is a wide range of research that is being conducted including next generation RNAi therapeutics, stem cell therapeutics, and gene therapy. Most of these therapeutics are predicted to be years or even decades away from clinical use.

In addition to a number of clinical trials<sup>1-4</sup> that test new therapeutics, researchers are evaluating the role of supportive treatments<sup>5,6</sup>. Researchers have also made contributions in understanding the mechanisms of ALS with clinical samples and in transgenic animal models<sup>7,8</sup>. The SOD1 protein continues to be the topic of much research and progress is being made in understanding its contribution<sup>9-14</sup>, as well as other



genes that may contribute to ALS progression<sup>15-17</sup>. Next generation therapeutics including gene therapy<sup>18-23</sup> and RNAi/siRNA<sup>24-26</sup> are also being developed that treat a number of symptoms of ALS including apoptosis<sup>27</sup>, reduced levels of neurotrophic factors<sup>28</sup>, DNA repair mechanisms<sup>29</sup>, and exploring the role of hypoxia in ALS<sup>30-33</sup>. Additionally, VEGF<sup>34,35</sup> and IGF-1<sup>36-39</sup> are among the many molecules that are currently being tested as a possible ALS therapeutic. It is not yet clear which experimental approaches will be most successful, and more research is needed to understand the relative and absolute role of stopping ALS progression for each therapeutic.

## **1.2.0 Magnetic resonance imaging**

### *1.2.1 Overall background*

Magnetic resonance imaging (MRI) is a method that is commonly used clinically to visualize tissue. MRI utilizes a magnetic field to generate an image of local tissue including: brain and spinal cord imaging, tumors, cardiac tissue and vasculature, and joints and cartilage. MRI differs from other imaging methods including positron emission tomography (PET), which detects radioisotopes and generates an image, because it has much higher resolution than PET. Additionally, a foreign radiolabeled product is not required to generate images; however, often an MRI contrast agent is administered for certain applications. Generally, MRI is considered very safe, but it cannot be performed with patients who have any metals that are sensitive to a magnetic field such as certain implants because the strong magnetic field would cause internal motion. One of the most common side effects in patients is a feeling of claustrophobia

because the imaging scan can take several hours to complete. Usually, the magnetic fields that are used in clinical MRIs have field strengths between 0.5-3 Tesla. However, experimental MRIs for non-human use have 14T magnetic strengths, or even higher. Despite the high resolution images given by MRI, machines are very expensive to purchase and operate, and often doctors make decisions about whether to give an MRI imaging session based on cost considerations.

### *1.2.2 Methods of Imaging*

The images from an MRI are obtained by generating a strong magnetic field and by measuring the rate at which protons align with the magnetic field. The relaxivity, or rate at which the protons return to their native state, is different for each type of tissue, and can be affected by fluid levels or the presence of a contrast agent. There are several types of scans on an MRI, and all have the goal of maximizing the signal contrast and generating maximum signal to noise in the tissue of interest. Generally, there are two types of relaxivity: longitudinal relaxivity which is associated with T1 contrast, and transverse relaxivity, which is associated with T2 contrast. Usually, the rate that protons return to their native longitudinal state is faster for T2 contrast by approximately an order of magnitude, but this rate is affected by the overall strength of the magnetic field. A modified type of T2 sequence is often used for functional MRI brain imaging to account for local differences in field strength.

Various contrast agents can be administered that can enhance the signal of either T1 or T2 contrast. Gadolinium is often used clinically to enhance T1 and makes tissue appear whiter in the presence of this agent<sup>40,41</sup>. Gadolinium is toxic in its native form,

but is usually administered with a chelate which allows interaction with protons on water molecules but reduces tissue toxicity. Additionally, recent studies have suggested that there may be additional safety issues with the use of gadolinium for patients at high risk of kidney failure, and the FDA has approved additional warning labels for gadolinium based products to account for this. There are also T2 contrast agents, such as iron core nanoparticles that can lead to an enhanced T2 signal that is darker compared to local tissue<sup>42-44</sup>. Often nanoparticles are functionalized to allow interaction with antibody molecules for targeting applications in tumors<sup>45,46</sup>. These studies could be expanded to other research areas including targeting the central nervous system.

### *1.2.3 Research involving ALS*

MRI is commonly used as one of the primary methods to diagnose ALS, specifically by ruling out cancer of the brain and spinal cord as a primary diagnosis. Additionally, researchers have used experimental MRI sequences to study the progression of ALS<sup>47-60</sup>. These studies have ranged from quantifying the size of the spinal cord using MRI to assess the disease progression to using more sophisticated diffusion tensor sequences. These methods are currently experimental, are not FDA-approved as an ALS diagnostic, and are not used by clinicians outside of a research environment. The use of MRI in monitoring the progression of ALS could see increasing use with the development of specific biomarker contrast agents.

## 1.3.0 Drug Delivery

### 1.3.1 Background

Many therapeutics are delivered via oral or injectable administration routes. However, it is often difficult to maintain drug concentrations within the therapeutic window. If drug concentrations are too high, side effects can occur (including death), but if drug concentrations are too low, the therapeutic is often not effective. Additionally, drug clearance rates including the first pass metabolism (clearance in the hepatic system) eliminate the drug from the system over time. This is complicated by the fact that different drugs have various therapeutic windows and clearance rates. The liver is responsible for breaking drugs down into metabolites that can be cleared from the kidney, but metabolites can be toxic. Models to predict drug toxicity are often inadequate because initial *in vitro* screens are conducted with cells in a 2D culture system that do not represent the liver microenvironment<sup>61</sup>. These issues and considerations affect the overall bioavailability and biodistribution over time, and are the cause of the failure for many candidate drugs failing prior to and during clinical trials. Controlled and more effective drug delivery can alleviate many of these problems.

### 1.3.2 Biodegradable Polymers

The field of drug delivery has seen advancement by the development of biodegradable and biocompatible synthetic polymers. These polymers include poly(lactic-co-glycolic acid) (PLGA), poly(lactic acid) (PLA), and poly(glycolic acid) (PGA). These polymers vary by their core composition, degradation rates, and drug release profiles, but are all generally considered well tolerated and are utilized in FDA-

approved products. They degrade into either lactic acid or glycolic acid and water, and as they degrade, an encapsulated therapeutic is released. Initial polymer studies were used to treat brain tumors and improve survival <sup>62-68</sup>, and since that point, significant advancements have been made in polymer design and in understanding release <sup>69-73</sup>. The next generation polymers that are being developed include polymers with positive charges that may enhance gene delivery, and those that have different degradation profiles and release characteristics. Therefore, the drug release can be controlled for many compounds for each application.

### *1.3.3 Blood Brain Barrier (BBB)*

Delivering therapeutic agents to the CNS is of great importance but has remained challenging in part because of difficulties in penetrating the blood brain barrier (BBB), a layer of endothelial cells bound by tight junctions. Most drugs that are larger than ~400 daltons do not pass through the BBB with high efficiency <sup>74</sup>. Various approaches have been used to administer agents to the CNS including concentrated mannitol, vascular endothelial growth factor (VEGF), ultrasound, encapsulation within nanoparticles, and retrograde transport. Of these, mannitol remains the most widely used clinically, primarily for applications in cancer treatment. Ultrasound and VEGF administration remain an active field of ongoing research. In addition, nanoparticle (both non-targeted and targeted) and retrograde transport approaches have been used successfully to penetrate the BBB.

#### *1.3.4 Microparticles and nanoparticles*

Microparticles (1-1000um) and nanoparticles (1-1000nm) are often defined by their size and are can be synthesized from commonly used polymers, including PLA, PLGA, and PLG. These nanoparticles and microparticles are usually used to encapsulate and release a therapeutic agent usually over a period of days to months, with minimal toxicity<sup>69</sup>. Nanoparticles can be administered either through non-targeted or targeted delivery. During the latter, a protein, aptamer, peptide sequence, or other targeting molecule specific for a receptor is attached to the outside of the polymer nanoparticle. Targeted nanoparticles offer the potential for local delivery, reducing any systemic side effects of the encapsulated therapeutic, and may reduce systemic clearance rates (i.e. from the kidney, liver, or macrophages)<sup>75</sup>. This is important as common routes of nanoparticle administration include intravenous and intramuscular delivery, both of which may lead to rapid clearance and reduced efficacy with certain applications. Many studies have found that the incorporation of polyethylene glycol (PEG) to the polymer chain reduces clearance rates and may improve overall efficacy<sup>76</sup>.

Most nanoparticles are not efficient at penetrating the CNS because of a combination of their size, surface charge, and hydrophobic properties<sup>74</sup>. However, their smaller size (in comparison with larger microparticles) may allow for greater BBB penetration. Recently, non-targeted polymer nanoparticles prepared from polybutylcyanoacrylate (PCBA) polymer encapsulating a variety of drugs and coated with a polysorbate 80 surfactant have been shown to penetrate the BBB<sup>77-81</sup>. The mechanism for uptake is not fully understood, but is proposed to take place via receptor mediated endocytosis in brain endothelial cells (ref)<sup>82</sup>. However, in contrast to PLA,

PLG, and PLGA polymers that are currently used in FDA-approved applications, PCBA polymers would need to be studied more extensively before they are widely used clinically<sup>83</sup>. Targeted nanoparticles may allow for boundaries such as the BBB to be penetrated by facilitating endocytosis or transcytosis across brain endothelial cells, or by utilizing retrograde transport to bypass the BBB.

## **1.4.0 Retrograde transport**

### *1.4.1 Background*

Axonal retrograde transport is an important cellular process used by neurons to transport proteins, small molecules, and even cell organelles from the terminal end of a neuron towards the cell body. Different molecules are transported via different mechanisms of axonal transport. Specifically, axonal retrograde transport is usually subdivided into molecules that are transported via fast transport (50-400mm/day) and slow transport (less than 10mm/day). The mechanisms of both fast and slow transport are still being investigated, but fast transport is largely thought to be mediated by dyenin and slow transport is mediated by kinesins.

### *1.4.2 Molecules that use retrograde transport*

Retrograde transport is utilized by viruses (i.e. herpes) and bacterial toxins (i.e. tetanus toxoid) to bypass the BBB and efficiently penetrate the CNS. This process has evolved over millions of years, and is highly efficient, often leading to the toxicity of many of these molecules. In addition, molecules such as manganese are transported via this mechanism, and have been used as MRI contrast agents. Other molecules that are

transported retrogradely include: poliovirus, wheat germ agglutinin (WGA), and rabies.

Many of these molecules are being studied both to understand the mechanism of transport and to utilize natural mechanisms of transport for drug delivery.

#### *1.4.3 Use as a delivery vehicle*

Researchers have used retrograde transport to deliver genes and protein conjugates to the CNS with therapeutic efficacy<sup>36,84</sup>. This approach offers the possibility of selectively targeting a specific region of the CNS that is a function of the injection site. This is in contrast to non-targeted intravenous administration that would likely penetrate the entire CNS equally. However, one concern with using this approach is a possible immune response, which may be particularly important in patients diagnosed with cancer or those taking immunosuppressive medications. The immune response will likely be a function of the retrograde transport molecule used and previous immunizations to that molecule. Recently, the tetanus toxin C fragment (the non-toxic binding portion of the tetanus toxoid that is efficiently retrograde transported in neurons) was conjugated to nanoparticles and shown to target neuroblastoma cells *in vitro*<sup>85</sup>. It is not clear yet whether this approach will lead to nanoparticles penetrating the CNS with high efficiency *in vivo*.

#### *1.4.4 Retrograde transport and ALS*

In addition to using retrograde transport as a delivery system, this important cellular process is well studied as it relates to the progression of neurodegenerative disease such as ALS. It has been shown that ALS is impaired preceding the visible



symptoms of ALS<sup>86-91</sup>. Additionally, there has been some progress made in using biomarkers to monitor this transport such as manganese<sup>92</sup>. However, it is expected that by utilizing bacterial or viral toxin fragments, we may gather additional insight into the disease progression and generate biomarkers with more clinical utility.

## **1.5.0 Stem cells**

### *1.5.1 Background and derivation*

One therapeutic area of interest for ALS is tissue engineering from stem cells. This offers a mechanism to treat advanced cases of ALS, where motoneurons have significantly degenerated, and may help to restore lost limb function. This approach could be used in parallel with pharmaceutical agents to treat ALS both on a molecular and cellular level.

Stem cells are undifferentiated (unspecialized) cells that reside among differentiated (specialized) cells in a tissue or organ and have the capability for self-renewal (producing identical copies of themselves) throughout their lifetime. A stem cell is also capable of producing more mature (specialized) cell types of the specific tissue or organ in which it resides through differentiation<sup>93</sup>. This allows the existence of a constant pool of specialized cells needed for homeostasis. To some extent, this pool also allows the replacement of dead, injured, or diseased cells (regeneration of injured tissue in an organ).

There are two primary classifications of stem cells: adult stem cells and embryonic stem cells. Adult stem cells are partially differentiated stem cells that maintain some pluripotency, but cannot become any cell type. In contrast, embryonic

stem cells can differentiate into any cell type. This makes embryonic stem cells particularly useful for studies aimed at better understanding developmental biology and those or for studies in which multiple cell types interact together in a cell microenvironment. Mouse embryonic stem cells have been studied for several decades, but human embryonic stem cells (hESC) were recently derived approximately ten years ago.

### *1.5.2 Ethical considerations*

There has recently been controversy and ethical debate regarding the use of hESC for research purposes. The primary arguments center around whether it is acceptable to use cells that have been derived from a fertilized embryo. Specifically, hESC were developed from early embryos in a laboratory that were to be discarded from *in vitro* fertilization clinics. At present, the National Institutes of Health have provided guidelines which limit government funding to only cell lines that have already been derived. The research in this study used only NIH-approved hESC lines. It is clear that more research will be needed before we understand any ethical considerations and the role of stem cells in any clinical treatments or tissue engineering applications.

### *1.5.3 Differentiation (including neuronal)*

One active focus of current research involves guiding the differentiation of undifferentiated stem cells into certain cell types and tissues. hESC are exposed to a variety of microenvironment conditions, nanotopography, and growth factors to induce differentiation. However, most cell populations remain mixed and this process is not

well understood. It is clear that a variety of factors contribute to cell differentiation and more research is needed.

Researchers are investigating new ways to promote neuronal differentiation with some applications for ALS<sup>94-96</sup>. There are a variety of markers for neuronal differentiation that are used including: nestin, Sox1, beta-3 tubulin, TuJ, and MAP2. These markers may have basal expression levels in undifferentiated stem cells, so it is important to compare these levels to appropriate controls. It is clear that having a high population of neural cells could advance tissue engineering research.

Research has been successful at generating high relative fractions of stem cells that express neuronal markers and exhibit neuronal characteristics. Usually, a variety of growth factors are used for differentiation studies, but it is also possible to use microfluidic technology as well<sup>97-104</sup>. However, this research must be expanded to include a 3D environment to move closer to a therapeutically relevant tissue engineering approach.

#### *1.5.4 Undifferentiation*

One field of active research is maintaining cells in an undifferentiated environment. Various markers are used show that cells are undifferentiated including nanog, Oct4, and SSEA4, which are transcription factors. However, these markers are not always equally expressed even in undifferentiated and pluripotent cells. Therefore, more accurate and specific markers would help researchers to better quantify each cell population. Certain scaffolds have been produced including those prepared from hyaluronic acid (HA) that can maintain cells in an undifferentiated environment<sup>105</sup>.

Often, synthetic scaffolds are preferred because any many applications have a long term clinical goal which would be complicated with animal derived products.

#### *1.5.5 Applications of stem cells for ALS*

Stem cells have recently been used as an experimental approach to treat ALS. Most of this research is still being conducted in an animal model, and there is no FDA-approved treatment for ALS that utilizes stem cells at the present time. However, research in animal models is advancing rapidly, and progress is being made. Stem cells are currently being tested as both supportive and replacement therapies for ALS, meaning they could either reduce the rate at which motor neurons lose motor function and support recovery, or serve as a template for new neural connections<sup>106</sup>. For example, recently researchers have shown that stem cell grafts that were transplanted into rats grew axons and synapsed with neighboring cells<sup>107-112</sup>. However, this research does not demonstrate that there will be an improvement in recovery in movement and motor neuron function.

It is also becoming more clear that stem cells function together with their microenvironment and other cells in a highly dynamic process over the ALS disease progression, and that understanding this microenvironment will be critical in developing therapeutically relevant treatments<sup>106, 113, 114</sup>. Therefore, researchers are utilizing growth factors and cytokines to control stem cell fate and improve motor neuron function in ALS, or genetically engineering stem cells to upregulate expression of these growth factors<sup>115</sup>. It is most likely that a combination approach will be required for successful therapy<sup>115</sup>.

### 1.5.6 Hydrogels and scaffolds

It is well-established that differences exist between cells grown in two dimensional (2D) culture and cells found in their native 3D environment, where they are surrounded by other cells and held in a complex network of extracellular matrix (ECM). In developing tissue, a unique 3D microenvironment with specific mechanical properties is formed by the ECM and various regulators. Cellular microenvironments *in vivo* are immobilized within tissue and are bound to ECM proteins that control mechanical stiffness by both chemical and biophysical cues. This matrix elasticity has been shown to direct stem cell lineage differentiation. However, it is still not clear how hESC sense 3D matrix elasticity and translate that into self renewal and tumor formation signals. It is therefore desirable to study cell differentiation in conditions that closely resemble the natural 3D microenvironment because these cell matrix interactions may more accurately represent *in vivo* conditions.

Three-dimensional scaffolds can be used to provide for a template for cell proliferation and differentiation. Certain scaffolds may more accurately mimic the native chemical and mechanical microenvironment of stem cells<sup>116-120</sup>. A number of natural and synthetic biomaterials have been used as cell scaffolds or for cell encapsulation (i.e. Matrigel, hyaluronic acid, collagen, dextran etc.). However, most scaffolds do not have the range of mechanical properties observed *in vivo*, and they lose strength and integrity as cells proliferate.

Bioelastomer materials may provide a flexible scaffold for the 3D culture of cells. Poly(glycerol sebacate) (PGS) was developed and shown to be biocompatible both *in*

*vitro* and *in vivo*<sup>121, 122</sup>. A recent modification to PGS incorporated acrylate groups into the polymer backbone that allowed for photo-polymerization with well-defined and tunable mechanical properties resembling those of native soft tissue. Additionally, PGSA was shown to support the culture of neuroblastomas and human embryonic stem cells *in vitro*, and to be highly biocompatible *in vivo*. These studies could lead to new therapeutic options for neurodegenerative diseases including ALS.

### **1.6.0 Overall goals**

The overall goal of this thesis is to make a contribution to scientific research by developing next generation methods to diagnose and treat ALS. To this end, we have conducted a three prong approach: 1) using a gadolinium tetanus toxin C fragment (Gd-TTC) conjugate as a biomarker and early diagnostic, 2) using a nanoparticle-based drug delivery system to bypass the blood brain barrier, penetrate the central nervous system, and selectively target neurons, and 3) using a combination of natural and synthetic polymers and growth factors in a 3D scaffold to enable human embryonic stem cell differentiation into neurons for tissue engineering applications. We feel that given our multidisciplinary expertise, this approach was the most efficient way to lead to high impact solutions in an established field of research. It is our expectation that our contribution will give ideas to others in the fields of drug delivery and neurodegenerative research.

## **1.7.0 Format of this document**

This thesis document begins with an introduction of topics that are pertinent to our overall goals, and then is organized into chapters that follow the specific aims of this thesis. Following research chapters is a section focusing on future work for the logical next steps following this thesis, and then a list of appendices. The appendices are organized in a way such that they follow the format of the thesis chapters. They contain an appendix summary, supplemental data, results from early experiments, and alternative analysis of data that was previously presented. It is our goal that these data will further guide researchers in what experiments are successful, and what experiments will be high risk.



## **Chapter 2: Development of a gadolinium tetanus toxin C fragment conjugate biomarker for *in vivo* MRI visualization of axonal retrograde transport in an amyotrophic lateral sclerosis mouse model**

### **2.1.0 Abstract**

Amyotrophic lateral sclerosis (ALS, or Lou Gehrig's disease) is a neurodegenerative disease with ineffective treatments at stopping the disease progression. We have developed a gadolinium tetanus toxin C fragment conjugate (Gd-TTC) that was shown to be highly visible under MRI, as determined by relaxivity experiments, and preserved the neuroblastoma cell binding properties of the native protein *in vitro*. Live animal and *ex vivo* MRI imaging showed that Gd-TTC transport could be visualized in the lumbar spinal cord following a hindlimb intramuscular injection in mice. Histological analysis confirmed these observations and confirmed that Gd-TTC was localized in the ventral horn of motor neurons in the lumbar spinal cord. H&E staining showed that Gd-TTC was well tolerated and biodistribution studies showed that it remained in high concentrations near the site of injection after 48 hours. The Gd-TTC was used to quantify reductions in axonal retrograde transport efficiency in a transgenic mouse model for ALS over the disease progression. We therefore conclude that the Gd-TTC conjugate may have applications as a minimally-invasive biomarker for neurodegenerative disease including ALS.

## 2.2.0 Introduction

Amyotrophic lateral sclerosis (ALS, or Lou Gehrig's disease) is a degenerative disease that affects motor neurons, causing progressive paralysis and death, typically within 5 years. An estimated 30,000 patients in the US are diagnosed with ALS; about 5,000 new cases arise every year. Although progress is being made in understanding the causes of the disease and in developing new treatments for ALS, there is still much work to be done<sup>25, 36, 123, 124</sup>. Only a single compound is FDA-approved for ALS, and its benefit is marginal<sup>125-127</sup>. A major challenge in treating ALS and other neurodegenerative diseases is directly targeting the central nervous system (CNS), a compartment that is difficult to penetrate because it is protected by the blood-brain barrier (BBB). Several methods have been used to penetrate the BBB including physical disruption by osmotic pressure, nanoparticles, and retrograde transport, but progress is still needed in this field<sup>36, 81, 84</sup>.

Retrograde transport from distal axon terminals to the neuronal cell body is an essential process in neurons; it is used to transport enzymes, vesicles, and mitochondria, and is exploited by viruses and bacterial pathogens as a route to intoxicate motor neurons<sup>128-131</sup>. The mechanism of retrograde transport is not well understood but is known to involve microtubules, dynactin and dynein. Additionally, retrograde transport can be divided into fast and slow components. Fast retrograde transport (speed ~400mm/day) is specific to membrane bound organelles, whereas slow retrograde transport (~5mm/day) is used to transport soluble proteins that are not membrane-bound. It is becoming well established that retrograde axonal transport of substances from the periphery to motor

neuron cell bodies can be used as an effective route to penetrate the CNS and bypass the BBB .

One problem in ALS therapy trials is that the disorder is usually not diagnosed until symptoms are advanced, precluding possible benefit from early intervention. A major limitation in devising therapies for ALS and other disorders affecting motor neurons is the absence of biomarkers that permit relatively rapid testing of drug efficacy. In the absence of such biomarkers, the gold standard in ALS therapeutics is analysis of survival; unfortunately, survival analyses are lengthy and expensive. Our knowledge of ALS disease progression has formed the basis for several transgenic animal models that are widely used in research laboratories in these studies. However, it is likely that physiological parameters that reflect the disease process could also serve as surrogate markers for the disease. This concept is exemplified in the muscle disorder polymyositis, for which heightened blood levels of the skeletal muscle enzyme creatine kinase accurately reflect the activity of the underlying muscle inflammation. To date, the only physiological indicators of motor nerve function are electromyographic assessments of the integrity of the motor unit. Regrettably, these measurements do not closely correlate with the stage and activity of the disease. Confounding the situation in ALS, these parameters, like the clinical presentation, do not become diagnostically useful until the disease is well advanced. For these reasons, it is striking that in experimental models of motor neuron disease, such as transgenic ALS mice, the process of axonal transport appears to be significantly deranged early in the course of motor neuron disease. This raises the possibility that techniques that allow one to non-invasively and accurately to define rates of axonal transport in humans would greatly enhance the diagnosis of motor

neuron diseases. Such methods would potentially serve as the desired biomarkers for motor neuron dysfunction that would facilitate and accelerate drug testing.

One important element in our early studies has been the use of a non-toxic fragment of tetanus toxin, known as tetanus toxin C fragment or TTC. TTC is the neuronal binding portion of the native tetanus toxin. It demonstrates extremely high affinity binding to the neuronal ganglioside GT1<sub>b</sub> that is the tetanus receptor. Because GT1<sub>b</sub> is located selectively the surfaces of neurons, TTC shows highly selective neuronal binding. Moreover, once it binds to neurons, TTC, like tetanus itself, is readily taken up in endosomes and efficiently transported via retrograde transport from the distal axonal terminus to the neuronal cell body. We and others have found that TTC binding and transport in neurons is quantitative both *in vitro* and *in vivo*; TTC is routinely used in experimental systems to provide quantitative assessment of retrograde axonal transport in motor neurons. The overall goal of this study is to develop a minimally invasive biomarker by conjugating gadolinium, a clinically used and highly MRI visible molecule, to TTC and to evaluate this as a biomarker for ALS and other neurodegenerative diseases.

## 2.3.0 Methods

*2.3.1 Synthesis of Gd-TTC and Gd-BSA:* A gadolinium protein labeling kit (BioPAL; Worcester, MA) was used to chemically conjugate gadolinium to TTC (Roche Applied Science; Indianapolis, IN) and BSA (Sigma; St. Louis, MO), according to the manufacturer's directions. Briefly, 4 mg protein was dissolved in 1.4mL 0.2M carbonate buffer (pH 8.9, final protein concentration 2.86mg/mL). 393uL of 1M sodium acetate containing 1M sodium hydroxide and 6.66uL 1M GdCl<sub>3</sub> were added in sequence to 7.3umol of an amine-reactive gadolinium chelate. The chelate was vortexed for approximately 2 minutes and allowed to incubate for 5 minutes at RT. 100uL of the subsequent chelate was incubated with 4mg of the protein under gentle stirring for 2 hours. Subsequent product was dialyzed with PBS for 2 hours (RT), 2 hours (RT), and overnight (4°C) against a 10 kDa dialysis cassette (Pierce Biotechnology). Dialysis medium was exchanged between each dialysis period. Protein was lyophilized and stored at -20°C until use.

*2.3.2 Protein characterization:* Gadolinium conjugates were prepared as described above. Protein samples (BSA, Gd-BSA, TTC, or Gd-TTC) were mixed 1:1 with a diluent (95% blue, 5% beta-mercaptanol) and heated for 5 minutes at 95C to denature the protein. 20uL of protein samples and 10uL of the ladder standard were loaded into a 15% SDS gel (COMPANY) in 1x tris-glycine buffer. BSA and Gd-BSA protein concentrations were 20ug/mL, and TTC and Gd-TTC protein concentrations were 50ug/mL. The gel was run for 55 minutes at 200V, stained in Coomassie blue solution for ~3h, and then destained in acetic acid solution overnight. Gels were photographed using a digital camera.

*2.3.3 Culture of N18-RE-105 neuroblastoma cells:* N18-RE-105 neuroblastoma cells were grown with previous methods as those previously described <sup>85</sup>. Briefly, neuroblastoma cells were cultured in DMEM and supplemented with HAT supplement (100uM sodium hypoxanthine, 400nM aminopterin, 16uM thymidine), 10% FBS, and 1% penicillin/streptomycin. All cells were grown in filtered flasks in an incubator at 95% air and 5% carbon dioxide. Media was changed every 48 hours, and cells were passaged with EDTA-trypsin when confluent. All media reagents were purchased from Invitrogen. N18-RE-105 cells were a generous gift of Dr. Jonathan Francis at the Massachusetts General Hospital.

*2.3.4 Cell binding assay and flow cytometry:* N18-RE-105 cells ( $10^6$  cells/mL) were removed from culture and incubated with Gd-BSA, TTC, or Gd-TTC (final protein concentration 10ug/mL) in 500uL of media containing 10% FBS for 60 minutes on ice. Cells were then incubated with a mouse monoclonal antibody against TTC (Roche Applied Science, Indianapolis, IN) at 10ug/mL for 60 minutes on ice. Cells were then incubated with a FITC-conjugated fluorescent anti-mouse secondary antibody with a 1:50 final dilution for 45 minutes on ice. Cells were washed with PBS containing 1% BSA 3x by centrifugation (3 minutes, 4C, 1500rpm) in between each incubation and after the final antibody incubation. Negative controls lacking protein, primary antibody, or secondary antibody were conducted analogously to verify antibody specificity. Cells were analyzed using a FACScan flow cytometer (Becton Dickinson) to measure fluorescence (488nm excitation, 530nm and 650nm emission) as previously described . Briefly, cells were

incubated with propidium iodide (5ug/mL), and cell populations were gated based on forward/side scatter and propidium iodide fluorescence to remove debris and dead cells from analysis. A total of at least 10,000 gated events were obtained for each sample. Data was analyzed using FlowJo software (Tree Star) to generate histograms of each sample.

*2.3.5 MRI relaxivity measurements:* Gd-TTC and Gd-BSA dissolved in PBS with final protein concentrations between 5mg/mL to 40ug/mL in 1:2 dilutions and placed in a 96 well plate. The signal intensity was determined at seven different inversion times for each protein concentration that were determined to give linear range fits with signal intensity (inversion times between 10 milliseconds and 10 seconds) using a Bruker NMR Minispec (Billerica, MA) as previously described <sup>45</sup>. Relaxivity values were determined using the following equation:  $M_z(TI) = M_\infty (1 - e^{-TI/R_1})$ ;  $T_1 = 1/R_1$ , where  $M_z(TI)$  represents the signal intensity at each inversion time,  $M_\infty$  represents the signal intensity at high inversion times, TI represents each inversion time, and  $R_1$  represents the signal relaxivity. Relaxivity values were determined for each protein concentration using best-fit functions in OriginLab software and plotted as a function of protein concentration (OriginLab, Northhampton, MA). Each reported value represents the cumulative average of over 5,000 independent measurements.

*2.3.6 MRI imaging of Protein Contrast (1.5T):* Gd-TTC and Gd-BSA were dissolved in PBS at concentrations between 3mg/mL and 190uL/mL in 1:2 dilutions and placed in a 96-well plate. PBS was placed in all wells and in the space between wells to provide a direct comparison in magnetic contrast and to minimize artifacts induced by the plate.

Samples were pulsed with a 90-180-90 inversion recovery MRI protocol using a 1.5T magnet with inversion times varied between 20-4000ms. Images were captured and processed using ImageJ software (National Institutes of Health, Bethesda, MD) for analysis.

*2.3.7 Animal study approval and injections:* All animal protocols were approved by the SRAC committee on animal care at the Massachusetts General Hospital. Mice (8-16 weeks) were anesthetized with 130mg/kg ketamine and 10mg/kg xylazine via an intraperitoneal injection. Mice were shaved and an incision was made exposing the right quadriceps under aseptic conditions. Three 25uL injections containing Gd-TTC, Gd-BSA, Eu-TTC, or Eu-BSA (20mg/mL) or a PBS negative control were made into the muscle using a 26G Hamilton syringe (1.5mg protein injected). The wound was sutured and the animal was allowed to recover.

*2.3.8 9.4T MRI live animal imaging (in vivo):* Animals were anesthetized under isoflurane/N<sub>2</sub>O/O<sub>2</sub> (1.5-2% isoflurane) and restrained in a headholder at 38C using a water blanket. A custom-made MRI surface coil was secured on the animal's back and centered around the lumbar spinal cord region. Animals were placed in a 9.4T magnetic field for imaging. Axial cross sections were taken of the animals at various echo times (20-4000ms) and recovery times (5-50ms) using a standard 90-180-90 inversion recovery MRI sequence, similar to those previously described . Section thickness ranged between 0.5-1.5mm, with a 2.5x2.5cm FOV, and resolution up to 256x256. Images were processed using ImageJ software (National Institutes of Health, Bethesda, MD).



*2.3.9 Transcardial perfusion and spinal cord isolation:* Animals were sacrificed using CO<sub>2</sub> asphyxia. An incision was made opening the animal's sternum, and a 30G needle was inserted into the left ventricle. The right atrium was cut, and the animal was perfused with PBS until blood cleared. Perfusion medium was switched to 4% paraformaldehyde solution and perfused for 15 minutes. The spinal cord was gently removed from the vertebrate using forceps and blunt dissection, and cut into cervical, thoracic, and lumbar sections. Tissue was fixated in 4% paraformaldehyde overnight. For immunohistochemistry experiments, tissue was incubated in 10% sucrose for 12 hours, and then in 30% sucrose solution for 12 hours, each overnight at 4C until sectioning. Tissue for MRI *ex vivo* imaging and hematoxylin/eosin staining was stored in PBS until imaging or mounting.

*2.3.10 14T MRI spinal cord imaging (ex vivo):* The spinal cord from Gd-TTC injected mice was fixed as described above and placed in an NMR tube in non-magnetic Fluoro solution. Axial cross sections were taken of the spinal cord at various echo times (20-1000ms) and recovery times (5-50ms) using a standard 90-180-90 inversion recovery MRI sequence, similar to those previously described . Section thickness ranged between 0.5-1.5mm, with a 2.5x2.5cm FOV, and resolution up to 256x256. Images were processed using ImageJ software (National Institutes of Health, Bethesda, MD).

*2.3.11 Hematoxylin and Eosin staining:* Spinal cords of PBS, TTC, or Gd-TTC injected mice were prepared as described above. Tissue was dehydrated in graded ethanol (70 -

100%), embedded in paraffin, sectioned axially using a microtome (4 $\mu$ m), and stained with H&E.

*2.3.12 Immunohistochemistry staining for TTC and NeuN:* Mice injected with either TTC or Gd-TTC were sacrificed 24-48 hours post injection. Samples were placed in Tissue-Tek OCT gel (Sakura Finetechnical Co, Tokyo, Japan), frozen on dry ice, and stored at -80°C till cryostat sectioning. Tissue was blocked and permeabilized in using PBS containing 0.3% Triton-100 and 10% FBS for 1h at RT. Tissue was incubated with rabbit anti-TTC (1:1000, Rockland Immunochemicals; Gilbertsville, PA) and mouse anti-NeuN (1:500, Chemicon; Billerica, MA) containing 0.1% Triton-100 and 10% FBS overnight at 4C. Tissue was washed in PBS 3x to remove unbound primary antibodies. Tissue was incubated with Cy3 conjugated goat anti-rabbit (1:1000, Jackson ImmunoResearch; West Grove, PA) and FITC conjugated goat anti-mouse (1:100, Sigma; St. Louis, MO) containing 0.1% Triton-100 and 10% FBS for 1.5 hours at RT. Tissue was washed 3x in PBS to remove unbound secondary antibody. Tissue was mounted using Vectashield fluorescent mounting medium containing DAPI (Vector Laboratories; Burlingame, CA) and imaged using a Nikon E800 microscope.

*2.3.13 Biodistribution (in vivo) and neutron irradiation analysis:* Europium-conjugated TTC and BSA were prepared analogously to preparation of gadolinium conjugated described above, but using EuCl<sub>3</sub> instead of GdCl<sub>3</sub> and a europium protein conjugation kit from BioPAL (Worcester, MA). Mice were injected with Eu-TTC, Eu-BSA, or PBS. Mice were sacrificed 48 hours post injection, and the following organs were harvested

and weighed: spinal cord, blood, spleen, heart, lungs, liver, kidney, brain, injected quadriceps, and uninjected quadriceps. Tissue was oven dried at 70C overnight and sent to BioPAL (Worcester, MA) for neutron irradiation analysis and quantification of europium content in each tissue using a short activation protocol. Briefly, tissue was exposed to a field of thermal neutrons for one minute. Tissue was stored for 24 hours to allow short-lived activation products to decay. Spectroscopic analysis was performed on each sample and reported as disintegrations per minute (dpm) measured for europium. Measurement normalization and corrections were made at BioPAL to account for inter-radionuclide crossover and tracer decay during the counting period. Instruments were calibrated to account for differences in sample volume and geometry. All sample analysis was conducted within one week of the removal of tissue.

*2.3.14 Image analysis and quantification:* ImageJ (NIH, Bethesda, MD) and Matlab (Mathworks; Natick, MA) were used for all image processing. A region of interest corresponding to the ventral horn in the lumbar spinal cord was determined, and ImageJ was used to determine pixel intensity over the entire region and automatically grouped into 256 bins. Data was then inputted into Matlab and fit to a normal distribution using built-in functions. Average distribution values for each corresponding side were analyzed and, sorted into positive and negative sides, and expressed as a normalized ratio for each set of wildtype or ALS animals.

## 2.4.0 Results and Discussion

### 2.4.1 Conjugation of gadolinium to TTC

We hypothesized that gadolinium could be conjugated to TTC to produce an MRI contrast agent biomarker for axonal retrograde transport. We reasoned that gadolinium 1) has high  $T_1$  magnetic contrast properties, 2) is widely used clinically as an imaging agent, and 3) is small in molecular weight relative to the size of TTC and is therefore expected to minimally affect transport. Gadolinium was incubated with a functionalized chelate and subsequently conjugated to primary amine groups on TTC and purified by dialysis (see Figure 1a). Gadolinium was also conjugated to BSA and the resulting conjugate was used as a control protein for all experiments, having both molecular weight and amino acid composition similar to that of TTC.

To verify successful conjugation and to determine whether unconjugated protein remained in each sample, we ran Gd-TTC and Gd-BSA against unconjugated controls on an SDS page gel and processed samples with a Coomassie blue stain (see Figure 1b). Both Gd-TTC and Gd-BSA showed higher molecular weights and wider distributions than the respective unconjugated TTC or BSA protein, suggesting successful chelate conjugation. Based on molecular weight standards and neglecting any effect of the chelate on protein mobility, the ratio of conjugated chelate to protein was estimated to be 7.1 for Gd-TTC and 5.6 for Gd-BSA. Additionally, bands corresponding to unconjugated protein were absent in Gd-TTC and Gd-BSA samples, suggesting that gadolinium conjugation was successful and products contained only trace unconjugated protein.

### 2.4.2 Characterization of Magnetic Relaxivity

We characterized the MRI relaxivity properties of Gd-TTC and Gd-BSA, 1) to determine the approximate number of gadolinium molecules that were conjugated to each molecule of protein, and 2) to obtain relaxivity values that could be used in subsequent studies to quantify rates and efficiency of retrograde transport *in vivo*. The magnetic contrast of conjugates was verified by visual inspection using a T<sub>1</sub>-weighted 1.5T MRI sequence in a phantom 96-well plate containing 1:2 serial dilutions of Gd-TTC and Gd-BSA (Figure 1c). In a separate experiment, preparations containing Gd-TTC and Gd-BSA in various concentrations (39ug/mL – 5mg/mL in 2:1 serial dilutions) were analyzed by a modified Bruker mini-spec auto NMR to determine conjugate relaxivity. For each conjugate at each concentration, an inversion recovery sequence was run and signal intensity was quantified to determine R<sub>1</sub> (Figure 1d-e). The R<sub>1</sub> value was plotted as a function of inversion time for each concentration and fit to a linear function to determine the relaxivity of each contrast agent (Figure 1f). The relaxivity of Gd-TTC and Gd-BSA were determined to be 0.029 uM<sup>-1</sup>s<sup>-1</sup> and 0.051 uM<sup>-1</sup>s<sup>-1</sup>, respectively. Both Gd-TTC and Gd-BSA exhibited similar behaviors and had linear relaxation times as a function of concentration (R<sup>2</sup> > 0.999), suggesting that there was minimal free gadolinium in the solution remaining after dialysis purification.

#### 2.4.3 Neuronal binding of Gd-TTC *in vitro*

Gadolinium conjugation could alter the ability of TTC to bind to neurons. We incubated TTC, Gd-TTC, and Gd-BSA with N18-RE-105 neuroblastoma cells that are known to express the G<sub>T1B</sub> ganglioside receptor for TTC on their surface. We incubated each preparation with a primary antibody against TTC followed by a fluorescent

secondary antibody, with appropriate washes in between the incubations. All incubations were done on ice to minimize receptor internalization that may affect binding in subsequent steps. Cells analyzed on flow cytometry showed high levels of fluorescence for positive controls TTC and Gd-TTC, but not in Gd-BSA negative controls or preparations lacking either a primary or secondary antibody (Figure 1g-i). In some preparations containing a secondary antibody, background fluorescence was observed; however, this was almost two orders of magnitude lower than TTC or Gd-TTC samples, and is expected to minimally contribute to the positive signal (Table 1). Interestingly, Gd-TTC samples exhibited a dual peak, suggesting that protein conformation of Gd-TTC may have been slightly affected by the conjugation. However, the overall *in vitro* cell binding properties of TTC were preserved in the Gd-TTC conjugate.

#### 2.4.4 Live animal 9.4T MRI imaging

Wildtype mice were injected with Gd-TTC unilaterally in the quadriceps and allowed to recover for 24-48h prior to *in vivo* 7.4T MRI imaging of the spinal cord. T1-weighted images of the lumbar section of the spinal cord showed areas of high magnetic contrast that were concentrated on the injection side of the animal (Figure 2, top). Contrast was observed in multiple spinal cord sections that were not adjacent, possibly a result of discrete clusters of motor neurons originating from different areas within the lumbar spinal cord. However, the localization of contrast was more central than was expected given known neuroanatomy motor neuron innervation in the ventral horn. This was observed consistently in several animals that were injected, and with different preparations of contrast agent. Additionally, contrast intensity was variable in different

animals suggesting that precise quantification of retrograde transport rates and efficiency may be difficult using this approach. Independent T<sub>2</sub>-weighted imaging scans of non-injected animals verified the interface of the white/gray matter, spinal cord, cerebral spinal fluid, and vertebrae (data not shown). These imaging results taken together are consistent with previously published studies of the mouse spinal cord *in vivo* and *ex vivo* imaging<sup>132, 133</sup>. However, the precise localization of the contrast agent within the spinal cord could not be determined because of visible motion artifacts (i.e. from animal breathing) and we therefore turned to higher resolution imaging of the spinal cord of excised mouse spinal cords.

#### *2.4.5 Ex Vivo 14T MRI imaging (high resolution)*

Spinal cords were excised from Gd-TTC injected animals and imaged *ex vivo* using a 14T MRI to generate high resolution images that were free from fat or motion artifacts. In a T<sub>1</sub>-weighted MRI sequence, unilateral magnetic contrast was observed in the ventral horn of the lumbar region (Figure 2, middle). Images from individual spinal cord sections were processed by examining regions of similar magnetic contrast to further investigate regions of high magnetic contrast intensity (Figure 2, bottom). Consistent with previous observations, there was variability in the contrast intensity and localization between the animals<sup>47, 132</sup>. However, contrast was observed to be primarily localized within expected regions, consistent with previous characterizations of TTC transport in motor neurons .

#### *2.4.6 Immunohistochemistry and Hematoxylin/Eosin Staining*

Spinal cords from Gd-TTC, TTC, or PBS unilaterally injected mice were fixed, sectioned, and immunostained against TTC and NeuN to verify axonal retrograde transport and further explore neuronal localization within the spinal cord. Spinal cord sections showed unilateral positive staining for TTC concentrated in the ventral horn of the lumbar region of the spinal cord (Figure 3). Furthermore, this was co-localized with neuronal positive staining. Spinal cord sections from TTC and Gd-TTC injected mice showed similar localization, intensity, and distribution. PBS or Gd-BSA injected animals showed characteristic NeuN staining, but only background levels of TTC staining (data not shown). These results suggest that axonal retrograde transport properties of TTC are preserved in the Gd-TTC conjugate.

To determine whether any signs of acute inflammation were observed as a result of the presence of the Gd-TTC conjugate, we sectioned and stained spinal cords with hematoxylin and eosin. No differences were observed between injected animals (either TTC or Gd-TTC) and PBS negative controls (Figure 4, top). These results suggest that an injection of the Gd-TTC conjugate is well tolerated and biocompatible. This is consistent with previous observations following the injection of TTC in rodents and the established safety profile of gadolinium compounds used in the clinic<sup>134-139</sup>.

#### 2.4.7 Biodistribution (*in vivo*)

We prepared europium conjugates to TTC and BSA to determine the *in vivo* biodistribution of Gd-TTC relative to that of non-specific Gd-BSA. Eu-TTC and Eu-BSA were prepared analogously to the gadolinium conjugates using the same amine-reactive chelate. Both europium and gadolinium are lanthanide rare earth elements with similar



molecular weights and are expected to attach to the chelate and subsequently the protein in a stable non-reversible reaction. Therefore, the Eu-TTC biodistribution is expected to resemble that of Gd-TTC. Europium can be neutron activated, generating unstable radioactive byproducts that can be measured to quantify the amount of conjugate present in tissue.

Adult mice were anesthetized and the quadriceps injected unilaterally with Eu-TTC or Eu-BSA. Mice were sacrificed and the major organs removed 48 hours post injection (spinal cord, blood, spleen, heart, lungs, liver, kidney, brain, injected quadriceps, and uninjected quadriceps). Organs were processed, and analyzed using neutron activation to determine semi-quantitative levels of Eu-TTC and Eu-BSA in each organ (Figure 4, bottom). After 48 hours, the highest concentration of both Eu-TTC and Eu-BSA were found in the quadriceps near the site of injection. These were not significantly different from each other, but both were higher than their respective uninjected quadriceps ( $p < 0.01$ ,  $n = 4$ ). Eu-TTC levels were found to be higher than Eu-BSA in the kidney ( $p < 0.001$ ,  $n = 4$ ) and lower than Eu-BSA in the spleen ( $p < 0.01$ ,  $n = 4$ ), lungs ( $p < 0.05$ ,  $n = 4$ ), and liver ( $p < 0.01$ ,  $n = 4$ ). This is likely a result of relative  $G_{TIB}$  ganglioside concentrations throughout the animal, which are known to be primarily expressed in neurons but also expressed in other organs. We were not able to detect any conjugate in either the brain or the spinal cord. This is likely because only a small amount of the overall injected dose is transported to the central nervous system, or because the neutron activation assay was not sensitive enough to detect the conjugate at the injected levels. It is also possible that a different timepoint would yield detectable levels of the contrast agent within the CNS. However, based on our previous work, we have seen high

levels the native TTC protein at 24-48 hours. These results therefore suggest that only a small amount of the overall injected dose reach the brain and spinal cord, but that this amount can be detected both by MRI and by immunochemistry.

#### *2.4.8 Gd-TTC as a Biomarker for ALS (in vivo)*

We conducted proof-of-concept studies to test our hypothesis that the Gd-TTC conjugate could be used as a minimally invasive biomarker for neurodegeneration, utilizing a transgenic mouse model for amyotrophic lateral sclerosis. The G93A mouse model that we used has been well-characterized and has a known disease progression that resembles human ALS: 1) at 60 days, mice are visibly asymptomatic, 2) at 90 days, symptoms including decreased muscle strength and mobility appear, and 3) at 120 days, mice are highly immobile and have significantly impaired motor function<sup>140-143</sup>. Transgenic ALS mice and wildtype controls were injected with Gd-TTC and sacrificed 48 hours post injection. Spinal cords were removed for 14T MRI spinal cord analysis, and sectioned for immunohistochemistry staining of TTC on the same spinal cords. MRI images of 60 day ALS animals showed similar magnetic contrast as wildtype controls that was reduced in 120 day ALS animals (Figure 5, top left). Similar trends were observed with immunohistochemistry staining for TTC (Figure 5, top right). Sections taken from MRI images and immunohistochemistry staining from 90 day ALS animals showed visibly similar intensity and localization as those from 60 day ALS and wildtype mice (data not shown).

Images from injected animals (n=3-4 in each group) were analyzed using ImageJ software to generate a histogram of known signal intensity in each lumbar horn and

grouped into 256 bins of equal size. This data was then processed in Matlab to fit each histogram to a normal distribution function, and the mean distribution value was used to compare different samples. Data was sorted such that paired values were always expressed as a ratio of the positive side to the negative side and expressed as a normalized ratio. MRI images showed no differences between wildtype, 60 day ALS, and 90 day ALS mice, but a significant reduction in intensity for 120 day ALS mice ( $p < 0.001$ ). Images processed from immunohistochemistry stains showed no difference between wildtype and 60 day ALS mice, but a reduction in signal intensity for 90 day ALS mice relative to wildtype ( $p < 0.001$ ) and reduced for 120 day ALS mice relative to both wildtype and 60 day ALS mice ( $p < 0.001$ ). Normalized signal ratios were higher for immunohistochemistry results than MRI, possibly a result of signal amplification during primary and secondary antibody incubation. These results taken together suggest that there are changes in axonal retrograde transport intensity that can be quantified throughout ALS disease progression. It should also be noted that TTC is transported via fast retrograde transport, which has previously been shown to not be impaired during ALS disease progression. These data suggest that there may be differences in the mechanism of transport for molecules that via fast axonal transport that remain unknown.

### **2.5.0 Conclusions**

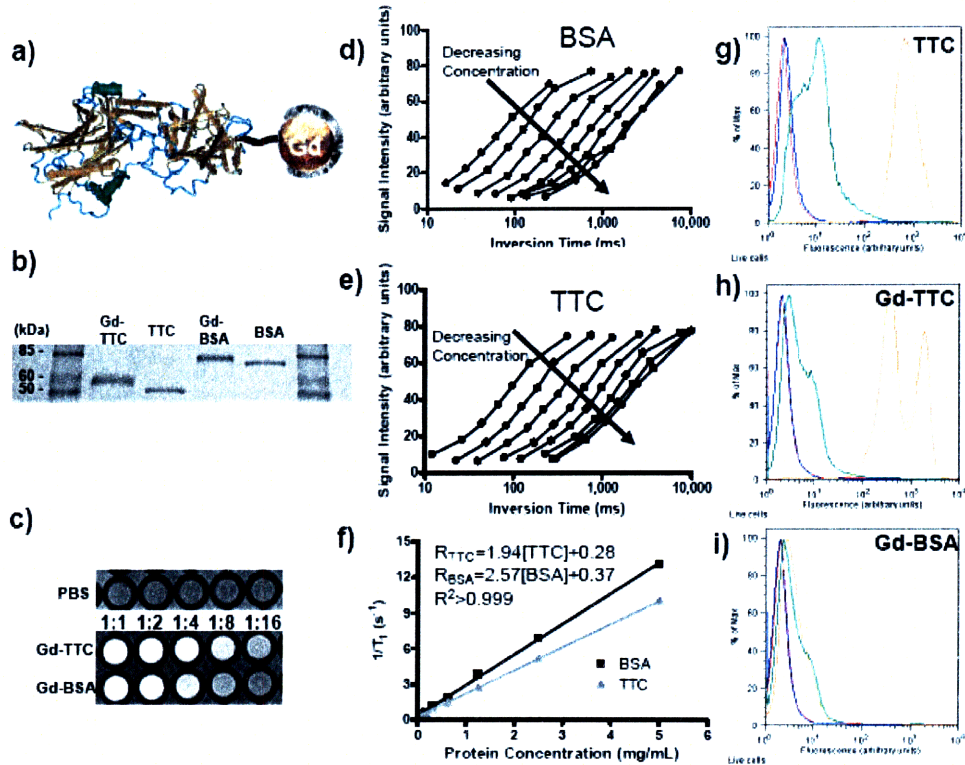
We have developed a novel gadolinium tetanus toxin C fragment conjugate (Gd-TTC) that was characterized by gel electrophoresis, MRI relaxivity, and *in vitro* cell binding to N18-RE-105 neuroblastoma cells. Gd-TTC was retrogradely transported from peripheral muscle to the spinal cord following a unilateral injection in mice as evidenced by 9.4T live animal *in vivo* and 14T *ex vivo* MRI imaging and immunohistochemistry staining for TTC and NeuN of the spinal cord. H&E staining and biodistribution studies showed that Gd-TTC was well tolerated and bioavailable. We conducted a proof-of-concept study and showed that the Gd-TTC conjugate could be used to quantify differences in retrograde transport that were observed in the ALS transgenic mouse model during the disease progression. The Gd-TTC conjugate could provide a biomarker for neurodegeneration and make earlier diagnostics possible.

### **2.6.0 Acknowledgements**

We would like to thank Sharon Gerecht, Martin Schulz, and Gilad Evrony for helpful suggestions during the course of this study. Seth Townsend was supported by a National Science Foundation Graduate Research Fellowship. This work was supported by grants from Project ALS and CIMIT.

## 2.7.0 Figures and Figure Legends

Figure 1



2.7.1 Figure 1 – Synthesis and characterization of Gd-TTC: (a) Schematic of gadolinium tetanus toxin C fragment contrast agent (not drawn to scale) showing stable amine site conjugation. (b) Coomassie blue staining of Gd-TTC, TTC, Gd-BSA, and BSA with protein standard after gel electrophoresis separation showing successful conjugation of a pure product with a narrow size distribution. (c) Visual verification of magnetic contrast of conjugates in a 96-well plate pulsed with a 90-180-90 inversion recovery MRI protocol using a 1.5T magnet. Concentrations for each sample ranged from 3mg/mL to 190uL/mL in 1:2 dilutions. PBS was placed in wells around all samples to minimize artifact from plate inhomogeneities. (d-e) Magnetic relaxivity curves for Gd-TTC (d) and



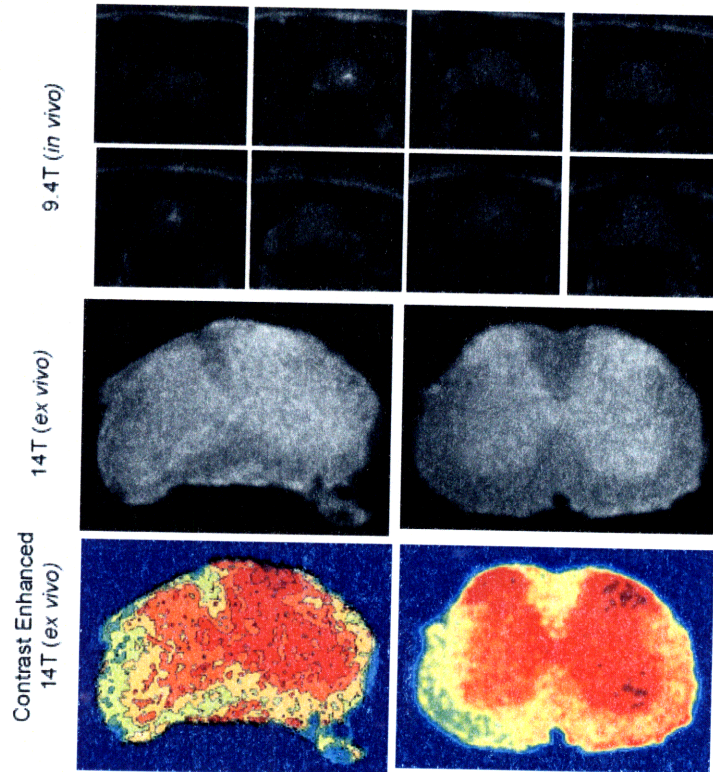
Gd-BSA (e) as measured using a modified NMR-Mouse. Concentrations for each sample ranged from 5mg/mL to 40ug/mL in 1:2 dilutions. (f) Linear fit analysis for Gd-BSA (black) and Gd-TTC (gray) for concentration dependent T1 values as determined for each relaxivity value determined by the following equation:  $M_z(TI) = M_z(1 - e^{-TI/R_1})$ ;  $T_1 = 1/R_1$ .

Linear behavior in both contrast agents indicates the absence of free gadolinium in solution and successful conjugation. (g-i) Flow cytometry analysis of N18-RE-105 neuroblastoma cells after incubation on ice with TTC (g), Gd-TTC (h), and Gd-BSA (i) and PBS (red), mouse monoclonal antibody against TTC (blue), secondary anti-mouse fluorescent antibody (green), and monoclonal and secondary antibody (orange) with appropriate washes, showing that gadolinium conjugation to TTC preserves neuroblastoma binding.





Figure 2

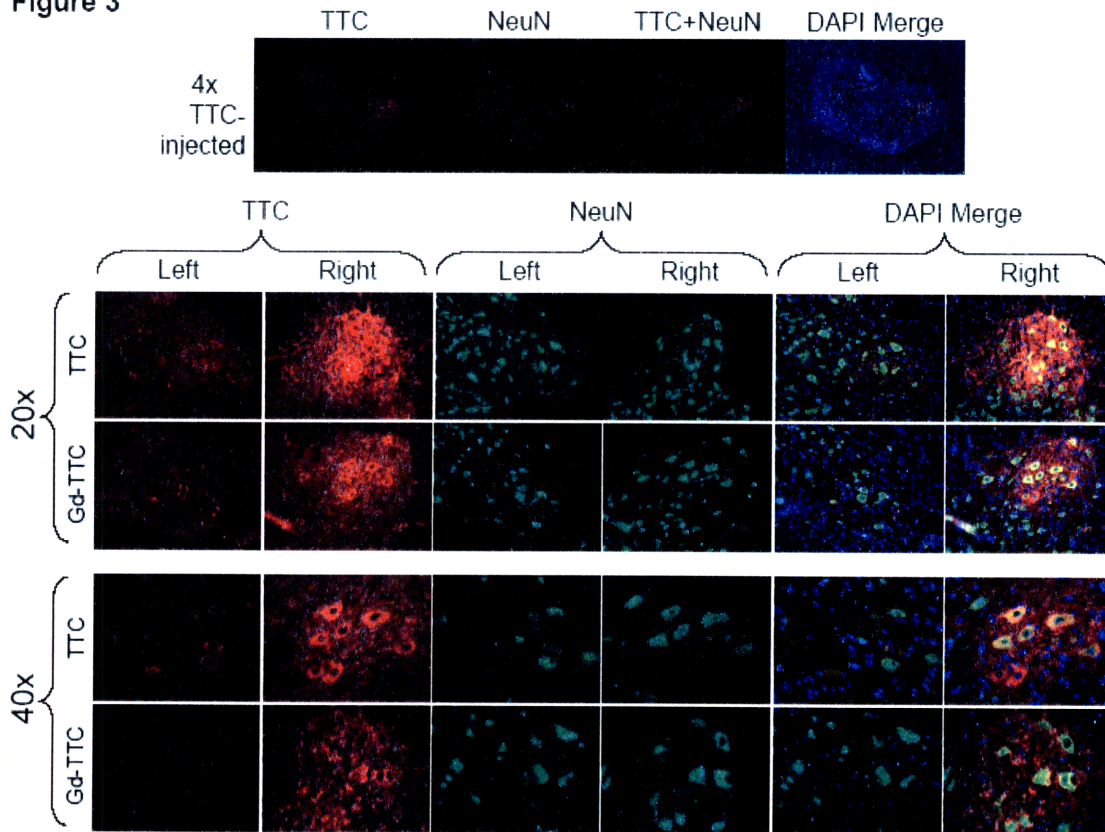


2.7.2 Figure 2 –MRI imaging of Gd-TTC injected wildtype mice: (Top) Live animal (anesthetized) *in vivo* imaging of a mouse spinal cord 24 hours following a unilateral quadriceps injection of Gd-TTC showing regions of enhanced contrast. Images were obtained using a 9.4T MRI and were the result of six averages scanned with T<sub>1</sub>-weighted scan with a TE of 1000ms, a TR of 14.8ms, 1mm interslice average, a field of view of 1.4cm x 1.4cm, and a resolution of 256x256. (Middle, Bottom) Representative high resolution (*ex vivo*) images of excised spinal cords removed from mice 48 hours following a unilateral quadriceps injection of Gd-TTC. Images were obtained using a 14T MRI and were the result of six averages scanned with a TE of 300ms, a TR of 3.4ms, 0.85mm interslice average, a field of view of 9.5mmx9.5mm, and a resolution of 256x256 (middle). (bottom) Images were processed using Matlab to highlight regions of



equal magnetic contrast intensity for 10 isolines (left) and for 50 isolines (right) to show relative localization and intensity of the contrast agent. Magnetic contrast is visible in the ventral horn in the lumbar section of the spinal cord.

**Figure 3**

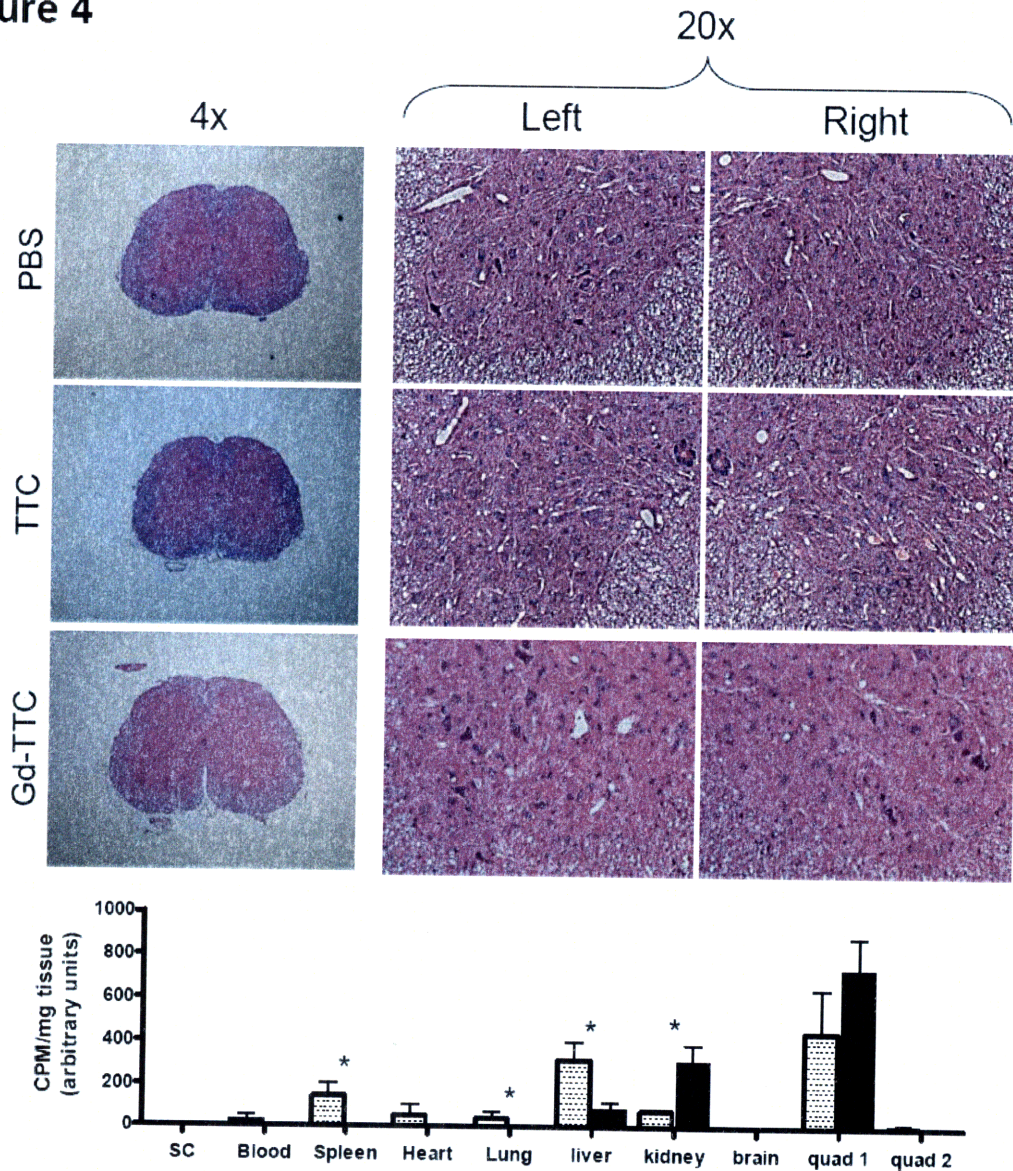


*2.7.3 Figure 3 – Immunohistological staining for TTC:* Mice were injected unilaterally with TTC or Gd-TTC and sacrificed 48 hours post injection. The lumbar spinal cord was sectioned and stained for TTC (red), NeuN (green), and DAPI (blue). Images were obtained at 4x magnification (top), 20x magnification (middle) and 40x magnification (bottom) that were centered on each side of the ventral horn of the spinal. TTC stained sections (left) show a high level of asymmetry between the right side and the left side of



the spinal cord in both TTC and Gd-TTC. NeuN staining was similar between TTC and Gd-TTC injected mice (middle). Merged images showed that TTC and NeuN positive staining were co-localized suggesting specific neuronal uptake of Gd-TTC that exhibits similar properties as TTC.

**Figure 4**





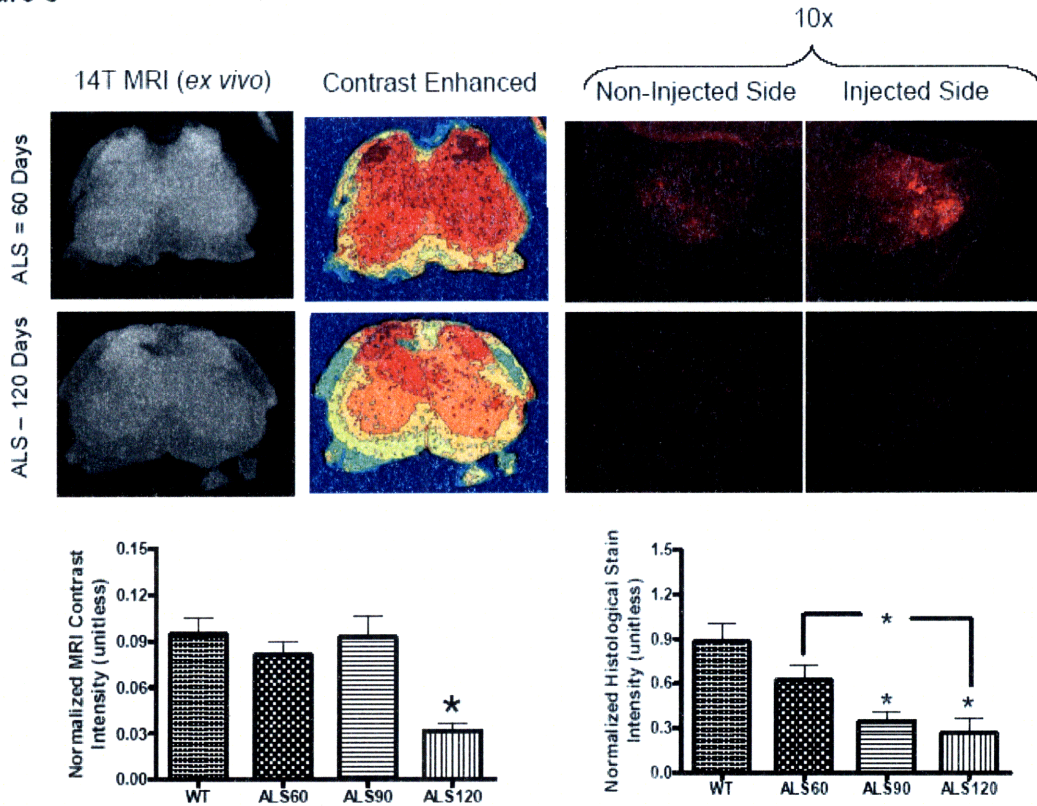
*2.7.4 Figure 4 – Haematoxylin and Eosin Staining and in vivo biodistribution: (Top)*

Mice were injected with PBS, TTC, or Gd-TTC unilaterally and sacrificed 48 hours post injection. Lumbar spinal cords were sectioned, stained with H&E, and imaged for PBS (top), TTC (middle), and Gd-TTC (bottom), at 4x (left) and 20x (right) magnification. No observable asymmetries between the right and left side, or between the each material injected were observed, suggesting only mild acute inflammation at the spinal cord as a result of the TTC or Gd-TTC conjugate injection and transport. (Bottom) Eu-TTC or Eu-BSA were injected unilaterally and mice were sacrificed 48 hours post injection. Tissue from the following tissue was removed, neutron activated, and analyzed for radiolabeled product: spinal cord (SC), blood, spleen, heart, lungs, liver, kidney, brain, injected quadriceps, and uninjected quadriceps. Eu-TTC (black) showed higher levels in the kidney, and lower levels in the liver, spleen, and lungs. Neither Eu-TTC or Eu-BSA were detectable in the spinal cord or brain, suggesting a small amount of overall injected dose is transported to this tissue. A high level of agent remained at the site of injection indicating prolonged opportunity for transport via motor neurons.





Figure 5



2.7.5 Figure 5 – *Gd-TTC* as a biomarker for retrograde transport in ALS mice: (Top left) 14T MRI images of 60 day and 120 day ALS mice 48 hours following a unilateral quadriceps injection of Gd-TTC. A high concentration of Gd-TTC is observed on a single side in the ventral horn at 60 days, with reduced contrast differences after 120 days. (Top right) Mice were immunostained for TTC showing consistent observations and reduced axonal retrograde transport in 120 day ALS animals. (Bottom) Both MRI (left) and immunohistochemistry differences were quantified and expressed as a normal ratio of positive:non-positive signal demonstrating differences in transport efficiency over the ALS disease progression.



## **Chapter 3: Tetanus toxin C fragment conjugated nanoparticles for targeted drug delivery to neurons** <sup>85</sup>

### **3.1.0 Abstract**

The use of nanoparticles for targeted drug delivery is often facilitated by specific conjugation of functional targeting molecules to the nanoparticle surface. We compared different biotin binding proteins (avidin, streptavidin, or neutravidin) as crosslinkers to conjugate proteins to biodegradable nanoparticles prepared from PLGA-PEG-biotin polymers. Avidin gave the highest levels of overall protein conjugation, whereas neutravidin minimized protein non-specific binding to the polymer. The tetanus toxin C fragment (TTC), which is efficiently retrogradely transported in neurons and binds to neurons with high specificity and affinity, retained the ability to bind to neuroblastoma cells following amine group modifications. TTC was conjugated to nanoparticles using neutravidin, and the resulting nanoparticles were shown to selectively target neuroblastoma cells *in vitro*. TTC-conjugated nanoparticles have the potential to serve as drug delivery vehicles targeted to the central nervous system.

### 3.2.0 Introduction

Biodegradable polymers, including polylactic acid (PLA) and poly(lactic-co-glycolic acid) (PLGA), have been used to create nanoparticles and microparticles that encapsulate a variety of therapeutic compounds over time with favorable safety profiles<sup>69</sup>. Polyethylene glycol (PEG) reduces systemic clearance rates *in vivo*<sup>76</sup>, and the functionalization of polymer end groups and subsequent conjugation of targeting moieties (proteins, aptamers, and peptides) permits local drug delivery and reduced systemic toxicity<sup>75</sup>. N-hydroxysuccinimide (NHS) and 1-Ethyl-3-(3-dimethylaminopropyl)-carbodiimide (EDC) are commonly used for protein conjugation and can generate a stable covalent bond. One problem when using this and other similar techniques is the presence of intermediaries with short half lives, which may lead to inefficient conjugations. In contrast, non-covalent interactions between biotin and its binding proteins (avidin, streptavidin, and neutravidin) are highly specific and do not involve unstable intermediaries. Biotin binding proteins have previously been used to conjugate proteins to the surface of microparticles and nanoparticles<sup>144-150</sup>.

A major challenge in treating neurodegenerative diseases is directly delivering therapies to neurons in the central nervous system (CNS). The CNS is difficult to penetrate because it is protected by the blood-brain barrier (BBB)<sup>151</sup>. Recently, nanoparticles synthesized from poly(butylcyanoacrylate) with polysorbate 80<sup>152</sup>, and in separate experiments liposomes conjugated to the antibody to the transferrin receptor, have been used to bypass the BBB<sup>153</sup>.

Retrograde transport from distal axon terminals to the neuronal cell body is an essential process in neurons; it transports enzymes, vesicles, and mitochondria, and is

exploited by viruses and bacterial pathogens as a route to intoxicate motor neurons <sup>154</sup>. It is apparent that retrograde axonal transport of substances from the periphery to motor neuron cell bodies can effectively penetrate the CNS and bypass the BBB <sup>36</sup>. Thus, it may be possible to target nanoparticles to CNS neurons by exploiting retrograde neuronal transport.

One important element in our early studies has been the use of a non-toxic fragment of tetanus toxin, known as tetanus toxin C fragment or TTC <sup>84</sup>. TTC is the neuronal binding portion of the native tetanus toxin. TTC demonstrates extremely high affinity binding to the neuronal ganglioside GT1<sub>b</sub>, that is the tetanus receptor, which is located selectively on the surfaces of neurons <sup>155</sup>. Moreover, once TTC binds to neurons, it is readily endocytosed and efficiently carried via retrograde transport from the distal axonal terminus to the neuronal cell body <sup>155, 156</sup>.

In this report, we compare the ability of different biotin binding proteins (avidin, streptavidin, and neutravidin) to specifically conjugate a protein to the surface of PLGA-PEG-biotin nanoparticles. We describe the use of TTC conjugated PLGA-PEG-biotin nanoparticles as a drug delivery system that selectively targets neuronal cells *in vitro*. This system may have applications for delivering therapeutics to neurons affected by neurodegenerative diseases and may allow retrograde transport delivery to the central nervous system.

### 3.3.0 Methods

*3.3.1 Preparation of PLGA-PEG-COOH:* One gram of PLGA-COOH (20kDa MW, Lactel Absorbable Polymers) was dissolved in 4mL dichloromethane and stirred at RT in the presence of NHS (1:8 PLGA:NHS molar ratio) and EDC (1:8 PLGA:EDC molar ratio) to form an amine reactive ester. Unreacted NHS and EDC were removed using a solution containing 70% ethyl ether and 30% methanol. Trace solvents were removed under vacuum for 2 hours. The polymer was re-dissolved in 5 mL chloroform and incubated under gentle stirring overnight with HCl.NH<sub>2</sub>-PEG-COOH (3400MW, Nektar Therapeutics) or NH<sub>2</sub>-PEG-Biotin (3400MW, Laysan Bio) (1:1.3 PLGA:PEG molar ratio). N-Ethyl-diisopropylamine (DIEA) was also added to the HCl.NH<sub>2</sub>-PEG-COOH solution. The polymer was washed with methanol to remove unreacted PEG. The final PLGA-PEG-COOH/Biotin product was recovered using ethyl ether, vacuum dried for 2h, and stored at -20°C until use.

*3.3.2 NMR analysis:* Polymer was dissolved in deuterated chloroform (5-10mg/mL) and placed in a glass NMR tube. Polymer was analyzed on a Bruker Avance 400Mhz NMR spectrometer using standard proton NMR to verify PEG conjugation to PLGA. Samples were analyzed for the presence of any intermediary products and to quantify the extent of conjugation.

*3.2.3 Preparation of nanoparticles (nanoprecipitation):* Ten milligrams of PLGA-PEG-COOH or PLGA-PEG-biotin was dissolved in 1.5mL acetone, and fluorescent nanoparticles were made by also adding 200ul of coumarin-6 (1mg/mL in acetone, Sigma

Aldrich)<sup>157</sup>. Nanoparticles made of different mixtures of –COOH and –Biotin polymers were prepared in the same way, similarly to methods previously described<sup>158</sup>. Five aliquots of 0.3 mL of the polymer solution were continuously injected with a glass syringe to each of five stirring vials of 0.9 mL deionized water to form nanoparticles. The tip of the syringe was submerged during particle formation. The vials were pooled, the acetone solvent was evaporated at RT for 1h, and nanoparticles were briefly centrifuged (2000rcf, 10 seconds) to remove any visible aggregates. Nanoparticles were concentrated and washed to remove any remaining acetone in an Amicon Ultra-4, 100kDa centrifugal filter (Millipore). Particles were redissolved in a minimal volume of water and stored at 4°C until use.

*3.3.4 Protein attachment to nanoparticles:* Five hundred microliters of nanoparticle solution (~20mg polymer/mL) was incubated with 2mL avidin (Invitrogen) solution (2mg/mL) and gently stirred for 30 minutes at RT to allow avidin conjugation to the nanoparticle. Neutravidin (Pierce Biotechnology) or streptavidin (Invitrogen) were used analogously for experiments using these as the crosslinker. Nanoparticles were washed and free biotin binding protein was removed by 3 centrifugal washes (4,000rcf, 25C, ~10 minutes) in an Amicon filter. Nanoparticles were resuspended in 500uL of water, and biotinylated bovine serum albumin (BSA) or TTC (2mg/mL in PBS) were incubated with the nanoparticles at RT under gentle stirring. Product was washed 3 times with PBS by centrifugation using an Amicon filter (4,000rcf, 25C, ~20 minutes) to remove unbound protein. Nanoparticles were resuspended in a minimal volume of PBS and stored at 4°C until analysis. For all free biotin conjugation experiments, free biotin was mixed with

biotinylated TTC in different concentrations, and conjugated analogously. All fluorescent measurements were made on a 1420 VICTOR3 plate reader (Perkin Elmer) and read in a 96-well plate in triplicate.

*3.3.5 Preparation of BSA-FITC and TTC-FITC:* Ten milligrams of BSA was dissolved in PBS (10mg/mL) or 1mg of TTC was dissolved in PBS (2mg/mL), and incubated with EZ-Link NHS-FITC (Pierce Biotechnology) (1-24:1 FITC:protein molar ratio) under gentle stirring for 2h at RT. Reacted product was collected using a Zeba Desalt Spin Column (Pierce Biotechnology), according to manufacturer's directions.

*3.3.6 Biotinylation of BSA and TTC:* Ten milligrams of BSA was dissolved in PBS (10mg/mL) or 1mg of TTC was dissolved in PBS (2mg/mL), and incubated with EZ-Link NHS-PEG<sub>4</sub>-biotin (Pierce Biotechnology) under gentle stirring for 2h at RT. Reacted product was collected using a Zeba Desalt Spin Column (Pierce Biotechnology), according to manufacturer's directions. Biotinylated BSA was incubated at a ratio of 20:1 NHS-PEG<sub>4</sub>-biotin:BSA and biotinylated TTC was incubated at a ratio of 10:1 NHS-PEG<sub>4</sub>-biotin:TTC in all experiments unless otherwise noted.

*3.3.7 Biotinylation quantification:* The extent of BSA and TTC biotinylation was determined using a HABA-biotin quantification assay (Pierce Biotechnology), according to manufacturer's directions. Briefly, the absorbance of the HABA-avidin solution was measured at 500nm. 100uL of biotinylated BSA or TTC was then added to 900ul of the HABA-avidin solution, and the absorbance at 500nm measured again. The molar



concentration of biotin was calculated from the difference in absorbance after adding biotinylated BSA, using a HABA-avidin extinction coefficient of  $34,000 \text{ M}^{-1} \text{ cm}^{-1}$ <sup>159</sup>. The extinction coefficient for TTC was calculated by measuring the absorbance at 280nm of a solution of biotinylated TTC whose concentration was measured by a micro BCA assay (Pierce Biotechnology). The absorbance at 280nm was confirmed to be linearly dependent on concentration using a series of TTC dilutions. The molar concentrations of biotinylated BSA and TTC were determined by measuring the absorbance of the protein solution at 280nm, and calculated using an extinction coefficient of  $43,824 \text{ M}^{-1} \text{ cm}^{-1}$  for BSA and the empirically derived extinction coefficient for TTC. The average number of biotins conjugated to BSA and TTC was calculated as the ratio of biotin concentration to biotinylated BSA/TTC concentration. All absorbance measurements were made on a SpectraMax Plus 384 spectrometer (Molecular Devices) and read in a cuvette in triplicate.

*3.3.8 Nanoparticle characterization and schematic:* Nanoparticle size and zeta potential properties were characterized using a ZetaPALS dynamic light scattering instrument (Brookhaven Instruments Corporation) as previously described<sup>158</sup>. 3D schematics of the nanoparticle and conjugation system were created using CN3D (NCBI) and 3ds Max (Autodesk) software.

*3.3.9 Flow cytometry:* Cells were analyzed using a FACScan flow cytometer (Becton Dickinson) to measure fluorescence (488nm excitation, 530nm and 650nm emission). Cells were incubated with propidium iodide (5ug/mL), and cell populations were gated

based on forward/side scatter and propidium iodide fluorescence to remove debris and dead cells from analysis. A total of at least 10,000 gated events were obtained for each sample. Data was analyzed using FlowJo software (Tree Star) to generate histograms of each sample.

*3.3.10 Cell culture:* N18-RE-105 neuroblastoma, b.End3 brain endothelial, and HepG2 liver cells were grown with previous methods as those previously described<sup>160-162</sup>. Briefly, neuroblastoma cells were cultured in DMEM and supplemented with HAT supplement (100uM sodium hypoxanthine, 400nM aminopterin, 16uM thymidine), 10% FBS, and 1% penicillin/streptomycin. HepG2 and b.End3 cells were grown in MEM and DMEM, respectively, containing 10% FBS and 1% penicillin/streptomycin. All cells were grown in filtered flasks in an incubator at 95% air and 5% carbon dioxide. Media was changed every 48 hours, and cells were passaged with EDTA-trypsin when confluent. All media reagents were purchased from Invitrogen. HepG2 and b.End3 cells were purchased from ATCC, and N18-RE-105 cells were a generous gift of Dr. Jonathan Francis at the Massachusetts General Hospital.

*3.3.11 Statistics:* An ANOVA analysis was conducted for all multiple point analysis, and a Student's t-test was used for all statistical analysis between two groups, unless otherwise indicated. A p-value less than 0.05 was considered significant. Results are expressed as mean  $\pm$  SD unless otherwise indicated.

## 3.4.0 Results and Discussion

### 3.4.1 Biotin binding proteins for nanoparticle conjugation

We used biotin binding proteins to conjugate targeting molecules to the surface of biodegradable nanoparticles for drug delivery (Figure 1a). The conjugation method uses biotin-functionalized PLGA-PEG polymers and biotin binding proteins (avidin, streptavidin, and neutravidin) as crosslinkers for conjugation (Figure 1b)<sup>163-165</sup>. This system has the advantage of conjugating a targeting ligand to the surface of the nanoparticle using highly specific biotin interactions. This may therefore have advantages over other conjugation chemistries that do not distinguish between functional groups that may be present on both the targeting ligand and the encapsulated therapeutic (e.g. primary amines, thiols). Moreover, this system amplifies available protein conjugation sites, because each biotin binding protein has four biotin binding sites, and avoids unstable chemical intermediaries present in other protein conjugation reactions. The bonds formed by the biotin interactions are highly stable, and the system can be universally applied to conjugate other targeting molecules with accessible primary amine groups.

### 3.4.2 NMR characterization

We prepared PLGA-PEG-biotin polymers by a one step synthesis conducted in anhydrous organic solvents. Proton NMR revealed characteristic peaks of PLGA at 1.5 ppm, 4.8 ppm and 5.2 ppm in all PLGA dissolved polymer samples (Figure 1c-f). Peaks were observed at 3.6 ppm in PLGA-PEG-COOH and PLGA-PEG-biotin, corresponding

to the PEG chain (Figure 1e-f). Using the integration of the relative molecular weights and peaks, the conjugation efficiency of NH<sub>2</sub>-PEG-COOH and NH<sub>2</sub>-PEG-Biotin to PLGA-COOH was estimated to be approximately 35%. NMR peaks in some samples were detected at 1.2 ppm and 3.4 ppm and identified as residual diethyl ether (Figures 1d, e, f). Biotin peaks following conjugation were not easily detected, presumably because the relative biotin signal was masked by the signal from the polymer chain, even when a lower MW PLGA polymer was used (~20kDa). This has previously been observed in NMR analysis of high molecular weight polymer chains with end-group conjugation<sup>146</sup>.

### *3.4.3 Protein conjugation to nanoparticles*

To show that biotin was functional and present on the surface of the nanoparticles, we synthesized nanoparticles using a solvent/non-solvent nanoprecipitation method and incubated them with avidin-FITC, followed by centrifugal washes. Nanoparticles were made using either PLGA-PEG-COOH or PLGA-PEG-biotin polymers. Nanoparticles formed from either a carboxyl or biotin end group that were not incubated with avidin-FITC showed baseline fluorescence levels in a fluorescent plate reader, whereas nanoparticles incubated with avidin-FITC had significantly higher binding with biotin-functionalized polymer than carboxylic acid controls (Figure 2a, n=5-6, p<0.01). Subsequent washes reduced but did not eliminate the amount of binding of the avidin-FITC to the PLGA-PEG-COOH, indicating a small amount of non-specific binding, likely a result of electrostatic interactions between the negatively charged polymer and positively charged avidin.

The previous experiments documented that one can conjugate avidin to the surface of a nanoparticle via biotin end-groups. We next tested the possibility that avidin could be used to attach a protein to the nanoparticle. We first conjugated biotin to BSA or TTC in different molar ratios (1:1, 3:1, and 10:1, biotin:protein) and quantified the final number of moles of biotin per mole of protein using a HABA-avidin assay. An empirically derived extinction coefficient of  $75,550 \text{ M}^{-1}\text{cm}^{-1}$  was used for TTC. As predicted, incubation of protein with higher concentrations of NHS-PEG<sub>4</sub>-biotin led to higher overall biotinylation (Figure 2b, ANOVA,  $p < 0.01$ ,  $n = 3$ ). At 10:1 conjugation ratios, TTC showed higher levels of biotinylation than BSA ( $p < 0.01$ ). We therefore used a higher 20:1 molar ratio of NHS-PEG<sub>4</sub>-biotin:BSA and quantified the extent of biotinylation. BSA showed slightly higher but not significant biotinylation for 20:1 than for 10:1 ratios ( $2.2 \pm 0.10$  vs.  $2.0 \pm 0.03$ , ns). For all subsequent experiments, we used protein that was conjugated with a 10:1 biotin:TTC ratio and a 20:1 biotin:BSA ratio.

We then used nonfluorescent avidin and biotinylated BSA-FITC (b-BSA-FITC) to evaluate whether PLGA-PEG-biotin+avidin could be used to conjugate protein to nanoparticles. We incubated nanoparticles with avidin, followed by three washes, and subsequently with biotinylated BSA-FITC followed by three washes (Figure 2c). Nanoparticles prepared from PLGA-PEG-biotin and subsequently incubated with avidin and biotinylated BSA-FITC gave significantly higher fluorescence than negative controls made from PLGA-PEG-COOH polymers or preparations without avidin (Figure 2d, ANOVA,  $p < 0.01$ ,  $n = 6$ ). This suggests that functional biotin is present on the nanoparticle surface, and that this could be used for protein conjugation. This system could be used as

an alternative to NHS/EDC conjugations to avoid unstable intermediaries throughout the conjugation process.

#### *3.4.4 Comparison of different biotin binding proteins*

In the previous experiments, some nonspecific binding of avidin-FITC (Figure 2a) and biotin-BSA-FITC (Figure 2d) to the nanoparticle was observed. We predicted that streptavidin (negatively charged) or neutravidin (an uncharged avidin derivative) may reduce non-specific interactions and binding to the nanoparticle. We added each of these three biotin binding proteins to either PLGA-PEG-COOH or PLGA-PEG-biotin nanoparticles. Biotinylated BSA-FITC was added to nanoparticle preparations after washing out unbound biotin binding protein. The mean fluorescence was measured on independent preparations in triplicate using a fluorescence plate reader (Figure 2e). Nanoparticles with different biotin binding proteins showed various levels of protein binding (ANOVA,  $p < 0.01$ ,  $n = 3-6$ ). As predicted, avidin resulted in high levels of overall protein conjugation to PLGA-PEG-biotin nanoparticles, significantly higher than streptavidin ( $p < 0.01$ ) and neutravidin ( $p < 0.05$ ). Streptavidin and neutravidin fluorescence values were not significantly different. Neutravidin led to relatively high levels of protein conjugation but had lower overall non-specific binding to the nanoparticles than avidin ( $p < 0.01$ ). Surprisingly, streptavidin led to non-specific binding to the nanoparticles and observable nanoparticle aggregation (visual observations). These data suggest that avidin has the advantage of generating high levels of conjugated (both specific and non-specific) protein on nanoparticles, whereas neutravidin leads to highly specific protein conjugation to nanoparticles. Neutravidin was used for all subsequent experiments.

#### *3.4.5 Protein functionality and specificity*

TTC in its native form binds with high affinity and specificity to neurons. To test whether conjugation of small molecules to TTC using NHS chemistry affects TTC protein functionality, we conjugated FITC to TTC using NHS-FITC (1:1, 8:1, and 24:1 FITC:protein molar ratios), and incubated the fluorescent protein with N18-RE-105 neuroblastoma cells, which are known to express the ganglioside (GT<sub>1B</sub>) receptor for TTC. BSA-FITC prepared analogously to TTC-FITC and matched in fluorescence and concentration to TTC-FITC was used as a negative control. In all binding ratios, TTC selectively bound to neuroblastoma cells, whereas BSA did not (Figure 3a-c). The higher binding of BSA at higher fluorescent ratios may be a result of unbound NHS-FITC that was not removed during protein purification. The double peak observed in TTC binding may be a result of a heterogenous cell population that is observed by light microscopy (visual observations). These data demonstrate that TTC preserves its ability to bind to neurons following amine conjugation.

#### *3.4.6 Nanoparticle aggregation*

In the above paradigm, each nanoparticle binds multiple biotin-binding proteins. Moreover, each neutravidin molecule has four biotin binding sites. For this reason, nanoparticle cross-linking was sometimes observed in these experiments<sup>166, 167</sup>. At least two factors determine the propensity toward aggregation: the ratio of free neutravidin to biotin on the nanoparticle surface in the first conjugation step, and the ratio of biotinylated protein to nanoparticle-bound neutravidin in the second conjugation step.

Therefore, we used two approaches to reduce aggregation. The first was to reduce the available numbers of biotin molecules on the nanoparticle surface by creating particles with various mixtures of PLGA-PEG-COOH and PLGA-PEG-biotin in increasing COOH:biotin molar ratios. Nanoparticles prepared from PLGA-PEG-biotin polymers show maximal aggregation at intermediate biotinylated TTC concentrations (<10  $\mu$ M), whereas increasing the PLGA-PEG-COOH molar ratio reduced aggregation at each protein concentration (Figure 3d). Aggregation was not fully eliminated even at very low PLGA-PEG-biotin concentrations, likely a result of some neutravidin non-specific binding to the nanoparticle surface. The second approach we have used to reduce aggregation is to competitively bind free biotin to neutravidin binding sites during the biotin-TTC conjugation step. Increasing free biotin reduced aggregation and eliminated aggregation at high free biotin concentrations (Figure 3e). We again note that increasing concentrations of biotin-TTC also reduced but did not eliminate aggregation. For subsequent experiments, we used 1.6 $\mu$ M free biotin and added TTC in excess of this amount to reduce nanoparticle size, while ensuring that TTC was bound to the nanoparticle surface.

#### *3.4.7 In vitro cell specificity*

We tested the ability of TTC to serve as a targeting protein for specific nanoparticle delivery to neurons. We prepared PLGA-PEG-biotin nanoparticles encapsulating fluorescent coumarin-6 and conjugated TTC to their surface.

Neuroblastoma cells were incubated with these nanoparticles as well as negative controls (without both neutravidin and TTC, without TTC, without neutravidin, and with BSA



instead of TTC). Cells were analyzed using flow cytometry and shown to be significantly more fluorescent with TTC conjugated nanoparticles than any negative control (Figure 4a). Hep G2 liver (Figure 4b) or b.End3 endothelial cells (Figure 4c) were incubated with TTC-conjugated or BSA-conjugated (negative control) nanoparticles. Both specific and non-specific uptake ratios are summarized on Table 1. Non-specific binding or uptake was observed in all cell types, which is consistent with previous cell targeting studies using different ligands<sup>168-170</sup>. This is possibly due to background levels of fluorescent nanoparticles that remain after cell washes. Although non-specific binding was observed, non-specific delivery of nanoparticles delivering therapeutic agents alone may not be sufficient for efficacy, necessitating targeted delivery that may increase uptake by specific cell types. The benefit of PEG is most clear in previous studies during *in vivo* studies where PEG has been shown to increase nanoparticle half life by reducing systemic clearance rates<sup>171</sup>. TTC-conjugated nanoparticles showed high selectivity for neuroblastoma cells, indicating that TTC-conjugated nanoparticles may be useful for selective targeting of neurons. Because of the native properties of TTC, these nanoparticles may allow for retrograde transport and provide a drug delivery system to specifically target neurons.

#### 3.4.8 Characterization of nanoparticles

Nanoparticle properties were characterized using dynamic light scattering (DLS) to give size, polydispersity, and zeta potential in each preparation (see Table 2). PLGA-PEG-COOH nanoparticles were not significantly different than PLGA-PEG-biotin nanoparticles in size, but were more negative in zeta potential (n=3, p<0.05), presumably

due to fewer COOH groups in biotin-conjugated nanoparticles. Nanoparticles showed a slight increase in size upon addition of neutravidin, and the addition of the biotinylated protein further increased the size of the nanoparticles.

### **3.5.0 Conclusions**

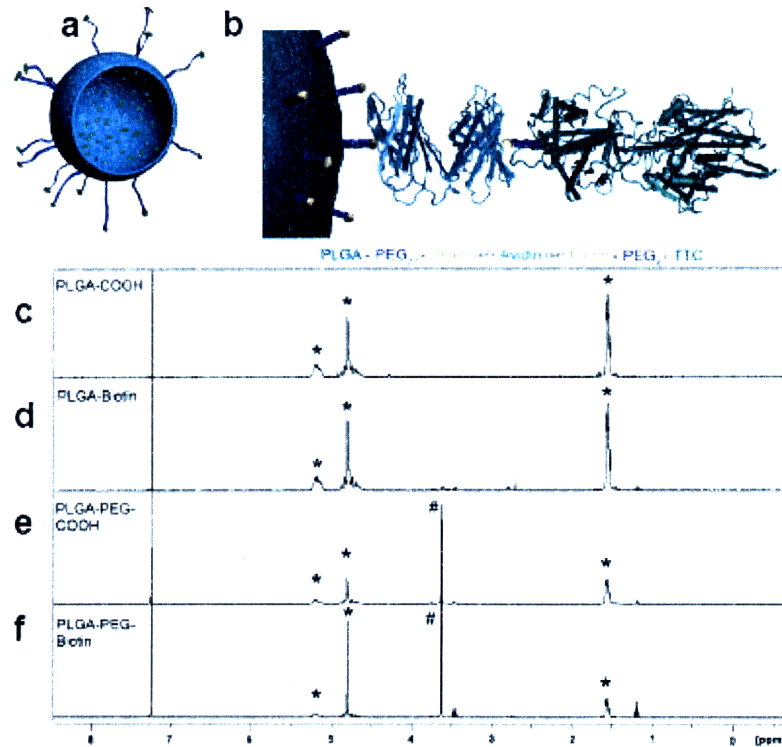
We developed nanoparticles from PLGA-PEG-biotin polymers and used biotin binding proteins (avidin, streptavidin, or neutravidin) as crosslinkers for protein conjugation. The tetanus toxin C fragment was modified and conjugated to nanoparticles, allowing targeted binding to neuroblastoma cells, while not targeting liver or endothelial cells.

### **3.6.0 Acknowledgements**

We would like to thank Greg Zugates, Benjamin Teply, Erin (Xiaolu) Wei, Jonathan Francis, Etgar Levy-Nissenbaum, Sharon Gerecht, and Glenn Paradis and the MIT Center for Cancer Research flow cytometry core facility for technical guidance. Spectroscopic instrumentation at the MIT DCIF is maintained with funding from NIH Grant 1S10RR13886-01 and NSF Grants CH3-9808063, DBI9729592, and CHE-9808061. This work was supported by funding from the Pierre de Bourgnecht ALS Research Fund, Angel Fund, Project ALS, the Pape Adams Fund, and NIH Grants DE16516 and HL60435. Seth Townsend is supported in part by a National Science Graduate Research Fellowship. Gilad Evrony was supported in part by the John Reed Fund at MIT.

### 3.7.0 Tables and Figures

**Figure 1**



3.

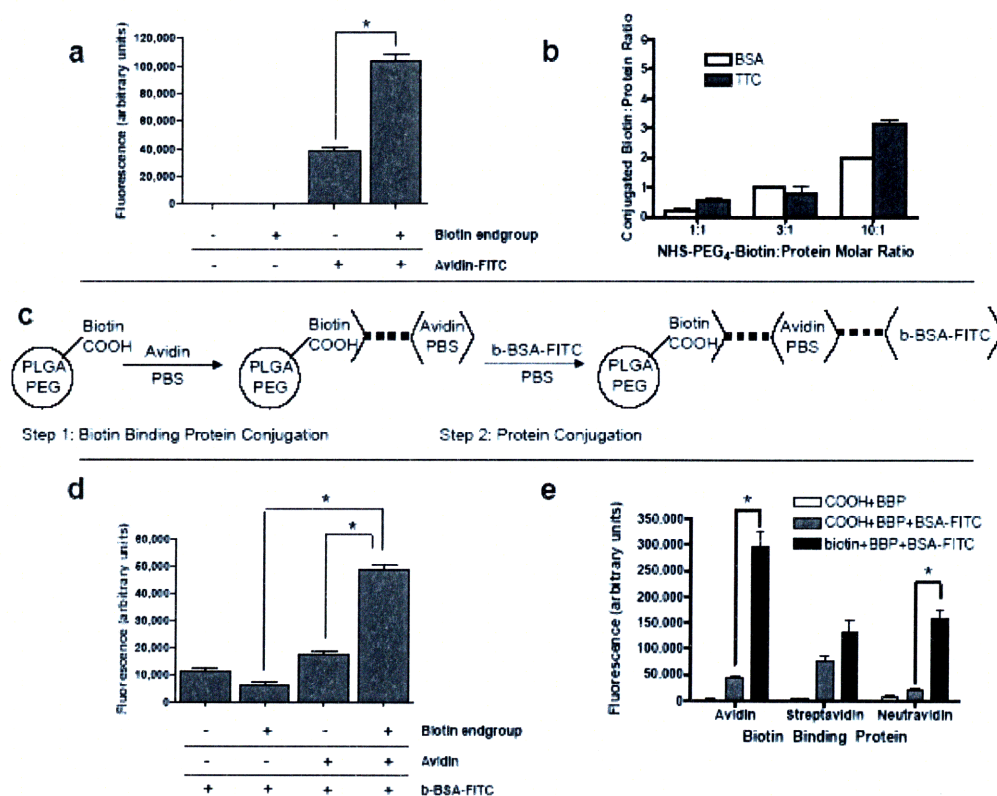
*7.1 Figure 1: Protein conjugation to nanoparticles using biotin binding proteins.*

Conceptual schematic (not to scale) illustrating (a) the cross-section of a biodegradable polymer nanoparticle that is functionalized with the tetanus toxin C fragment (TTC) and presumed to encapsulate a therapeutic substance, and (b) the conjugation system used to attach functional TTC to the nanoparticle utilizing PLGA-PEG-biotin functionalized biodegradable polymer, and biotinylated TTC with an avidin cross-linker, based on previously published structures<sup>163-165</sup>. Two of the four avidin subunits are shown for illustrative purposes. Proton NMR spectra of (c) PLGA-COOH, (d) PLGA-biotin, (e) PLGA-PEG-COOH, and (f) PLGA-PEG-biotin polymers dissolved in deuterated



chloroform. Characteristic peaks are visible for PLGA (\*) and PEG (#), but not for conjugated biotin.

**Figure 2**

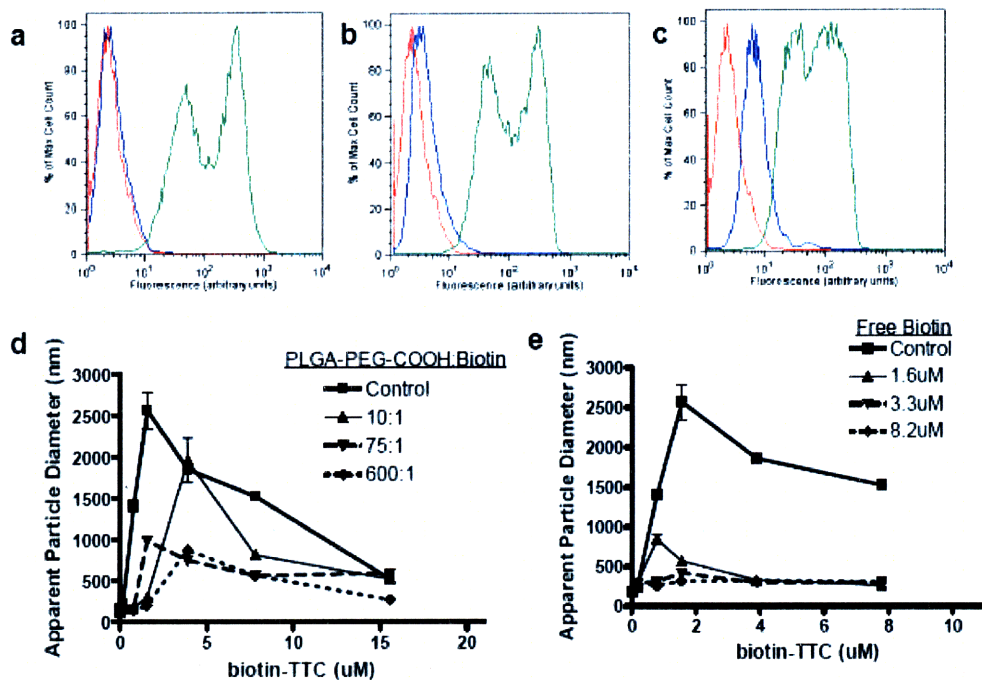


3.7.2 *Figure 2: Protein conjugation to PLGA-PEG-biotin nanoparticles.* (a) PLGA-PEG-COOH (-) and PLGA-PEG-biotin (+) nanoparticles incubated with the presence (+) or absence (-) of avidin-FITC and analyzed on a fluorescent plate reader. (b) Quantified extent of biotinylation for BSA (white) and TTC (gray) proteins for different NHS-PEG<sub>4</sub>-biotin:protein molar ratios. (c) Schematic representation of overall protein conjugation to PLGA-PEG-COOH or PLGA-PEG-biotin polymer nanoparticles (as indicated). Avidin (Step 1) and biotinylated BSA-FITC (Step 2) were conjugated in sequence to the nanoparticle surface, with PBS washes to remove unbound protein at each step. (d)



PLGA-PEG-COOH (-) and PLGA-PEG-biotin (+) nanoparticles incubated with the presence (+) or absence (-) of avidin, subsequently incubated with biotinylated BSA-FITC (b-BSA-FITC) and analyzed on a fluorescent plate reader showing selective protein conjugation to nanoparticles. (e) Comparison of biotin binding proteins (BBP) as crosslinkers for protein conjugation to nanoparticles. Data is expressed as mean  $\pm$  SEM. PLGA-PEG-COOH (white, gray) and PLGA-PEG-biotin (black) nanoparticles were prepared and incubated with avidin (left), streptavidin (middle), or neutravidin (right), and subsequently with biotinylated BSA-FITC. Avidin showed the highest overall protein conjugation, whereas neutravidin resulted in reduced non-specific interaction and the most specific protein conjugation.

Figure 3



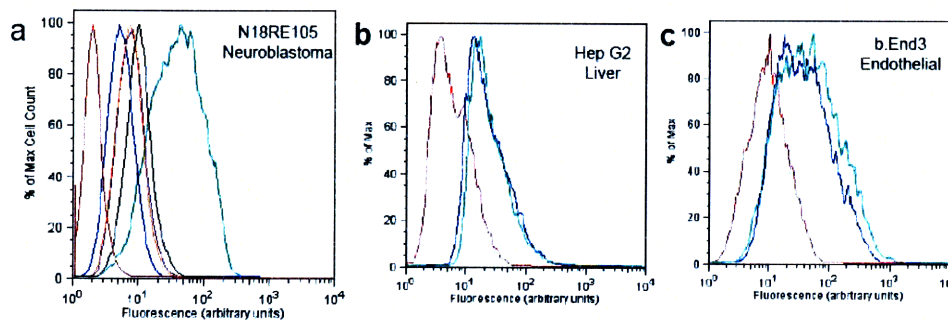
3.7.3 Figure 3: TTC protein functionality and nanoparticle size optimization. Flow cytometry analysis of N18-RE-105 neuroblastoma cells incubated with fluorescent TTC





(green), fluorescent BSA (blue), or PBS control (red), for NHS-FITC:protein conjugation ratios of 1:1 (a), 8:1 (b), and 24:1 (c). TTC remained functional following amine conjugation and preserved its ability to target neurons (a-c). Dynamic light scattering analysis of nanoparticle size following conjugation with neutravidin and biotinylated TTC (d-e). (d) Nanoparticles prepared with different molar ratios of PLGA-PEG-COOH to PLGA-PEG-biotin as indicated (control is 100% PLGA-PEG-Biotin), and (e) free biotin competition with TTC-biotin conjugation to nanoparticles at different concentrations of free biotin as indicated; control is without free biotin. These figures show that nanoparticle aggregation can be reduced by decreasing the number of biotins on the nanoparticle surface (d) or by free biotin competition during conjugation of the biotinylated protein (e). For all sizing experiments, results are expressed as mean $\pm$ SD of 3 independent size measurements of one preparation of nanoparticles.

**Figure 4**



3.7.4 *Figure 4: In vitro cell binding of TTC-conjugated nanoparticles.* Flow cytometry analysis of N18-RE-105 neuroblastoma cells (a), HepG2 liver (b), and b.End3 endothelial (c), cells following incubation with TTC-conjugated nanoparticles (green), BSA-conjugated nanoparticles (blue), or a PBS negative control (red). Other negative controls



are shown for (a) for nanoparticles without neutravidin (purple), without TTC (orange), and blank nanoparticles (black), demonstrating that TTC-conjugated nanoparticles selectively target neurons.

**Table 1**

	N18-RE-105 Neuroblastoma	Hep G2 Liver	b.End3 Endothelial
Non-Specific Uptake ratio (BSA/PBS)	2.76	4.31	4.99
Specific Uptake Ratio (TTC/PBS)	25.50	4.87	6.83

*3.7.5 Table 1: Nanoparticle binding to cells.* Summary of figure 4 flow cytometry analysis for N18-RE-105 neuroblastoma, HepG2, and b.End3 cells incubated with TTC or BSA conjugated fluorescent nanoparticles and PBS (negative control). The specific (TTC) and non-specific (BSA) uptake ratios show the fluorescence ratio of conjugated nanoparticles to PBS treated negative controls. Results are expressed as mean fluorescence of each gated live cell population. Each sample represents an analysis of at least 10,000 live gated cells.

**Table 2**

	Mean Size (nm)	Zeta Potential (mV)	Polydispersity Index
PLGA-PEG-COOH	135.7(1.1)	-32.07(3.19)	0.137(0.023)
PLGA-PEG-biotin	111.1(1.8)	-23.28(1.17)	0.227(0.006)
PLGA-PEG-biotin+NA	144.1(2.4)	-0.497(0.402)	0.198(0.012)
PLGA-PEG-biotin+NA+BSA	175.3(2.3)	-3.37(3.86)	0.226(0.012)
PLGA-PEG-biotin+NA+TTC+free biotin	255.2(6.3)	-5.85(5.00)	0.219(0.007)

3.7.6 *Table 2: Nanoparticle characterization.* Size, charge zeta potential, and polydispersity index for each nanoparticle preparation indicated as determined by dynamic light scattering. Results are expressed as mean (SD) for 3 size and zeta potential measurements.



## **Chapter 4: A porous photocurable elastomer for cell encapsulation and culture**<sup>172</sup>

### **4.1.0 Abstract**

Tissue engineering utilizing stem cells has the potential to provide new therapeutics for amyotrophic lateral sclerosis (ALS, or Lou Gehrig's disease). Encapsulating cells within a polymer matrix creates a three-dimensional (3D) scaffold that may more accurately represent the native microenvironment and cell organization and may support neuronal culture. Here we report a porous scaffold prepared from a photocurable elastomer, poly(glycerol-co-sebacate)-acrylate (PGSA). The scaffold porosity, swelling, mass loss, toxicity and mechanical properties, suggest that porous PGSA could be used to support the growth and differentiation of encapsulated cells. Neuroblastoma (NB) and human embryonic stem cells (hESCs) were encapsulated into the matrix and found to adhere to the material and interact with each other within 24 hours. After 7 days, encapsulated NB cells were found to grow, and form matrix fibrils and tissue. Undifferentiated hESCs proliferated and differentiated in the PGSA scaffold. In vivo experiments showed that both porous scaffolds have similar biocompatibility profiles as non-porous PGSA, but porous PGSA promotes tissue ingrowth, as compared to non-porous PGSA. We therefore propose that porous PGSA scaffolds can provide a logistical template for 3D growth of cells and tissue engineering.

## 4.2.0 Introduction

Tissue engineering of neurons may lead to more effective treatments for amyotrophic lateral sclerosis (ALS, or Lou Gehrig's disease). This could be accomplished either *ex vivo* or *in vivo*, the later of which would require that the cell microenvironment support neuronal growth and proliferation. It is well-established that differences exist between cells grown in two dimensional (2D) culture and cells found in their native 3D environment, where cells interact with each other and the extracellular matrix (ECM) to form tissue. These interactions lead to well established differences in cell signaling, gene expression, and cellular organization<sup>173-176</sup>. Furthermore, it is increasingly accepted that physical cues play a role in cell growth and tissue assembly<sup>177, 178</sup>. These signals are important in stem cells (SCs) during self renewal, proliferation, and differentiation.

Stem cells have great potential both as a source of cellular tissue for regenerative medicine and for investigating fundamental concepts in developmental biology<sup>179, 180</sup>. Three-dimensional scaffolds can be used to provide a structural and logistic template for SC attachment, growth and differentiation. These may more accurately mimic some aspects of both chemical and physical signals and the native local microenvironment of SCs<sup>116, 181, 182</sup>.

Various methods have been used to culture cells in a 3D environment, including seeding or encapsulating cells into biomaterials. Scaffolds prepared from biodegradable polymers (e.g. PLGA) are commonly used for cell seeding, but cell density throughout the matrix may not be uniform and may affect cell fate and differentiation<sup>117-120</sup>. Encapsulating cells within a biodegradable scaffold may lead to a more uniform cell



distribution<sup>183</sup>. Hydrogels are highly hydrated matrices prepared from either natural or synthetic material networks that are widely used for embedding cells in a 3D environment<sup>184</sup>. In many applications, it is desirable to use scaffold prepared from polymers with material properties that resemble those of the native ECM, a soft, tough, and elastomeric network that provides mechanical stability and structural integrity to cells.

Bioelastomer materials may provide a flexible scaffold for 3D culture of cells<sup>185</sup>. In our previous studies, poly(glycerol sebacate) (PGS) was developed and shown to be biocompatible both *in vitro* and *in vivo*<sup>121, 122</sup>. A recent modification to PGS incorporated acrylate groups into the polymer backbone that allowed for photopolymerization while preserving the elastic and biocompatibility properties of PGS<sup>186</sup>. Photopolymerization has been used as a means to encapsulate and support both mature cells and human embryonic stem cells (hESC)<sup>187-191</sup>. This modified elastomer, poly(glycerol-co-sebacate)-acrylate (PGSA), polymerizes to form a uniform scaffold. However, the density and hydrophobicity of the material, which lacks pores, does not allow for rapid diffusion of media and therefore may not be well suited for cell encapsulation. We hypothesized that porous PGSA could be used for cell encapsulation and culture within an elastic scaffold.

### 4.3.0 Methods

*4.3.1 Cell culture and media: hESCs.* Two NIH-registered hESC cell lines were used for all studies (H9 and H13, WiCell Research Institute, Madison, WI; p19-30). Human ESCs were grown on an inactivated mouse embryonic fibroblast (MEF) feeder layer in growth medium (80% KnockOut DMEM, supplemented with 20% KnockOut Serum Replacement, 4 ng/ml basic Fibroblast Growth Factor, 1 mM L-glutamine, 0.1 mM  $\beta$ -mercaptoethanol, 1% non-essential amino acids). Human ESCs were passaged every 4-6 days using 1mg/ml type IV collagenase for 20-30 minutes. Neuroblastoma cells. N18-RE-105 neuroblastoma cells were grown in DMEM supplemented with HAT supplement, 10% FBS, penicillin and streptomycin. Media was changed every 48 hours, and cells were passaged with EDTA-trypsin for 5-7 minutes every 3-5 days when confluent. Embryoid body (EB) media. Encapsulated hESCs were cultured with in EB media (80% DMEM, supplemented with 20% defined FBS, 1 mM L-glutamine, 0.1 mM  $\beta$ -mercaptoethanol, 1% non-essential amino acids). All media components and reagents for both hESCs and neuroblastoma culture were purchased from Invitrogen Corporation (Carlsbad, CA), except for defined FBS, which was purchased from Hyclone (Logan, UT).

*4.3.2 Synthesis of PGSA:* All reagent were purchased from Sigma-Aldrich (St. Louis, MO), PGS and PGSA were prepared as previously described<sup>121, 186</sup>. Briefly, 20g PGS pre-polymer was incubated in a round-bottom flask with 200 mL anhydrous dichloromethane and 20mg 4-(dimethylamino)-pyridine (DMAP). The flask was cooled

to 0 °C under positive N<sub>2</sub> pressure. (0.34\* 78 mmol) Acryloyl chloride and equimolar triethylamine (0.32 mol per mol of hydroxyl groups on the PGS pre-polymer) were slowly added to the flask and stirred for 24 h at RT. The resulting PGSA polymer was dissolved in ethyl acetate, precipitated with ethanol, vacuum oven dried at 45 °C, and stored at -20C until use.

*4.3.3 Formation of porous PGSA scaffolds:* PGSA scaffolds were prepared by mixing the PGSA pre-polymer with 0.1% photoinitiator (2,2-dimethoxy-2-phenyl-acetophenone, wt%) and polymerized using a ultraviolet light (10 mW/cm<sup>2</sup>, model 100AP , Black-Ray ) at RT for 10 minutes. To form PGSA15 and PGSA35 scaffolds, 15 and 35% glycerol (wt%) was mixed with the PGSA pre-polymer containing photoinitiator and polymerized analogously. Polymerization for all scaffolds occurred under sterile conditions using a custom mold. Cylindrical scaffolds containing 25uL of pre-polymer were prepared for both *in vitro* (3mm in diameter, 2mm thick) and *in vivo* (8mm in diameter, 1mm thick) experiments.

*4.3.4 In vitro swelling and material loss:* PGSA samples with 15% and 35% glycerol (wt%) were weighed and incubated in media at 37°C. At time intervals between 1-35 days, the samples were removed from media, blotted, and weighed to record the wet weight. The samples were then oven dried for five days at 60°C and weighed to record the dry weight. Swelling ratios were determined by the following formula:

$SR_t = (W_t/D_t)/(W_{t0}/D_{t0})$ , where  $SR_t$  is the normalized swelling ratio at time = t,  $W_t$  is the weight of the scaffold at time = t,  $W_{t0}$  is the initial weight of the scaffolds at t = 0,  $D_{t0}$  is

the dry weight of the scaffolds at  $t = 0$ , and  $D_t$  is the dry weight of the scaffold at time  $= t$ . Mass loss was determined by the following formula:  $M_t = (D_t/I_t)/(D_0/I_0)$ , where  $M_t$  represents the normalized mass of the scaffold at time  $= t$ ,  $I_t$  represents the initial dry weight of the scaffolds at time  $= t$ ,  $I_0$  represents the initial dry weight of the scaffolds at time  $= 0$ , and  $D_0$  and  $D_t$  and  $W_t$  represent the same as stated above. Results were normalized to the average initial wet weight and the individual scaffold dry weight (for swelling ratios) or the average initial dry weight and individual scaffold wet weight (for mass loss) at each timepoint.

*4.3.5 Mechanical tests:* Tensile tests were conducted on dog-bone-shaped polymer strips cut from photocured PGSA15 and PGSA35 sheets (test section dimensions roughly 10mm x 3.5mm x 1.2mm,  $n = 5$  per composition) and were tested using an Instron 5542 according to ASTM standard D412-98a. All mechanical testing was performed under wet conditions, specifically the photocured PGSA samples were incubated in PBS for 24 h prior to testing. The samples were elongated at a constant deflection rate of 10 mm/min and were all elongated to failure. Stress-strain properties were determined using engineering stress and strain and the tensile modulus was calculated from the initial slope (0-20%). The compressive modulus of the PGSA15, PGSA35, and swollen HA hydrogels (2%, 50kDa)<sup>192</sup> was determined using parallel plate grips on the same Instron 5542 at a constant deflection rate of 500  $\mu\text{m}/\text{min}$ . Samples for mechanical testing ( $n = 5$  per composition) were cylindrical (~1.5 mm height, ~6.0 mm diameter) and were compressed until failure or until 60% of the initial thickness was reached. None of the PGSA15 or PGSA35 samples failed before reaching the maximum loading limit of the 50N load cell

employed in all tests. The compressive modulus was determined as the initial slope of the stress-strain curve (0-20% strain).

*4.3.6 In vitro toxicity:* Cell proliferation was detected the XTT kit (Sigma, St. Louis MO) according to the manufacturer's instructions. Briefly, undifferentiated hESCs cultured in the presence of PGSA macromer with glycerol (15% and 35%) and were incubated for 4 h in medium containing 20% (v/v) XTT solution. For analysis, 150  $\mu$ l of the medium were removed, placed in a 96-plate well and read in a microplate reader at 450 nm.

Encapsulation of hESCs and neuroblastomas into PSGA. For encapsulation studies, cells were removed from culture by incubation with collagenase (hESCs) or with trypsin (neuroblastomas). Approximately  $3-6 \times 10^6$  hESCs or NBs were mixed with 50  $\mu$ L PGSA prepolymer (15% or 35% glycerol) and photocured as describe above. The crosslinked polymers were immediately placed in 2mls EB media (for hESCs) or NB media (for NB cells). Scaffolds with encapsulated cells were kept in culture for 1-7 days, and media was changed daily.

*4.3.7 Environmental Scanning Electron Microscope (ESEM):* FEI/Phillips XL-30 Field Emission ESEM was used to evaluate PGSA porosity, cell organization, and cell-material interaction. Samples of PGSA (with or without cells) were removed from culture, fixed with Accustain (Sigma-Aldrich, St. Louis, MO), and washed with PBS. Scaffolds were cut horizontally cut in half and placed with inner side facing up on the ESEM platform. ESEM images were taken with a beam intensity of between 5-30.0 keV at 0.4 Torr with the gaseous secondary electron (GSE) detectors.

*4.3.8 Porosity analysis:* Porosity of PGSA scaffolds was determined using ESEM images and histological sections of scaffolds using the built-in area selection tool of ImageJ software (NIH, Bethesda, MD). A total of 2 scaffolds and at least 10 images were analyzed from two different scaffold preparations. The size of each pore and total number of pores were determined for each image analyzed. The total percent porosity was determined the ratio of the total pore area to the total scaffold area in each image.

*4.3.9 In vivo biocompatibility:* PGSA, PGSA15, and PGSA35 scaffolds (all without cells) were prepared under sterile conditions and incubated in PBS for 48hrs. Female Lewis rats (n=8) (Charles River Laboratories, Wilmington, MA) weighing 200-250 g were housed in groups of 2 and had access to water and food ad libitum. Animals were cared for according to the approved protocols of the Committee on Animal Care of the Massachusetts Institute of Technology in conformity with the NIH guidelines for the care and use of laboratory animals (NIH publication #85-23, revised 1985). The animals were anaesthetized using continuous 2% isoflurane/O<sub>2</sub> inhalation. Two rats per group per time point received implants. This was done by three small midline incisions on the dorsum of the rat and the implants were introduced in lateral subcutaneous pockets created by blunt dissection. All animals remained in good general health throughout the study as assessed by their weight gain. At each predetermined time point (1,3,5, and 7 weeks), one randomly selected group of rats (n=2) was sacrificed, and the implanted scaffolds were removed en bloc with the surrounding tissue (~15x15mm). The samples were fixed and processed for histology as described below.

*4.3.10 Histology:* PGSA scaffolds from both *in vitro* (with and without cells) and *in vivo* (without cells) experiments were placed in Tissue-Tek OCT gel (Sakura Finetechnical Co, Tokyo, JPN), frozen on dry ice, and stored at -80°C till cryostat sectioning. Sequential sections (8-15  $\mu\text{m}$ ) were stained with hematoxylin and eosine (H&E). Separate scaffolds from *in vivo* experiments were fixed with Accustain (Sigma-Aldrich, St. Louis, MO) for 24hrs, dehydrated in graded ethanol (70 - 100%), embedded in paraffin, sectioned using a microtome (4 $\mu\text{m}$ ), and stained with H&E.

*4.3.11 Immunofluorescence:* Cryosections were thawed and fixed with acetone for 5min at room temperature. After blocking with 5% FBS, cells were stained with one of the following primary antibodies: anti-cytokeratin 18 (1:50; Chemicon, Temecula, CA), anti- $\alpha$ -feto protein (1:100; Dako Dako California Inc. Carpinteria, CA), and Brachyury (1:100; R&D systems, Minneapolis, MN). Cells were then rinsed three times with PBS (Invitrogen corporation, Carlsbad, CA) and incubated for 30 min with suitable FITC-conjugated (R&D systems, Minneapolis, MN) or Cy3-conjugated (Sigma, St Louis, MO) secondary antibodies. Secondary antibody alone served as controls. The immuno-labeled cells were examined using fluorescence microscopy (Zeiss, Germany).

*4.3.12 Inflammatory response and in-growth characterization:* The size of the inflammatory active zone of implanted scaffolds was measured in histological sections using the built-in calibration/length tool in AxioVision software (Zeiss, Oberkochen, Germany). A total of 30 measurements (over 10 histological slices) were taken for each

scaffold. Additionally, the number of in-growths was determined for each implanted scaffold by counting pores with positive H+E staining and grouped by their size, small (<50um) and large (>50um), at each timepoint. Results are presented as the average  $\pm$  SD for the (n=4).

*4.3.13 Statistics:* One-tailed student's t-tests with unequal variances were performed to determine statistical significance, where appropriate (Microsoft Excel, Redmond, WA). Parametric one-way and two-way ANOVA tests were also performed where appropriate (GraphPad Prism 4.02, GraphPad Software, San Diego, CA). Significance levels were set at: \* $p < 0.05$ , \*\* $p < 0.01$ , and \*\*\* $p < 0.001$ . All results shown are mean $\pm$ SD.



## 4.4.0 Results

### 4.4.1 Characterization of PGSA scaffold porosity

We hypothesized that glycerol could be used during the PGSA polymerization process to develop a porous scaffold. We reasoned that glycerol (utilized as a cryoprotectant additive) is expected to be minimally toxic to cells, and is viscous, thus minimizing material separation during polymerization. Glycerol was added in 15% (PGSA15) and 35% (PGSA35) mass ratios with pre-polymer containing photoinitiator, and polymerized using ultraviolet light under sterile conditions. Glycerol concentrations higher than 35% did not form scaffolds that were structurally stable (visual observations; data not shown). We used environmental scanning electron microscopy (ESEM) and light microscopy of cryosectioned scaffolds to characterize the ultrastructure. Scaffolds prepared from both 15% and 35% glycerol resulted in pore formation across the entire scaffold. Macropores ( $\geq 50\mu\text{m}$ ; Fig 1a-b) with interconnecting pores ( $20\text{-}50\mu\text{m}$ ; Fig 1) were observed in both scaffolds, whereas micropores ( $< 20\mu\text{m}$ ) were found in greater number in PGSA35 scaffolds (Fig 1). The average macropore size were similar for both scaffolds, whereas the total pore number was greater for PGSA35 scaffolds (Table 1;  $*p < 0.05$ ). The total porosity (determined from macropores) was slightly higher in PGSA15 scaffolds (Table 1;  $***p < 0.001$ ).

### 4.4.2 Swelling and mass loss properties

To evaluate PGSA/glycerol scaffolds as a system for *in vitro* cell culture, we studied their swelling and mass loss properties. PGSA/glycerol scaffolds were prepared

as before and incubated in PBS for 1-35 days at 37°C. Both PGSA15 and PGSA35 swelled within 24 hours to  $206 \pm 18.9\%$  and  $140 \pm 4.20\%$  of their respective initial weights (mean $\pm$ SD, Figure 2A). The swelling ratios in both scaffolds showed a biphasic hydration that peaked at 6 days, followed by decreasing swelling ratios in each scaffold (Figure 2A). These data are consistent with mass loss over 35 days that was observed for PGSA15 ( $18.1 \pm 1.5\%$ ) and PGSA35 ( $27.5 \pm 4.9\%$ ) scaffolds (Fig 2B), and with previous experiments that showed slow *in vitro* degradation rates of PGSA<sup>186</sup>.

#### 4.4.3 Mechanical property characterization

To examine the mechanical properties of porous PGSA, we conducted a series of tensile and compressive tests. Tensile test showed that stress-strain properties of both PGSA15 and PGSA35 retained similar elastic behaviour to those of PGSA<sup>186</sup> (Fig 2C). The ultimate strain for PGSA15 was similar to that of PGSA (Table 2), whereas the ultimate strain for PGSA35 was significantly greater than either PGSA or PGSA15 (Table 2; \*\* $p < 0.01$ ). The Young's modulus for PGSA15 was significantly greater than for the value for PGSA35 (Table 2; \* $p < 0.05$ ), while both were lower than that for PGSA (Table 2). The ultimate stresses of the PGSA15 and PGSA35 were similar; however, both values were less than the ultimate stress of PGSA (Table 2).

#### 4.4.4 Toxicity

Previous studies have demonstrated that polymerized PGS and PGSA are biocompatible and support the growth and proliferation of cells<sup>121, 122, 186</sup>. Because the photocuring process may lead to unpolymerized PGSA, we evaluated the effects of

unpolymerized PGSA and glycerol on the toxicity of cells. We used hESCs for these experiments because they are particularly susceptible to harmful culture conditions<sup>193</sup>. Human ESCs were cultured on a MEF feeder layer with 50  $\mu$ l/ml PGSA15 and PGSA35, concentrations simulating conditions in which none of the material polymerized. Human ESCs formed characteristic colonies of proliferating cells in all culture conditions (Fig 3). Comparison of the cell metabolism by an XTT assay showed that cell proliferation rates were slightly reduced by PGSA15 and PGSA35 but not significantly different than control conditions (Fig 3).

#### *4.4.5 N18-RE-105 cell encapsulation and culture (in vitro)*

We evaluated the ability of PGSA15 and PGSA35 scaffolds to encapsulate N18-RE-105 neuroblastoma (NB) cells. NB cells were encapsulated by photopolymerization in PGSA15 and PGSA35 scaffolds and grown in culture media for 1-7 days. After 1 day in culture, ESEM analysis revealed that NB cells adhered to the scaffold wall (mainly within macropores) and formed protrusions and apparent interconnections between each other (Figure 4A-C). After 7 days, NB cells produced fibrils which coated entire pores, suggesting that cells were producing components of the extracellular matrix on the PGSA material (Fig 4D). NB cells continued to grow while forming 3D aggregates and were found in both smaller interconnecting pores and macropores (Fig 4E-F). NB cells were supported similarly in both PGSA15 and PGSA35 scaffolds, and no qualitative or quantitative differences were observed between the scaffolds.

#### *4.4.6 Human embryonic stem cell encapsulation (in vitro)*

To test whether PGSA scaffolds would support the culture of human embryonic stem cell (hESCs), we encapsulated undifferentiated hESCs into scaffolds using an analogous protocol used for the NB cell experiments. After 1 day in both PGSA15 and PGSA35 scaffolds, hESCs were found to be organized in colonies primarily within the PGSA macropores (Figure 4G-I). After 7 days, were found in interconnecting pores (Fig 4J), while forming tissue-like sheets that covered the entire scaffold (Fig 4K). Thick histological sections revealed aggregates with various cell morphologies within the pores (Fig 4L). Similarly to the NB cultures, no differences could be quantified between cells grown in PGSA15 and PGSA35 scaffolds

#### *4.4.7 Human ESC proliferation and differentiation (in vitro)*

Histology sectioning showed that hESCs encapsulated in PGSA15 and PGSA35 scaffolds for 7 days are at a higher cell density than was observed after 1 day of culture, suggesting that PGSA supports cell proliferation (data not shown). To further investigate this, hESCs encapsulated into PGSA15 and PGSA35 scaffolds for 7 days were stained for the Ki67 protein, which is expressed in proliferating differentiated cells<sup>194</sup>. The majority of encapsulated hESCs were observed to express Ki67 after 7 days in culture (Fig 5A-C). We further found cells that were representative of all three germ layers in the encapsulated differentiated hESCs (Fig 5D-F), suggesting that structures similar to EBs were forming within the scaffold.

#### 4.4.8 Biocompatibility (*in vivo*)

To investigate the biocompatibility of porous scaffolds made from PGSA and glycerol, we prepared PGSA15 and PGSA35 scaffolds without cells and implanted them subcutaneously in rats for 1-7 weeks. The thickness of the inflammatory active zone was quantified in each scaffold at four time points. Notably, there was an acute inflammatory response in the PGSA35 scaffolds that was not present in the PGSA15 scaffolds, as determined by the thickness of the active zone and the presence of characteristic signs of inflammation throughout the muscle (Fig 6A). The elevated inflammatory response in the PGSA35 scaffold that was observed at week 1 was not observed at later time points (Fig 6B). The active zone showed a decreasing inflammatory response for both PGSA15 and PGSA35 scaffolds over a 7 week period, as was previously reported for PLGA and PGS implants (Fig 6C;). The PGSA15 inflammatory response at all time points was similar to that previously reported for PLGA and PGS<sup>121, 122</sup>, which are known to be highly biocompatible.

#### 4.4.9 Scaffold ingrowth (*in vivo*)

We examined whether an increase in porosity from glycerol in PGSA scaffolds would promote the formation of tissue ingrowth *in vivo*. We observed that 1 week after subcutaneous implantation, some ingrowth could be detected in both the PGSA15 and PGSA35 scaffolds (Fig 7A), and ingrowth increased over 7 weeks post implantation (Fig 7B). The ingrowth was absent in the non-porous PGSA scaffolds made without glycerol. The ingrowths in the PGSA15 and PGSA35 scaffolds were observed both at the boundary of the scaffold and the surrounding tissue and within the scaffold pores (Fig

7C). In contrast to the non-porous scaffolds (without glycerol), increasing glycerol mass percentage was associated with an increase in both small ingrowth (Fig 7D), and large ingrowth (Fig 7E), over time. These data suggest that porous PGSA promotes scaffold ingrowth and could be used to support growth for tissue engineering applications.

#### 4.5.0 Discussion

The modified elastomer, PGSA, polymerizes under physiological conditions and allows the encapsulation of proteins and cells. Glycerol was chosen as a cell carrier due to its: (1) common usage as a cell and tissue carrier for cryopreservation<sup>195</sup>, and (2) minimal reactivity with PGSA that may result in dispersed phase separation. Our results show that mixing glycerol (15% or 35% (w/w)) with PGSA resulted in porous scaffolds. Macropores ( $\geq 50\mu\text{m}$ ) with interconnecting pores (20-50 $\mu\text{m}$ ) were observed in both scaffolds, whereas micropores ( $< 20\mu\text{m}$ ) were found in greater number in PGSA35 scaffolds. The addition of porosity had a substantial effect on the mechanical properties of PGSA, which is to be expected as increased porosity causes a decrease of load bearing material per volume, however these changes in porosity did not cause a decrease in ultimate strain. A softer substrate and the ability to tune the mechanical properties within a given range could be advantageous as cell differentiation was shown to be affected by substrate stiffness<sup>196</sup>. The toxicity effects of unpolymerized PGSA/glycerol were found to be minimal and most likely were magnified because unpolymerized material would normally be removed during media changes. Overall, we reasoned that either the PGSA15 or the PGSA35 scaffolds could be used to encapsulate and support the growth of cells in 3D culture.

Our laboratory and others have used methylacrylated and acrylated pre-polymer in combination with photopolymerization to encapsulate cells in hydrogels and have shown minimal effects of the UV light on cell viability, p53 accumulation, and gene aberrations over long term culture<sup>116, 189</sup>. NB cells were chosen because, like PGS, PGSA has possible applications as a material that may promote nerve guidance<sup>197</sup>. NB cells encapsulated in PGSA proliferated and formed structures resembling neuronal like spheres after one week in culture. Furthermore, after one week of encapsulation, the surface of the PGSA was covered with ECM fibers suggesting that the NB cells created their own 3D microenvironments by secretion of ECM. To examine the usage of PGSA with hESCs, undifferentiated hESC colonies were encapsulated and cultured for one week. Human ESCs proliferated and formed aggregates that resembled embryoid body like structures within the pores, which contained representative cell types of all three germ layers. Altogether, these results suggest that porous PGSA elastic scaffolds offer a biocompatible scaffold with tuneable mechanical properties.

Examining the porous PGSA biocompatibility *in vivo* it was found that high levels of glycerol (35%) resulted in acute inflammatory reaction which was decreased to basal levels similar to PGSA15 and PGSA<sup>186</sup>. In growth into both PGSA15 and PGSA35 was observed already after 1 week, which increased with time of transplantation. These results suggest that porous PGSA promotes integration with the host circulation and tissue, and therefore may be utilized for tissue engineering applications.

#### **4.6.0 Conclusions**

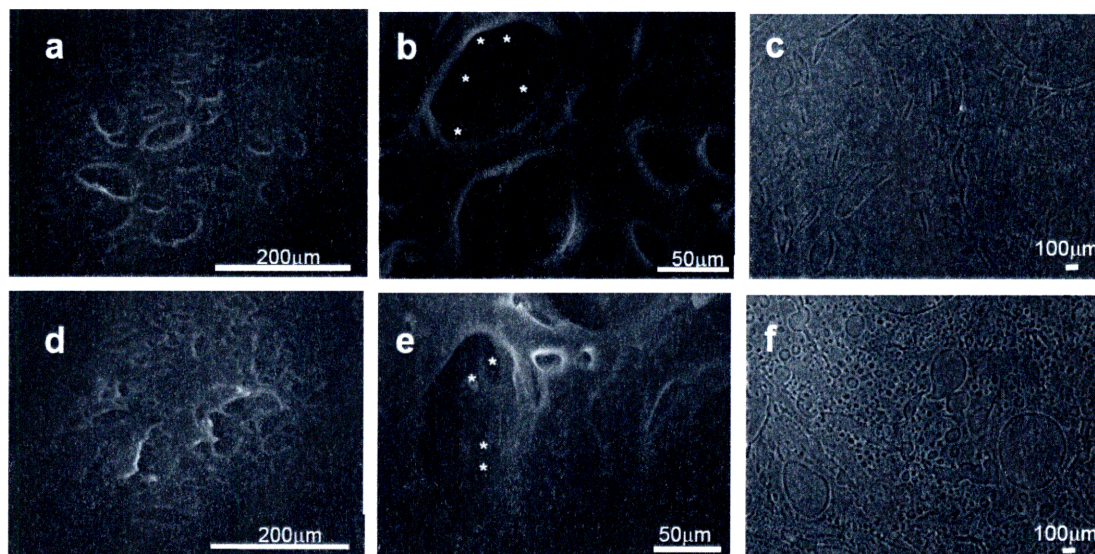
We have utilized glycerol to create porous PGSA scaffolds, which were found to maintain elastomeric mechanical properties, and defined porosity, swelling, mass loss, and biocompatibility characteristics. Porous PGSA scaffolds were used to encapsulate and support the growth of N18-RE-105 neuroblastoma and hESCs *in vitro*. Porous PGSA scaffolds were biocompatible *in vivo* and allow host tissue ingrowth. This data suggests that bioelastic porous PGSA scaffolds could be used as an alternative to hydrogel culture *in vitro* or as a scaffold for tissue engineering applications *in vivo*.

#### **4.7.0 Acknowledgements**

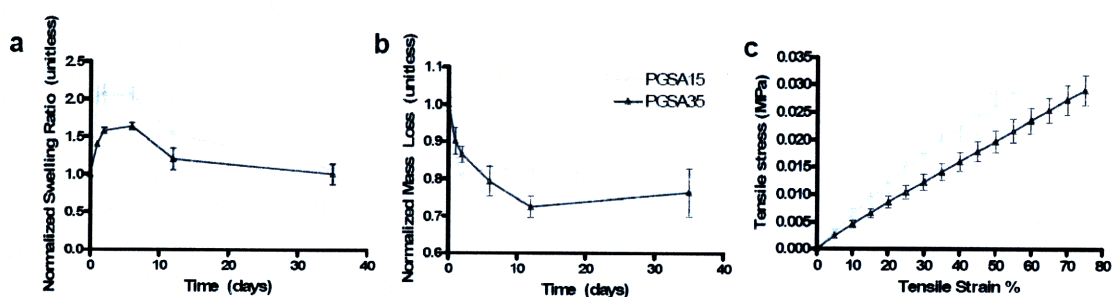
The authors would like to acknowledge the following: Weijia Zhang and the Center for Cancer Research Histology Core Facility at MIT for scaffold sectioning and H&E staining and the Center for Cancer Research Microscopy Imagine Core Facility at MIT for fluorescence microscopy imaging. Funding provided through NIH grants HL060434, HL076485, and RO1-DE13023, and an NSF graduate research fellowship for SAT.



## 4.8.0 Table and Figure Captions

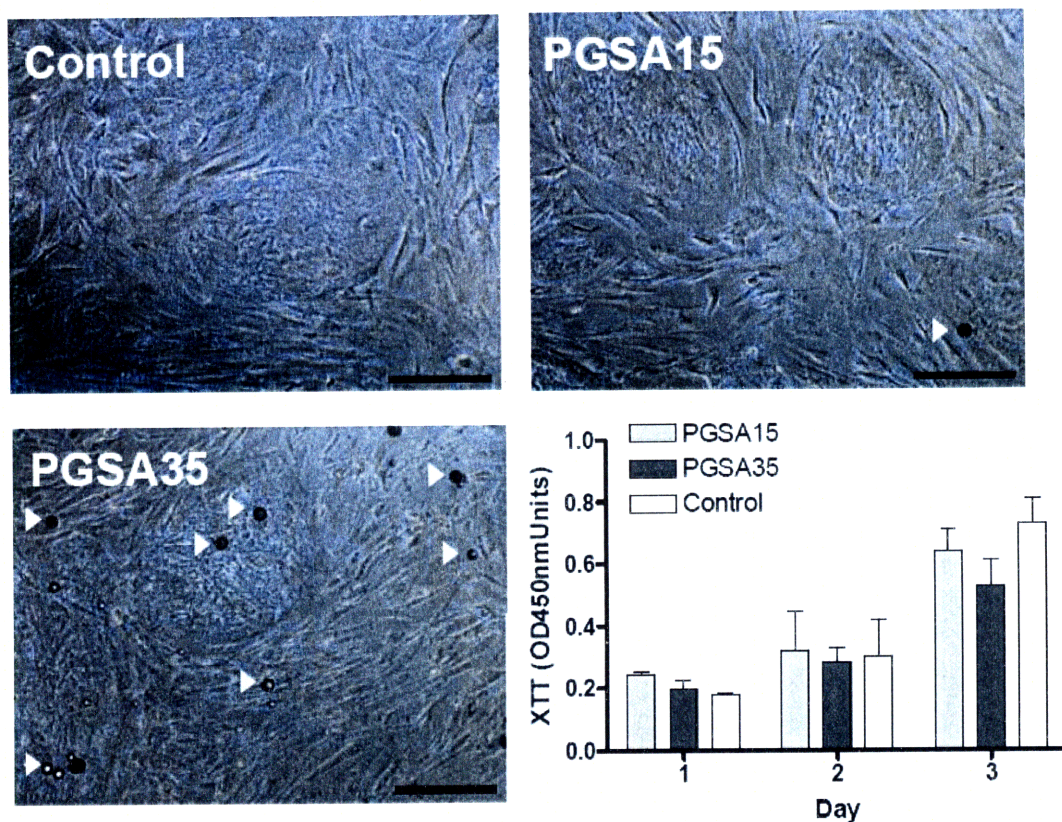


4.8.1 Figure 1: Porous PGSA. ESEM images of PGSA15 and PGSA35 scaffolds at low (left panels) and high (middle panels) magnification, showing the presence of macropores (>50 μm) and interconnecting pores (20-50 μm, asterisks). Light microscopy images of cryostat sectioned scaffolds (right panels) showing the presence of micropores (<20 μm) throughout the PGSA35 but not in the PGSA15 scaffolds.



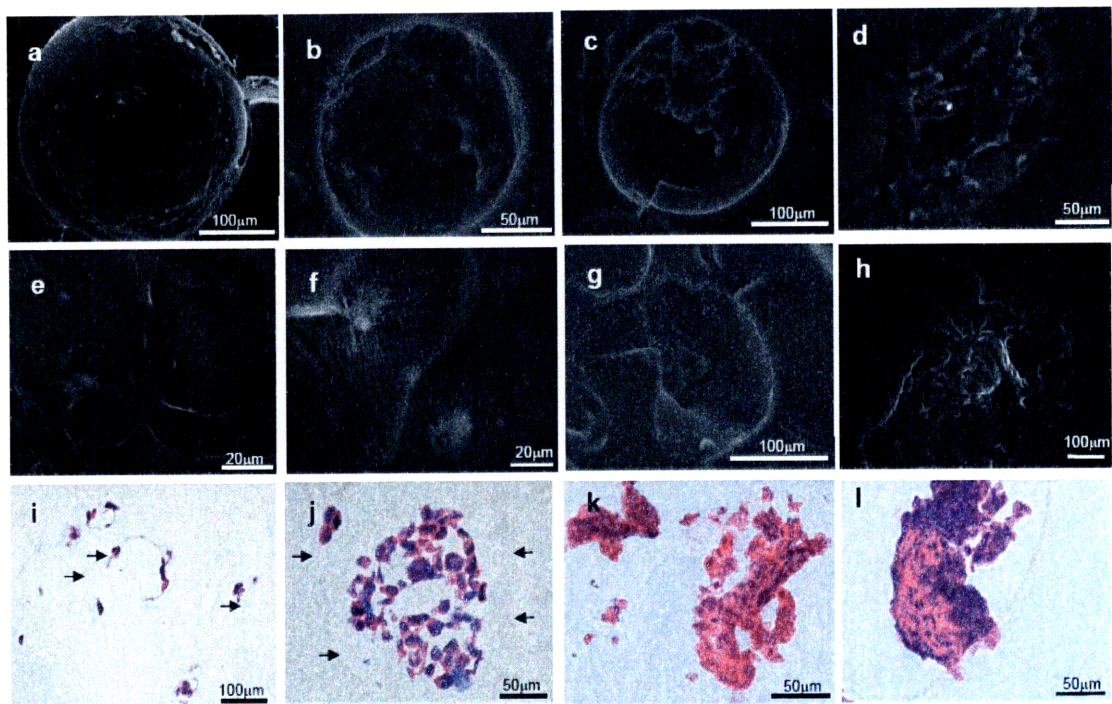
4.8.2 Figure 2: Swelling, mass loss, and mechanical characterization. (A) Normalized swelling ratios and (B) normalized mass loss during *in vitro* incubation for 1-35 days, and (C) Average tensile stress-strain properties of PGSA15 (light) and PGSA35 (dark) scaffolds.





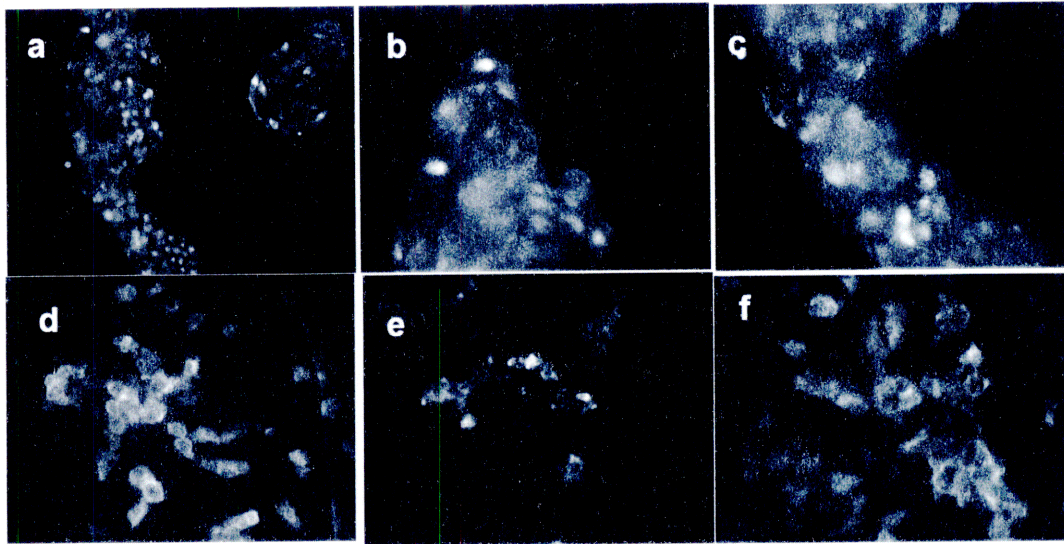
4.8.3 Figure 3: Toxicity of PGSA monomer and glycerol. Light microscopy images of undifferentiated hESCs grown on MEF feeder layers in the absence (control), or in the presence of 50uL/mL PGSA pre-polymer (PGSA15 and PGSA35). Characteristic hESC colonies are observed under all conditions. Arrows indicate PGSA and glycerol in media. Cell proliferation graph quantified by an XTT cell proliferation assay showing slightly reduced but not significantly different cell activity in PGSA15 and PGSA35 conditions, as compared to cells grown in control conditions. Scale bars=100 $\mu$ m.





4.8.4 Figure 4: Cell encapsulation within Porous PGSA. ESEM and H&E staining micrographs showing encapsulated N18-RE-105 NB cells (A) after 1 day of culture found primarily within macropores, (B) mainly located on the pore walls (indicated by arrows), while (C) forming cellular interconnections among neighboring cells. After 7 days, ESEM images showed that NB cells (D) produced fibrous components which coated entire pores, (E) formed 3D aggregates and (F) bonds among cells within the aggregates. Undifferentiated hESC colonies encapsulated in porous PGSA and cultured for 1 day were also observed to (G-I) settle within the macropores. After 7 days, hESCs (J,K) formed tissue like structures covering most of the scaffold pores, and (L) were organized in 3D structures containing cells with various morphologies.

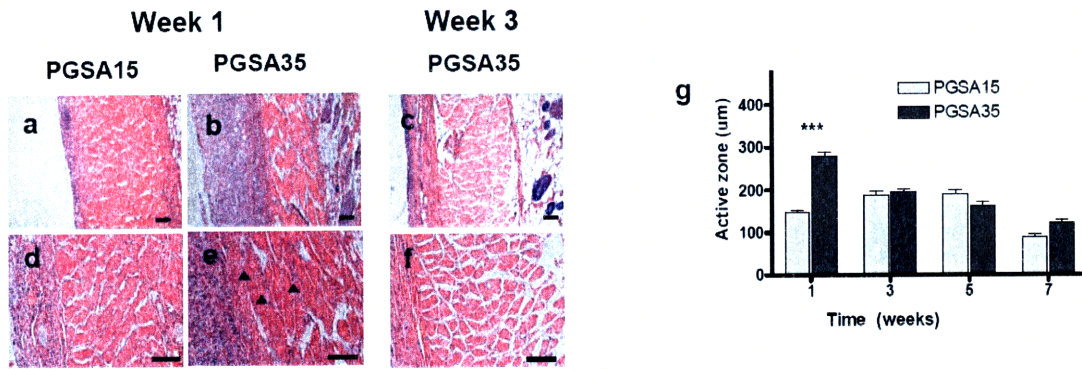




4.8.5 *Figure 5: Differentiated hESCs.* Immunofluorescent staining of hESCs encapsulated in porous PGSA and cultured for 7 days further revealed proliferating cells positive for Ki67 in (A) low and (B-C) high magnification. Differentiated hESCs were found to express early markers of the three germ layers: (D) brachury (mesoderm), (E) cytokeratin 18 (ectoderm), and (F)  $\alpha$ -Feto protein (endoderm). Scale bars A,D-F=50 $\mu$ m; B-C-10 $\mu$ m.

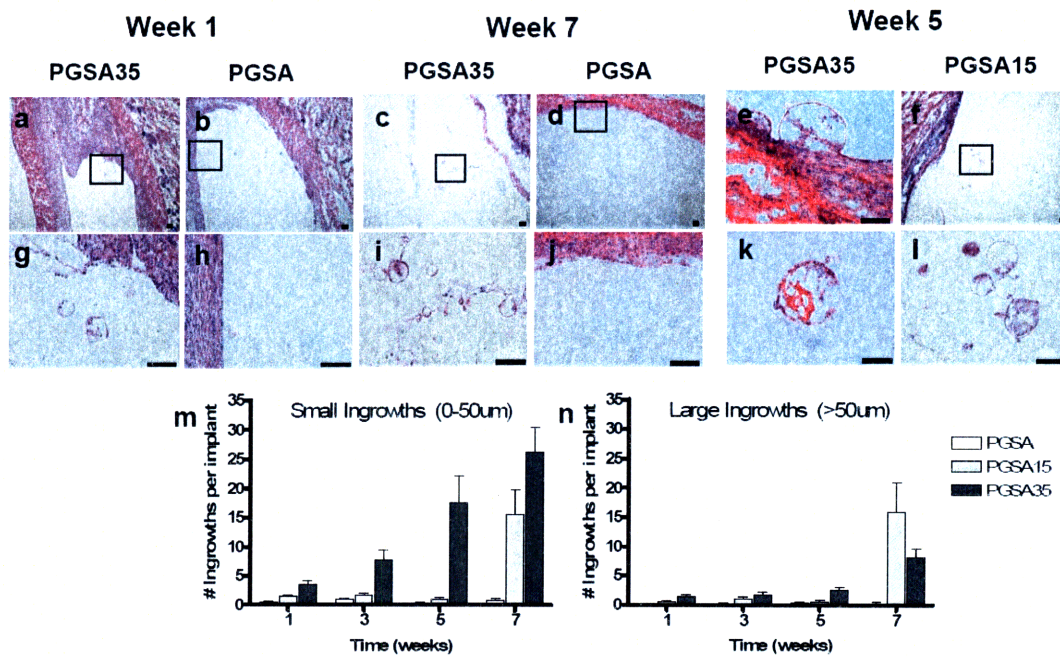






4.8.6 Figure 6: *In vivo* Biocompatibility. Porous PGSA scaffolds were transplanted S.C in rats. (A) After 1 week PGSA35 (i,ii) showed a thicker inflammatory zone surrounding the scaffolds than PGSA15 (iii,iv). Inflammation in the muscle (arrowheads) was found in PGSA35 scaffolds only. (B) After 3 weeks, the PGSA35 inflammatory zone was reduced to comparable levels for PGSA15. (C) Inflammatory zones of both scaffolds were reduced along the 7-week experiment ( $p < 0.001$ ). Scale bar=100 $\mu$ m.





4.8.7 Figure 7: *In vivo* ingrowth. PGSA, PGSA15, and PGSA35 scaffolds were transplanted subcutaneously in rats. (A) H&E stained histological slices of explants revealed tissue ingrowth in porous scaffolds after 1 week that were not observed in the nonporous scaffolds (no glycerol), and (B) continued to persist in porous scaffolds with almost no growth in the nonporous scaffolds (no glycerol). All boxes in upper panel are shown at higher magnification in lower panels. (C) Different types of ingrowth could be observed in implants including at the boundary of the scaffold and the surrounding tissue (right) and within the scaffold pores (left). Presence of glycerol was found to be associated with an increase in both (D) small and (E) large ingrowth. Scale bars=100 $\mu$ m.



**Table 1**

	Average Macropore Size (um)	Pore Number (# per mm <sup>2</sup> )	Porosity (% volume)
PGSA15	86.8±23.2	0.44±0.10*	18.1±2.10***
PGSA35	85.3±23.7	12.4±2.27	17.2±0.36

4.8.8 *Table 1: Pore Characterization.* Porosity properties of PGSA scaffold was quantified from ESEM images analyses. Porosity was determined for macropores (>50um) only by ESEM . Values shown are mean±SD.

**Table 2**

	Ultimate strain (%)	Young's modulus (kPa)	Ultimate stress (kPa)
PGSA15	57.0 ± 4.1%	59.9 ± 8.4*	27.8 ± 3.6
PGSA35	81.3 ± 13%**	42.3 ± 5.0	30.3 ± 2.6
PGSA <sup>186</sup>	60.1 ± 5.7%	568 ± 220	270 ± 32

4.8.9 *Table 2: Mechanical properties of porous PGSA.* Mechanical properties as determined from stress-strain relationships for PGSA15 and PGSA35 (n = 5 for each condition) and values for PGSA as determined previously for comparison<sup>186</sup>. Values shown are mean±SD.

**Table 3**

	Compression modulus (kPa)	Stress at ≤60% Strain (kPa)
PGSA15	119 ± 65*	266 ± 93
PGSA35	80.2 ± 28	232 ± 71
HA	34.1 ± 10.6*	144 ± 89 <sup>[a]</sup>

4.8.10 *Table 3: Compressive properties of porous PGSA.* Mechanical properties as determined from stress-strain relationships for PGSA15, PGSA35 and HA hydrogels (n = 5 for each condition).<sup>[a]</sup> Stress at failure. Values shown are mean±SD.



## Chapter 5: Future Directions

### 5.1.0 ALS biomarkers

We have shown that Gd-TTC can be used to quantify differences in axonal retrograde transport. It is clear that a functional measure of transport would help clinicians to both diagnose and to monitor the progression and any recovery of ALS; however, there is still much work that must be done before there is widespread use of a new biomarker for ALS. Specifically, we must characterize and optimize the dose and transport timecourse of the contrast agent. A thorough imaging study must be conducted that quantifies this rate, and to correlate differences that are observed with immunohistochemistry staining. Ideally, serial sectioning would be used in parallel with high resolution *in vivo* and *ex vivo* imaging to correlate differences observed and to determine the cluster of motor neurons for positive transport. These studies would provide insight into the mechanism of transport reduction that was observed in late stage ALS transgenic animals: a decrease in overall efficiency (i.e. rate) of transport, or a decrease in maximal transport rates.

New MRI imaging sequences could also improve quantification of transport rates by reducing noise. Gating on animal breathing could reduce motion artifacts, but would prolong the overall scan time. MRI coils that were specifically designed for spinal cord images would also enhance signal to noise over the standard surface coils that were used for these studies. Additionally, using iron in place of gadolinium as a contrast agent could enhance the overall signal, but would introduce additional complications that would need to be overcome and optimized in any subsequent study.

Any biomarker for ALS would need to be extensively validated in larger animal models for both efficacy and toxicity. These studies that were shown to be successful in mice would likely be conducted in rats, including ALS transgenic rat models, before moving into non-human primate models. Primate models would not include ALS animals, but would provide toxicity studies that would be required before moving into healthy humans and humans with ALS. However, our goal of developing a biomarker for ALS retrograde transport remains unchanged.

## **5.2.0 Drug delivery to the CNS**

Our goal of developing a drug delivery system that penetrates the CNS with high efficiency and selectively targeted neurons *in vivo* remains largely unrealized. This could be for a variety of reasons, including that nanoparticle size was too large, the use of TTC as a carrier molecule was ineffective, and that there was a technical reason for failure (i.e. radiolabeled molecules dissociated from the polymer nanoparticles). To address these issues, a series of experiments could be designed. Reducing nanoparticle size has proven difficult for a number of researchers, but progress is being made. Initial nanoparticle size is largely determined by solvent and non-solvent combinations, and the size of nanoparticles can easily reach 80nm or less. However, once protein is conjugated to the nanoparticle, aggregation becomes a problem. This problem can be alleviated but not eliminated by conducting the precipitation in PBS and maintaining this nanoparticle solution for the duration of the preparations. Additionally, sucrose stabilization can reduce aggregation during lyophilization and could be incorporated into future experiments.



It is possible that having higher concentrations of TTC, or utilizing other protein or viral fragments would improve cellular uptake and improve overall delivery to the CNS. Using avidin as a biotin binding molecule cross-linker or using a higher concentration of PLGA-PEG-biotin could increase protein concentrations. However, this would likely introduce additional problems with nanoparticle aggregation. If these approaches are not successful at improving uptake, TTC-conjugated nanoparticles could still have an application for local delivery. Thus, biodistribution studies should be conducted that test this option as a delivery vehicle. However, even with these additional experiments, it would be predicted that this drug vehicle would not be successful in penetrating the CNS because of the low penetration rates of the blood brain barrier.

### **5.3.0 Neuronal stem cells**

There are additional experiments that could be conducted to characterize the timecourse for differentiation and the non-neuronal cell fraction before any tissue engineering application would be realized. Our experiments have shown that PGSA was well tolerated both *in vitro* and *in vivo*, but that hESC that were encapsulated into PGSA differentiated into both neurons and non-neuronal fractions. In contrast, Matrigel encapsulation appeared to have a higher concentration of cells expressing neuronal markers than other cell germ layers. Thus more experiments are needed to characterize these differences in cell differentiation, and to quantify each cell fraction. The immunohistochemistry studies should be expanded to incorporate fluorescent analysis and dual staining, to determine specifically whether cells that have increased levels of

neuronal stains also have a decreased level of undifferentiation markers (Oct4, SSEA4, and Nanog).

The next phase of studies that could be conducted is to use encapsulated growth factors and cytokines that promote neuronal differentiation. Specifically, this could start by combining growth factors present in Matrigel with PGSA scaffolds, or to use microparticle controlled release for these studies. There are a variety of factors that could be considered, but it would be a logical first step to combine the two matrices that were utilized for this thesis. Additionally, it would be beneficial to know whether any long term genetic abnormalities were visible by conducting karyotyping experiments on long term culture of encapsulated cells. These studies would move us closer to understanding neuronal differentiation and to carefully controlling cell microenvironments for tissue engineering applications.

## Appendix Summary

### *Appendix A: Authorship on Publications and Manuscripts*

This contains a list of the publications and manuscripts that have led to the majority of this thesis, including authors lists, order, and affiliations. When noted, authors have contributed equally to manuscripts. Additionally, some of the work has been presented at scientific conferences, including a 1) Keystone Symposia: stem cells and their microenvironment (poster/presentation, March 2007) for the PGSA research, 2) US-Japan symposium on drug delivery systems (poster/presentation, December 2007) for the Gd-TTC biomarker and TTC-conjugated nanoparticles, and two separate departmental presentations given through the biotechnology and toxicology seminar series.

### *Appendix B: Tetanus toxin C conjugated nanoparticles for in vivo delivery to the central nervous system*

This appendix provides supplemental data from Chapter 3, dealing with further *in vivo* data supporting TTC-conjugated nanoparticle drug delivery to the CNS.

### *Appendix C: Human embryonic stem cell encapsulation in Matrigel for neuronal differentiation.*

This appendix details a new technique that we have utilized to encapsulate hESC into Matrigel scaffolds within a 3D microenvironment. We provide data that suggests that the Matrigel environment may induce neuronal differentiation and support stem cell culture.

### *Appendix D: Chemical structures and predicted NMR*

NMR results were compared with theoretical NMR signal, as determined by ChemDraw software, which is commonly used by chemists to convert a chemical structure into a signal. The following NMR spectra were analyzed: 1) PLA-PEG-biotin and PLGA-PEG-biotin, 2) NHS, EDC, and Sulfo-NHS, 3) Sulfo-NHS-biotin and NH<sub>2</sub>-PEG-biotin, 4) NH<sub>2</sub>-PEG-biotin theoretical NMR, 5) PLGA-COOH theoretical NMR, 6) PLGA-PEG-COOH theoretical NMR, 7) NH<sub>2</sub>-PEG-COOH theoretical NMR, 8) PLGA PEG-biotin theoretical NMR, 9) Biotin: theoretical NMR, and 10) Summary predicted polymer NMR. In summary, most of the peaks that were determined analytically were not similar to those that were predicted, even when the predictions had a large degree of certainty associated with the predictions.

#### *Appendix E: Synthesis of PLGA-PEG-biotin*

This contains a chemical equation overview of the process that was used to synthesize PLGA-PEG-biotin using NHS and EDC modifications of COOH acid groups at the terminal ends of the polymer.

#### *Appendix F: Schematics of MRI contrast agent biomarkers*

This contains a schematic of possible MRI contrast agents that could be used in parallel with TTC modifications as a biomarker for neurodegenerative diseases including ALS. These include: 1) Gd-TTC, which was the focus of our initial studies, 2) an iron core nanoparticle that is conjugated to TTC with a dextran outer shell and a ~2nm core, 3) a biodegradable PLGA (or equivalent) polymer nanoparticle with encapsulated Magnevist gadolinium-based MRI contrast agent, and conjugated to TTC. The first agent has the advantage of having a

size/molecular weight closest to that of TTC and is predicted to maintain the native retrograde transport properties of TTC. The second agent is iron-based and has extremely high contrast per nanoparticle. The third agent has the advantage of being biodegradable with a well-established safety profile. We have utilized all three systems in previous studies, with the best results coming from the first agent, and thus that is the primary work that we present.

*Appendix G: Additional analysis of MRI relaxivity*

Our first studies with the Gd-TTC contrast agent were conducted in a 96-well plate in a 1.5T MRI over a range of TE and TR signals. Thus, the relaxivity could be measured for each contrast agent, but not nearly as accurately as those results obtained from an NMR mini-spec. Gd-TTC, Gd-BSA, and iron core nanoparticles (conjugated to either TTC or BSA) were analyzed in the MRI at various dilutions. The results from these experiments agree well with those that are presented in the thesis.

*Appendix H: 4.7T MRI Imaging (in vivo)*

Initial MRI imaging experiments were conducted with live mice at 4.7T under isoflurane anesthesia. Mice were injected with 50 $\mu$ L of Gd-TTC (3mg/mL), for a total dose of 150 $\mu$ g of Gd-TTC, and imaged 24 hours post recovery. Shown are two sequential sections of the mouse spinal cord for the thoracic (left) and lumbar (right) regions. While there are regions of high MRI contrast intensity in the lumbar sections, further experiments suggested that these signals were caused by artifacts and not as a direct result of Gd-TTC transport.

*Appendix I: 9.4T MRI Imaging (in vivo)*

These contain images of mice that were injected with Gd-TTC and were presented earlier in the thesis. However, these images show the spinal cord with other organs that are visible, and additional sections. It is possible to see the full extent of the breathing and other artifacts that are visible throughout sections, and to see the orientation of tissue throughout the entire animal. It is clear that MRI contrast and the reduction of artifacts are not ideal, and that the imaging could be improved by a combination of imaging sequences and MRI coil design.

*Appendix J: Spinal cord staining of TTC transport (ex vivo)*

Immunohistochemistry of mice spinal cord samples in the lumbar region 24 hours after the injection of TTC protein. On the left are PBS negative controls, and on the right are TTC injected mice, for low (top) and high (bottom) magnification. These were stained with traditional DAB protocols. TTC localization is concentrated on a single side of the mouse; however, positivity is also visible on the contralateral side and around the edges of the tissue. Our desire to explore neuronal localization with dual staining in injected animals led us to pursue immunofluorescence for most experiments in this thesis.

*Appendix K: Additional analysis of IHC and MRI transport quantification*

There are many ways that the immunohistochemistry and MRI data can be analyzed and quantified to give comparisons between wildtype and ALS animals at various ages. This shows examples of the method that was used and described in detail during the thesis. Specifically, a histogram was generated for a region of interest in the ventral horn of the lumbar spinal cord on each side. The histogram corresponds to signal intensity levels, and the number of pixels in the image at

each intensity. Thus, a normalized ratio can be generated by fitting each histogram to a probability distribution function that accounts for differences in staining, antibody, and fluorescence background in each tissue sample. Shown are representative samples of wildtype and each age of ALS histograms.

#### *Appendix L: Nanoparticle preparations to control size*

One concern that we had when preparing nanoparticles for *in vivo* delivery of therapeutics is that the nanoparticle size would be too large to allow for TTC-facilitated transport. We tested a number of different polymer solvents and non-solvents to reduce nanoparticle size. Here we give a table of combinations for a PLGA polymer in each solvent, and the sizes of each nanoparticle preparation.

#### *Appendix M: Immunohistochemistry staining of TTC-conjugated nanoparticles*

We used traditional primary and secondary antibody immunofluorescent experiments to determine whether TTC was conjugated to nanoparticles, and whether this was specific when using NHS and EDC conjugation chemistry. This experiment also suggested that the TTC protein conformation was preserved. The figure shows greater fluorescence levels for TTC/NHS/EDC nanoparticles than those of negative controls. Negative controls include those without a primary antibody, secondary antibody, or without NHS/EDC.

#### *Appendix N: Nanoparticle protein encapsulation and conjugation*

We used a variety of methods to verify that proteins were encapsulated into biodegradable polymers for early experiments, and also to show that avidin could be used to specifically conjugate a protein to the polymer. (A) This shows that biotinylated fluorescent BSA was conjugated to the nanoparticles only with avidin

as a crosslinker, as evidenced by the visible fluorescent pellet of nanoparticles in ependorf tubes. (B) Flow cytometry confirmed that populations of nanoparticles were more fluorescent. (C-E) Fluorescent BSA protein was encapsulated into nanoparticles via a double emulsion protocol, and nanoparticles were analyzed by flow cytometry (C), and a BCA protein quantification assay (D-E). It was shown that protein could be encapsulated using these methods, but encapsulation efficiency of smaller molecule therapeutics was more quantitative via HPLC assays and was the focus of this analysis.

*Appendix O: Flow cytometry analysis of biotin binding proteins*

In addition to fluorescent quantification when comparing biotin binding proteins, we also used flow cytometry. Our analysis showed that this method could be used to show relative differences, but was less quantitative because it was greatly affected by nanoparticle concentration in each sample, suggesting that a population of nanoparticles was analyzed in each sample.

*Appendix P: Cell binding of TTC-conjugated nanoparticles using NHS/EDC*

Our initial experiments were focused on using NHS and EDC to conjugate TTC onto nanoparticles as a drug delivery vehicle. We made the nanoparticles fluorescent by encapsulating BSA-FITC via double emulsion, and then activated COOH groups on the polymer similarly to those protocols previously described<sup>169</sup>. An increase in N18-RE-105 neuroblastoma cell binding was observed in the TTC conjugated nanoparticles; however, the overall binding ratio compared to that of BSA conjugated nanoparticles was less than four fold. Thus, we



investigated methods of improving protein levels on the nanoparticles and focused on biotin binding proteins which gave higher overall binding ratios.

*Appendix Q: TTC nanoparticles binding to Prostate cancer*

Our studies investigating nanoparticle cell binding *in vitro* focused on several cell lines as negative controls that were not neuroblastomas and therefore were not predicted to express the TTC receptor, the GT<sub>1B</sub> ganglioside. However, we surprisingly observed that one prostate line (LNCAP) had significantly higher binding properties for TTC nanoparticles than for BSA negative controls. Upon further investigation, we found that previous publications showed that there were increased expression levels of the TTC binding ganglioside in LNCAP cells, relative to other cell types including PC3 prostate cell lines<sup>198</sup>. Thus, we suggest that TTC nanoparticles may be useful in targeting prostate cancer, as this ganglioside is also upregulated in human forms of prostate cancer.

*Appendix R: TTC binding to neuroblastomas with polystyrene nanoparticles*

In our earlier studies, we also used polystyrene nanoparticle beads to investigate differences in cellular uptake in cell lines as a function of nanoparticle size. There were significant increases in neuroblastoma binding after 30 minutes for 40nm and 200nm nanoparticles, and 1µm microparticles.

*Appendix S: Diffusion through hydrogels*

In our investigations of different scaffolds that could be utilized for cell encapsulation studies, we utilized hyaluronic acid and measured the rate of diffusion of some representative molecules of different sizes in the hydrogel (VEGF, albumin, globulins, and glucose). Scaffolds were prepared in a custom

molding, and then radiolabeled samples were taken from the supernatant, as indicated by the schematic. The amount removed was accounted for mathematically and was not predicted to change relative concentration levels significantly. All molecules had rapid diffusion rates through the hydrogel, and these studies could be expanded to other scaffolds.

#### *Appendix T: Cancer Stem Cells*

This provides further background about cancer stem cells, a field of growing interest with therapeutically relevant applications. Further insight into the biology behind cancer stem cells could provide additional applications for work in the field of ALS.

#### *Appendix U: References*

This includes a list of references that have been cited throughout the thesis, in the Nature journal format.

## Appendix A: Authorship on Publications and Manuscripts

### Chapter 2 (manuscript)

Development of a gadolinium tetanus toxin C fragment conjugate biomarker for *in vivo* MRI visualization of axonal retrograde transport in an amyotrophic lateral sclerosis mouse model

Seth A. Townsend<sup>a</sup>, Shuning Huang<sup>b,c</sup>, Ann Bialik<sup>d</sup>, Hannah Zhou<sup>e</sup>, Bruce Jenkins<sup>c</sup>, Bruce Rosen<sup>c</sup>, Robert S. Langer<sup>a,b,e</sup>, and Robert H. Brown, Jr.<sup>d,\*</sup>

<sup>a</sup> Departments of Biological Engineering, <sup>e</sup> Chemical Engineering, and <sup>b</sup> Division of Health Sciences and Technology, Massachusetts Institute of Technology, Cambridge, MA, 02139, USA. <sup>c</sup> Martinos Center for Biomedical Imaging, Massachusetts General Hospital, Charlestown, MA, 02129, USA. <sup>d</sup> Day Neuromuscular Research Laboratory, Massachusetts General Hospital East, 16<sup>th</sup> Street, Charlestown, MA, 02129, USA.

\*Address to whom correspondence should be addressed: email brownrhjr@aol.com.

### Chapter 3 (published<sup>85</sup>: *Biomaterials*. 2007 Dec;28(34):5176-84. Epub 2007 Sep 14.)

Tetanus toxin C fragment conjugated nanoparticles for targeted drug delivery to neurons

Seth A. Townsend<sup>a,1</sup>, Gilad D. Evrony<sup>b,1</sup>, Frank X. Gu<sup>c</sup>, Martin P. Schulz<sup>e</sup>, Robert H. Brown, Jr.<sup>f</sup>, and Robert S. Langer<sup>a,c,d,\*</sup>

<sup>a</sup> Departments of Biological Engineering, <sup>b</sup> Brain and Cognitive Sciences, and <sup>c</sup> Chemical Engineering, and <sup>d</sup> Division of Health Sciences and Technology, Massachusetts Institute of Technology, Cambridge, MA, 02139, USA. <sup>e</sup> Institute for Pharmacy and Molecular Biotechnology<sup>4</sup>, University of Heidelberg, Im Neuenheimer Feld 580, Heidelberg, 69120, Germany. <sup>f</sup> Day Neuromuscular Research Laboratory, Massachusetts General Hospital East, 16<sup>th</sup> Street, Charlestown, MA, 02129, USA. Department of Plastic and Reconstructive Surgery, Erasmus Medical Center, 3000 CA Rotterdam, The Netherlands.

<sup>1</sup> Authors contributed equally to this work. \*Address to whom correspondence should be addressed: email rlanger@mit.edu, fax (617) 258-8827

### Chapter 4 (published<sup>172</sup>: *Biomaterials*. 2007 Nov;28(32):4826-35. Epub 2007 Aug 9.)

A porous photocurable elastomer for cell encapsulation and culture

Sharon Gerecht<sup>a,c</sup>, Seth A. Townsend<sup>b</sup>, Heather Pressler<sup>c</sup>, Han Zhu<sup>b</sup>, Christiaan L.E. Nijst<sup>f</sup>, Joost P. Bruggeman<sup>g</sup>, Jason W. Nichol<sup>a,d</sup>, Robert Langer<sup>a,b,d,\*</sup>

<sup>a</sup> Division of Health Sciences and Technology, and Departments of, <sup>b</sup> Biological Engineering, <sup>c</sup> Chemistry, and <sup>d</sup> Chemical Engineering, Massachusetts Institute of Technology, 77 Massachusetts Avenue, Cambridge, MA, 02139, USA. <sup>e</sup> Department of Chemical and Biomolecular Engineering, Johns Hopkins University, 3400 North Charles Street, Baltimore, MD 21218, USA. <sup>f</sup> Department of Biomedical Engineering, Eindhoven University of Technology, 5600 MB Eindhoven, The Netherlands. <sup>g</sup> Department of Plastic and Reconstructive Surgery, Erasmus Medical Center, 3000 CA Rotterdam, The Netherlands. \* Address to whom correspondence should be addressed: email [rlanger@mit.edu](mailto:rlanger@mit.edu), fax (617) 258-8827

### Appendix B (manuscript)

Tetanus toxin C conjugated nanoparticles for *in vivo* delivery to the central nervous system

Seth A. Townsend<sup>a</sup>, Gilad Evrony<sup>b</sup>, Ann Bialik<sup>c</sup>, Frank Gu<sup>d</sup>, Hannah Zhou<sup>d</sup>, Robert H. Brown, Jr.<sup>c</sup>, Robert Langer<sup>a, d, e, \*</sup>

<sup>a</sup> Departments of Biological Engineering, <sup>b</sup> Brain and Cognitive Sciences, <sup>d</sup> Chemical Engineering, and <sup>e</sup> Division of Health Sciences and Technology, Massachusetts Institute of Technology, Cambridge, MA, 02139, USA. <sup>c</sup> Day Neuromuscular Research Laboratory, Massachusetts General Hospital East, 16<sup>th</sup> Street, Charlestown, MA, 02129, USA. \* Address to whom correspondence should be addressed: email [rlanger@mit.edu](mailto:rlanger@mit.edu).

### Appendix C (manuscript)

Human embryonic stem cell encapsulation in Matrigel for neuronal differentiation.

Seth A. Townsend<sup>a, #</sup>, Martin Schulz<sup>b, #</sup>, Sharon Gerecht<sup>c, d</sup>, and Robert Langer<sup>a, c, e, \*</sup>

Departments of <sup>a</sup> Biological Engineering and <sup>c</sup> Chemical Engineering, and <sup>e</sup> Division of Health Sciences and Technology, at the Massachusetts Institute of Technology, 77 Massachusetts Avenue, Cambridge, MA, 02139, USA. <sup>e</sup> Institute for Pharmacy and Molecular Biotechnology<sup>4</sup>, University of Heidelberg, Im Neuenheimer Feld 580, Heidelberg, 69120, Germany. <sup>d</sup> Department of Chemical and Biomolecular Engineering, Johns Hopkins University, 3400 North Charles Street, Baltimore, MD 21218, USA. <sup>#</sup> authors contributed equally. \* Address to whom correspondence should be addressed: email [rlanger@mit.edu](mailto:rlanger@mit.edu), fax (617) 258-8827

## **Appendix B: Tetanus toxin C conjugated nanoparticles for *in vivo* delivery to the central nervous system**

### **A.B.1.0 Abstract**

Amyotrophic lateral sclerosis (ALS, or Lou Gehrig's disease) is a neurodegenerative disease of the central nervous system (CNS). We have expanded on our previous studies utilizing TTC-conjugated PLGA-PEG nanoparticles to evaluate whether they would lead to more effective therapeutic drug delivery systems targeting the CNS. Riluzole, the only FDA-approved drug for ALS, was encapsulated within nanoparticles and showed to exhibit a controlled release profile over a period of several days. TTC-conjugated nanoparticles were shown to be biocompatible using H&E staining, and specifically transported *in vivo* from the injection site in the peripheral quadriceps into the lumbar region of the spinal cord. Furthermore, TTC-conjugated nanoparticles were co-localized within lumbar spinal cord motor neurons. Radiolabeled biodistribution studies showed that there was not a statistically significant difference between TTC-conjugated and BSA-conjugated nanoparticles in their ability to reach the central nervous system. TTC-conjugated nanoparticles could provide a drug delivery system that enables selective targeting of motor neurons of the central nervous system.

## **A.B.2.0 Introduction**

Delivering therapeutic agents to the central nervous system (CNS) is of great importance but has remained challenging in part because of difficulties in penetrating the blood brain barrier (BBB), a layer of endothelial cells bound by tight junctions. Most drugs that are larger than ~400 daltons do not pass through the BBB with high efficiency<sup>74</sup>. Various approaches have been used to administer agents to the CNS including concentrated mannitol, vascular endothelial growth factor (VEGF), ultrasound, encapsulation within nanoparticles, and retrograde transport. Of these, mannitol remains the most widely used clinically, primarily for applications in cancer treatment. Ultrasound and VEGF administration remain an active field of ongoing research. In addition, nanoparticle (both non-targeted and targeted) and retrograde transport approaches have been used successfully to penetrate the BBB.

Many nanoparticles are synthesized from commonly used polymers, including polylactic acid (PLA), poly(lactic-co-glycolic acid) (PLGA), and polyglycolic acid (PLG), which are used to encapsulate and release a therapeutic agent usually over a period of days to months, with minimal toxicity<sup>69</sup>. New polymers are being evaluated for use as drug carriers that may have beneficial properties such as improvements in drug loading efficiency, payload delivery, or release kinetics, but their toxicity profile must be extensively validated before widespread clinical use. Generally, these properties are different for each therapeutic compound and polymer but can be optimized for each application.

Nanoparticles can be administered either through non-targeted or targeted delivery. During the latter, a protein, aptamer, peptide sequence, or other targeting

molecule specific for a receptor is attached to the outside of the polymer nanoparticle. Targeted nanoparticles offer the potential for local delivery, reducing any systemic side effects of the encapsulated therapeutic, and may reduce systemic clearance rates (i.e. from the kidney, liver, or macrophages) <sup>75</sup>. This is important as common routes of nanoparticle administration include intravenous and intramuscular delivery, both of which may lead to rapid clearance and reduced efficacy with certain applications. Many studies have found that the incorporation of polyethylene glycol (PEG) to the polymer chain reduces clearance rates and may improve overall efficacy <sup>76</sup>.

Most nanoparticles are not efficient at penetrating the CNS because of a combination of their size, surface charge, and hydrophobic properties <sup>74</sup>. However, their smaller size (in comparison with larger microparticles) may allow for greater BBB penetration. Recently, non-targeted polymer nanoparticles prepared from polybutylcyanoacrylate (PCBA) polymer encapsulating a variety of drugs and coated with a polysorbate 80 surfactant have been shown to penetrate the BBB <sup>77-81</sup>. The mechanism for uptake is not fully understood, but is proposed to take place via receptor mediated endocytosis in brain endothelial cells (ref) <sup>82</sup>. However, in contrast to PLA, PLG, and PLGA polymers that are currently used in FDA-approved applications, PCBA polymers would need to be studied more extensively before they are widely used clinically <sup>83</sup>.

Targeted nanoparticles may allow for boundaries such as the BBB to be penetrated by facilitating endocytosis or transcytosis across brain endothelial cells. Another approach utilizes retrograde transport to bypass the BBB. Axonal retrograde transport is an important cellular process used by neurons to transport proteins, small

molecules, and even cell organelles from the terminal end of a neuron towards the cell body. It is utilized by viruses (i.e. herpes) and bacterial toxins (i.e. tetanus toxoid) to bypass the BBB and efficiently penetrate the CNS. Researchers have used retrograde transport to deliver genes and protein conjugates to the CNS with therapeutic efficacy<sup>36, 84</sup>. In addition, this approach offers the possibility of selectively targeting a specific region of the CNS that is a function of the injection site. This is in contrast to non-targeted intravenous administration that would likely penetrate the entire CNS equally. However, one concern with using this approach is a possible immune response, which may be particularly important in patients diagnosed with cancer or those taking immunosuppressive medications. The immune response will likely be a function of the retrograde transport molecule used and previous immunizations to that molecule. Recently, the tetanus toxin C fragment (the non-toxic binding portion of the tetanus toxoid that is efficiently retrograde transported in neurons) was conjugated to nanoparticles and shown to target neuroblastoma cells *in vitro*<sup>85</sup>. It is not clear yet whether this approach will lead to nanoparticles penetrating the CNS with high efficiency *in vivo*.

Liposome nanoparticles prepared from lipids offer another alternative to deliver therapeutics to the CNS. In particular, lipids may offer better loading efficiency for negatively charged DNA or siRNA payloads than negatively charged polymers. Liposomes that were conjugated to a transferrin or insulin receptor antibody (thought to transcytosis across endothelial cells) were have been used for successful gene delivery with a brain specific promoter (ref)<sup>153, 199, 200</sup>. However, this approach is non-specific to brain endothelial cells and requires a brain specific promoter to achieve selective CNS



targeting. A different study addressed this issue by targeting magnetic liposomes to the vasculature surrounding the CNS by generating a transient magnetic field<sup>201</sup>. This approach may be used in parallel with a targeted liposome to penetrate the CNS while reducing nonspecific uptake in other organs. In addition to these approaches, lipid libraries similar to those that have been used for other organs could lead to new materials that might efficiently penetrate the BBB and target CNS<sup>202</sup>. In particular, these liposomes may have applications for delivering interference RNA through shRNA, siRNA, or RNAi molecules because their loading efficiency is generally higher than that of negatively charged polymer nanoparticles.

The overall goal of this study is to advance our previous research that showed TTC-conjugated nanoparticles were highly selective for neuroblastoma cells *in vitro*<sup>85</sup>, and to evaluate whether these nanoparticles could be used as a drug delivery system to selectively target the central nervous system *in vivo*.

### **A.B.3.0 Methods**

*A.B.3.1: Preparation of nanoparticles:* PLGA-PEG-biotin polymer and nanoparticles were prepared as previously described<sup>85</sup>. Briefly, PLGA-COOH (20kDa MW, Lactel Absorbable Polymers) was activated with NHS (1:8 PLGA:NHS molar ratio) and EDC (1:8 PLGA:EDC molar ratio) and subsequently incubated with NH<sub>2</sub>-PEG-Biotin (3400MW, Laysan Bio) (1:1.3 PLGA:PEG molar ratio) to form PLGA-PEG-biotin. Nanoparticles were prepared by PLGA-PEG-biotin (6.7mg/mL polymer in acetone) nanoprecipitation into deionized water. Coumarin-6 (1mg/mL in acetone, Sigma Aldrich) or drug (riluzole or thalidomide, 5-50% mass drug:polymer) were mixed with the polymer prior for encapsulation studies. The solvents for the drugs and polymer that were used included: acetone, acetonitrile, or DMSO, and were acetonitrile where not indicated. Nanoparticles (500uL at ~20mg polymer/mL) were incubated with neutravidin (2uL at 2mg/mL) (Pierce Biotechnology; Rockford, IL), subsequently mixed with biotinylated TTC or BSA, and washed by centrifugation using an Amicon filter (4,000ref, 25C, ~20 minutes). Nanoparticles were concentrated and stored at 4C until use.

*A.B.3.2 Measurement of encapsulation efficiency and release kinetics:* Drugs were encapsulated into polymer nanoparticles (as indicated above) and dialyzed against a 10,000 Da membrane (Pierce Biotechnology; Rockford, IL) at timepoints between 0-48 hours. Once removed, nanoparticles were snap frozen in liquid nitrogen and lyophilized to remove liquid. The dry nanoparticles were dissolved in acetonitrile solvent, filtered through a 0.22µm syringe filter and analyzed using an Agilent 1100 high performance

liquid chromatography (HPLC) (Agilent Technologies; Palo Alto, CA) with a C18 column (Alltech Associates; Deerfield, IL) in 100 $\mu$ L intervals with detection at 264 $\lambda$  as previously described<sup>158, 203</sup>. All samples were processed with equal parts of water and acetonitrile at constant 1ml/min flowrate for one hour. Various timepoints were taken to generate release kinetics curves for each drug at different loading concentrations, and total encapsulation efficiency was determined by known drug concentrations at initial timepoints by normalizing to polymer peaks in the HPLC.

*A.B.3.3 Animal study approval and injections:* All animal protocols were approved by the Committee on Animal Care at the Massachusetts Institute of Technology. Mice (8-16 weeks) were anesthetized with 130mg/kg ketamine and 10mg/kg xylazine via an intraperitoneal injection. Mice were shaved and a small incision was made exposing the right quadriceps under aseptic conditions. Three 25 $\mu$ L injections containing BSA-conjugated, TTC-conjugated nanoparticles or a PBS negative control were made into the muscle using a 26G Hamilton syringe (1.5mg total protein injected). Nanoparticles were injected that contained coumarin-6, radiolabeled [3H]-PLGA (5 uCi per animal), or blank drug, and were either conjugated to TTC or BSA. The wound was sutured and the animal was allowed to recover.

*A.B.3.4 Transcardial perfusion and spinal cord isolation:* Animals for all spinal cord sectioned experiments (H&E, fluorescent nanoparticles, and immunohistochemistry staining) were sacrificed using CO<sub>2</sub> asphyxia. An incision was made opening the animal's sternum, and a 30G needle was inserted into the left ventricle. The right atrium

was cut, and the animal was perfused with PBS until blood cleared. Perfusion medium was switched to 4% paraformaldehyde solution and perfused for 15 minutes. The spinal cord was gently removed from the vertebrate using forceps and blunt dissection, and cut into cervical, thoracic, and lumbar sections. Tissue was fixated in 4% paraformaldehyde overnight. For immunohistochemistry experiments, tissue was incubated in 10% sucrose for 12 hours, and then in 30% sucrose solution for 12 hours, each overnight at 4C until sectioning. Tissue for hematoxylin and eosin staining was stored in PBS until mounting.

*A.B.3.5 Hematoxylin and Eosin staining:* Spinal cords from mice injected with TTC-conjugated nanoparticles, BSA-conjugated nanoparticles, or PBS negative controls were prepared as described previously <sup>204</sup>. A Gemini automated (ThermoFisher Scientific; Waltham, MA) staining machine was used for all H&E. Briefly, tissue was dehydrated in graded ethanol (70 to 100%), embedded in paraffin and sectioned axially using a microtome (4 $\mu$ m). Tissue paraffin was removed with 3 changes of xylene, rehydrated with graded ethanol, stained with Harris Hematoxylin (Surgipath Medical; Richmond, IL) for four minutes, and then rinsed with water, 1% acid alcohol (1% HCl in 70% ethanol), and then water in series. Tissue was then stained for blue nuclei using Scott's Tap water substitute (Surgipath Medical; Richmond, IL) for one minute, washed and ethanol/xylene dehydrated as previously, and mounted. Slides were photographed using an inverted Nikon light microscope.

*A.B.3.6 Immunohistochemistry staining for TTC and NeuN:* Mice injected with either TTC-conjugated or BSA-conjugated nanoparticles were sacrificed 24-48 hours post

injection. Nanoparticles were fluorescent for all non-stained tissue, and non-fluorescent for all immunohistochemistry stained tissue. Samples were placed in Tissue-Tek OCT gel (Sakura Finetechnical Co; Tokyo, Japan), frozen on dry ice, and stored at -80°C till cryostat sectioning. For all non-fluorescent samples, tissue was blocked and permeabilized in using PBS containing 0.3% Triton-100 and 10% FBS for 1h at RT. Tissue was incubated with rabbit anti-TTC (1:1000, Rockland Immunochemicals; Gilbertsville, PA) and mouse anti-NeuN (1:500, Chemicon; Billerica, MA) containing 0.1% Triton-100 and 10% FBS overnight at 4C. Tissue was washed in PBS 3x to remove unbound primary antibodies. Tissue was incubated with Cy3 conjugated goat anti-rabbit (1:1000, Jackson ImmunoResearch; West Grove, PA) and FITC conjugated goat anti-mouse (1:100, Sigma; St. Louis, MO) containing 0.1% Triton-100 and 10% FBS for 1.5 hours at RT. Tissue was washed 3x in PBS to remove unbound secondary antibody. For all samples, tissue was mounted using Vectashield fluorescent mounting medium containing DAPI (Vector Laboratories; Burlingame, CA) and imaged using a Nikon E800 microscope.

*A.B.3.7 Cell culture and nanoparticle incubations:* N18-RE-105 neuroblastoma and HepG2 liver cells were grown with previous methods as those previously described<sup>85, 160-162</sup>. Briefly, neuroblastoma cells were cultured in DMEM and supplemented with HAT supplement (100uM sodium hypoxanthine, 400nM aminopterin, 16uM thymidine), 10% FBS, and 1% penicillin/streptomycin. HepG2 cells were grown in MEM containing 10% FBS and 1% penicillin/streptomycin. All cells were grown in filtered flasks in an incubator at 95% air and 5% carbon dioxide. Media was changed every 48 hours, and

cells were passaged with EDTA-trypsin when confluent. Confluent neuroblastoma and HepG2 cells were incubated with dilute radiolabeled nanoparticles at 37C for 30 minutes prior to trypsin and processing for radiodetection. All media reagents were purchased from Invitrogen. HepG2 cells were purchased from ATCC, and N18-RE-105 cells were a generous gift of Dr. Jonathan Francis at the Massachusetts General Hospital.

*A.B.3.8 Nanoparticle biodistribution (in vivo) and tissue preparation/processing:* Radiolabeled nanoparticles (TTC or BSA conjugated) were prepared and injected unilaterally into the mouse quadriceps as stated above. Separate animals were injected with PBS negative controls. Mice were sacrificed 48 hours post injection, and the following organs were harvested and weighed: heart, spleen, lung, liver, kidney, right (injected) quadriceps, left (not injected) quadriceps, brain, spinal cord, bone, and blood. The tritium content of each tissue sample was analyzed using a Packard Tri-Carb Scintillation Analyser (Downers Grove, IL, USA) as protocols modified from those previously described<sup>158</sup>. The tissues were measured in liquid solution with equal parts of Hionic-Fluor scintillation cocktail (PerkinElmer, Boston, MA). Tissue was processed prior to measuring in 2mL of Solvable (Packard) for 12h at 60C, and the resulting solution was de-colored with 200 mL hydrogen peroxide for 1h at 60C. The injected stock solution was also measured and treated as an unknown sample to determine the percentage of injected dose at each tissue. The wet weight of each organ was measured to normalize radioactive counts to each gram of tissue. All sample analysis was conducted immediately after the removal of tissue.

## **A.B.4.0 Results and Discussion**

### *A.B.4.1 Riluzole release kinetics from nanoparticles*

We studied the release kinetics of riluzole after encapsulation into biodegradable polymers of different molecular weights at various loading efficiencies. Riluzole was chosen as a model drug because it is currently the only FDA approved drug for amyotrophic lateral sclerosis (ALS, or Lou Gehrig's disease), a disease that would benefit from drug controlled release and local delivery from nanoparticles. We utilized nanoparticles prepared from PLGA-PEG polymer as previously described<sup>85</sup>, with inherent viscosities of either 0.67 or 0.83 (in methylene chloride). Polymer solvents that were used included acetone, acetonitrile, and dimethyl sulfoxide (DMSO). At 50% drug loading, a burst release for all solvent and polymer viscosity conditions was observed (Figure 1a), which is consistent with other release profiles for small molecule drugs<sup>203</sup>. We then reduced the drug loading percentage to a 5% drug to polymer mass ratio. This resulted in drug release profiles that were extended, with only 90% of the drug released after 48 hours (Figure 1b). This is a significant improvement on current riluzole treatments which are administered twice daily, and could likely be further optimized to extend the release profile.

### *A.B.4.2 Biocompatibility of TTC-conjugated nanoparticles*

Spinal cords from mice that were unilaterally injected with TTC or BSA conjugated nanoparticles were fixed, sectioned, and stained with hematoxylin and

ession to determine whether any signs of acute inflammation were observed. No differences were observed between injected animals (either TTC or BSA conjugated nanoparticles) (Figure 2) and PBS negative controls (data not shown). These results suggest that an injection of the Gd-TTC conjugate is well tolerated and biocompatible. This is consistent with previous observations following the injection of TTC in rodents and the established safety profile of gadolinium compounds used in the clinic.

#### *A.B.4.3 In vivo transport of TTC-conjugated nanoparticles*

To evaluate whether nanoparticles were transported to the lumbar spinal cord specifically (i.e. as a direct result of TTC conjugation), we prepared fluorescent nanoparticles and conjugated them to either BSA or TTC. Nanoparticles were injected unilaterally as before, and spinal cords were sectioned using a cryostat. Sections were immediately mounted and stained with DAPI mounting medium to photograph sections using a fluorescent microscope. All animals showed a small amount of non-specific uptake on the uninjected side of the animal, likely a result of nanoparticles that were in circulation. However, the intensity of fluorescence was significantly higher on the side of injection, and was co-localized with DAPI stains (Figure 3), as indicated by three different animals for representative traces. Spinal cords from mice that were injected with BSA-conjugated nanoparticles were less intense than those from TTC-conjugated mice (data not shown). These data suggest that TTC-nanoparticles promote delivery to the spinal cord.

#### *A.B.4.4 Localization of TTC-conjugated nanoparticles in motorneurons*



Spinal cords from mice that were unilaterally injected with TTC or BSA conjugated nanoparticles (non-fluorescent) were fixed, sectioned, and immunostained against TTC and a NeuN neuronal stain to verify axonal retrograde transport and to further explore neuronal localization within the spinal cord. Spinal cord sections from mice following TTC-conjugated nanoparticle injection showed unilateral positive staining for TTC concentrated in the ventral horn of the lumbar region of the spinal cord (Figure 3, top). This was absent in spinal cord sections that were injected with BSA-conjugated nanoparticles (Figure 3, bottom). Furthermore, TTC positive staining was co-localized with neuronal positive staining in the positive samples. Spinal cord sections from TTC injected mice showed similar localization, intensity, and distribution (data not shown). PBS injected mice showed characteristic NeuN staining, but only background levels of TTC staining (data not shown). These results suggest that axonal retrograde transport properties of TTC-conjugated nanoparticles are preserved following conjugation, and are able to facilitate nanoparticle transport into the lumbar region of the spinal cord.

#### *A.B.4.5 Nanoparticle biodistribution (in vivo)*

We prepared radiolabeled nanoparticles that were conjugated to either TTC or BSA to determine relative nanoparticle biodistribution and to quantify how effective TTC-conjugated nanoparticles were at penetrating the CNS. Radiolabeled nanoparticles (and PBS negative controls) were injected unilaterally into the quadriceps of mice. Mice were sacrificed after 48 hours, and the following organs were recovered: heart, spleen, lung, liver, kidney, right quadriceps (injected), left quadriceps, brain, spinal

cord, femur bone, and blood. Tissue was processed and analyzed for radioactivity. Overall, the biodistribution was similar for nanoparticles regardless of whether they were conjugated to TTC or BSA. TTC-conjugated nanoparticles showed lower levels of radioactivity in the brain ( $16.9 \pm 0.7$  vs.  $11.2 \pm 0.35$ ,  $p < 0.01$ ), in the lung ( $18.3 \pm 2.4$  vs.  $11.5 \pm 0.02$ ,  $p < 0.05$ ), and in the heart ( $18.4 \pm 2.8$  vs.  $11.7 \pm 1.5$ ,  $p < 0.05$ ) than BSA-conjugated nanoparticles. This result is most likely a result of high background levels and a small relative level of enhanced transport efficiency of TTC-conjugated nanoparticles relative to those of negative controls. Further studies will be required to further investigate differences in central nervous system delivery that are a result of TTC-mediated delivery and to validate this method as a drug delivery system.

### **A.B.5.0 Conclusions**

We have expanded on our previous studies that showed TTC-conjugated nanoparticles were highly specific for neuroblastoma cells *in vitro*<sup>85</sup>. We showed that riluzole could be encapsulated within biodegradable nanoparticles and released over a period of several days. TTC-conjugated nanoparticles were shown to be biocompatible (as evidenced by H&E staining), transported specifically within the lumbar region of the spinal cord, and co-localized with neurons. However, TTC-conjugated nanoparticles did not show overall a greater level of penetration to the central nervous system. We have developed a drug delivery system with potential to specifically and efficiently target the central nervous system.

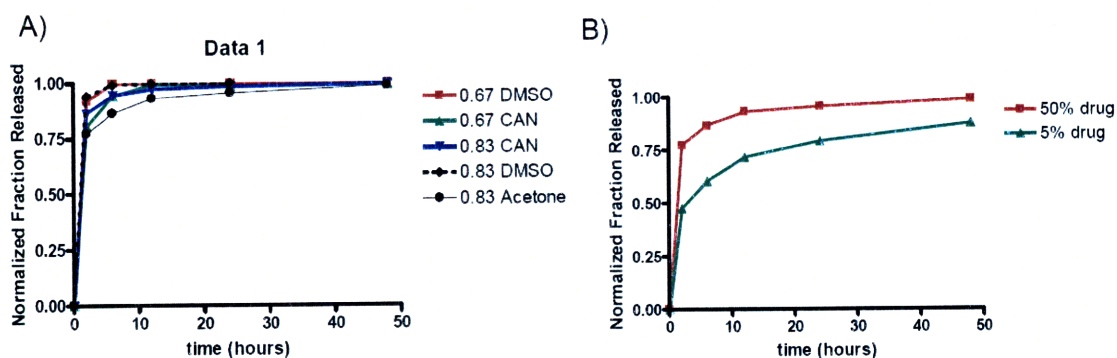
### **A.B.6.0 Acknowledgements**

We would like to thank Sharon Gerecht and Martin Schulz for helpful suggestions during the course of this study, and Weijia Zhang and the MIT Center for Cancer Research for assistance with spinal cord sectioning and histological staining. Seth Townsend was supported by a National Science Foundation Graduate Research Fellowship. This work was supported by grants from Project ALS and CIMIT.



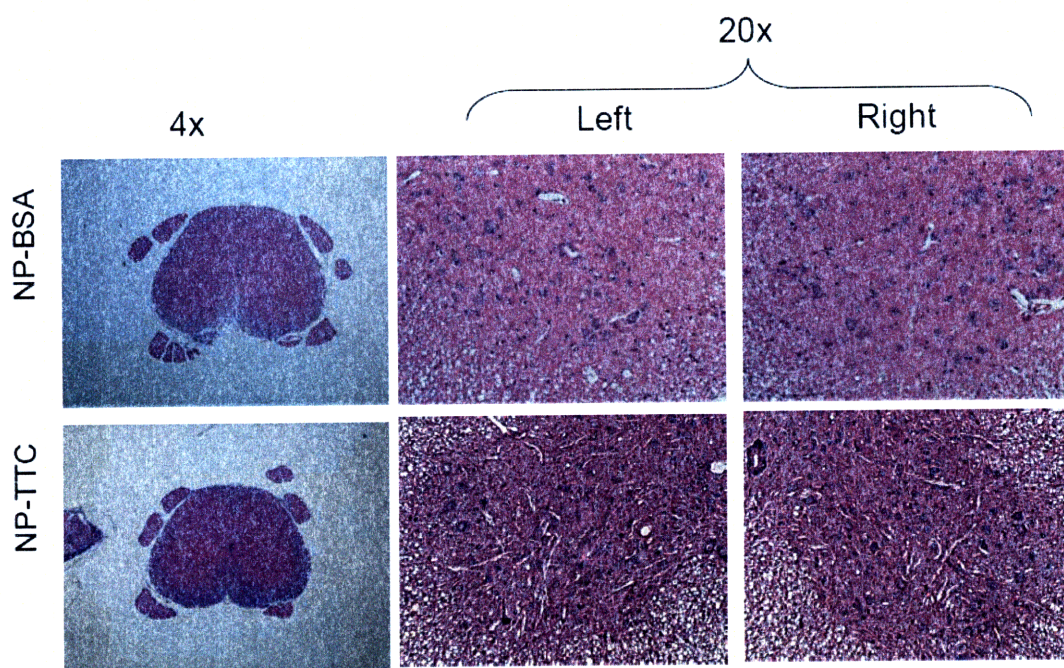
## A.B.7.0 Figures and Figure Legends

Figure 1



*A.B.7.1 Figure 1 – Riluzole nanoparticle release kinetics:* (a) Drug release kinetics over 48 hours for riluzole at 50% drug loading (drug to polymer mass ratio) for 0.67 and 0.83 inherent viscosity PLGA-PEG polymers, in acetone, acetonitrile, or DMSO, as indicated. (b) Comparison of drug loading efficiency on release kinetics for 50% and 5% riluzole loading. Drug release kinetics can be controlled by changing drug loading concentrations and polymer ratios, as well as by changing polymer and solvent parameters.



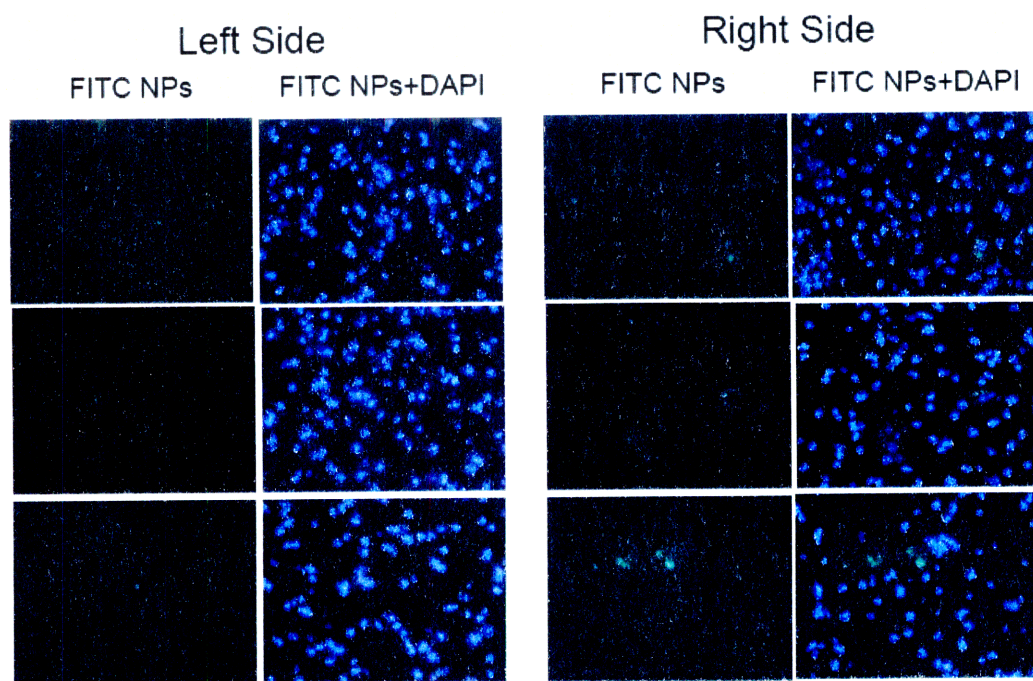


*A.B.7.2 Figure 2 – Haematoxylin and eosin staining of lumbar spinal cord sections following BSA-NP and TTC-NP injections: Mice injected unilaterally with TTC-conjugated or BSA-conjugated nanoparticles were sacrificed 48 hours post injection. Lumbar spinal cords were sectioned, stained with H&E, and imaged for BSA-NP (top) and TTC-NP (bottom), at 4x (left) and 20x (right) magnification. No observable asymmetries between the right and left side, or between the each material injected were observed, suggesting only mild acute inflammation at the spinal cord as a result of the TTC or Gd-TTC conjugate injection and transport.*





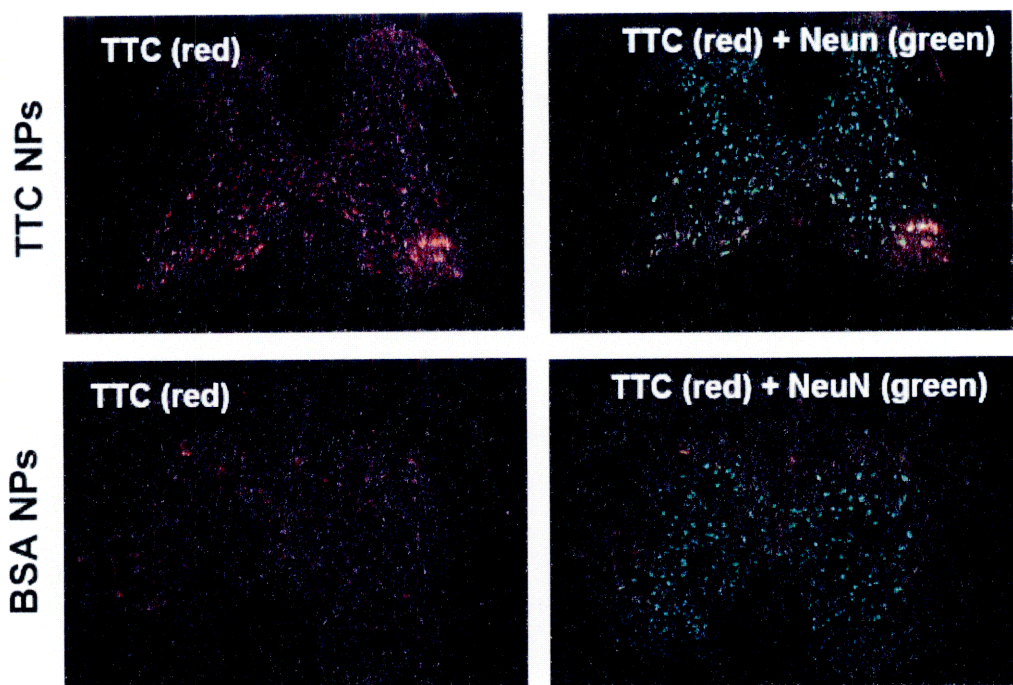
Figure 3



*A.B.7.3 Figure 3 – Retrograde transport for TTC-conjugated nanoparticles to the lumbar spinal cord:* Mice were injected unilaterally with fluorescent TTC-conjugated nanoparticles, sacrificed after 48 hours, and then spinal cords stained with DAPI to investigate nanoparticle localization in the spinal cord. The injection side (right) of the spinal cord shows higher concentration of fluorescent nanoparticles localized within DAPI positive regions, suggesting successful transport to the spinal cord.



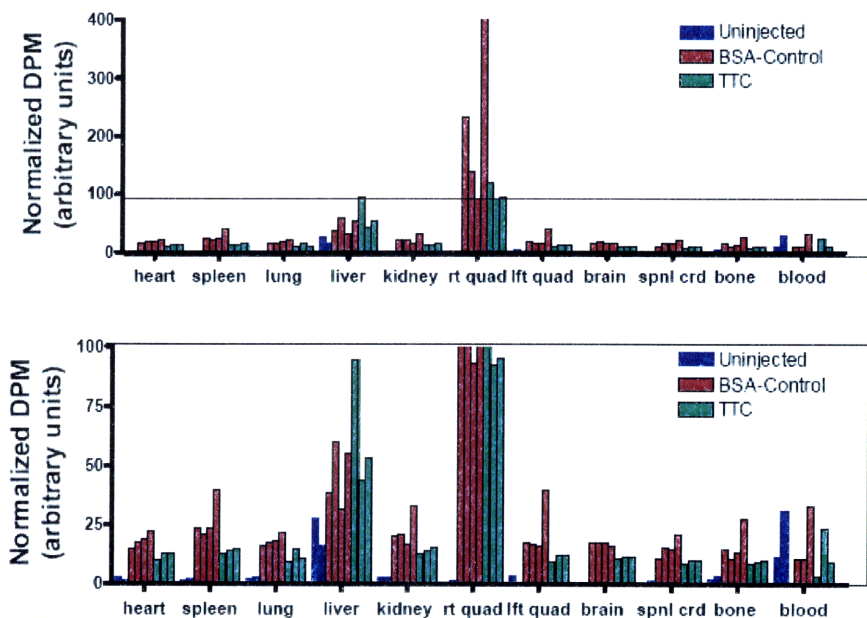
Figure 4



*A.B.7.4 Figure 4 – Immunohistological staining for TTC:* Mice were injected unilaterally with nonfluorescent TTC-NP or BSA-NP and sacrificed 48 hours post injection. The lumbar spinal cord was sectioned and stained for TTC (red) and NeuN (green). Images that were obtained at 4x magnification showed that TTC positive staining was localized unilaterally within the ventral horn of the spinal cord. Merged images showed that TTC and NeuN positive staining were co-localized suggesting specific neuronal uptake of TTC-NP.



Figure 5



A.B.7.5 Figure 5 – *In vivo* biodistribution: Mice were injected with PBS, TTC-NP, or BSA-NP unilaterally and sacrificed 48 hours post injection. Tissue from the following tissue was removed and analyzed for radiolabeled product: heart, spleen, lung, liver, kidney, right quad (injected side), left quadriceps (uninjected side), brain, spinal cord, bone (femur), and blood for low (top) and high (bottom) scale analysis. A high level of agent remained at the site of injection indicating prolonged opportunity for transport via motor neurons. Overall, biodistribution including that in the central nervous system (brain and spinal cord) of BSA and TTC-conjugated nanoparticles were similar.



## **Appendix C: Human embryonic stem cell encapsulation in Matrigel for neuronal differentiation**

### **A.C.1.0 Abstract**

Tissue engineering and stem cell research would move closer to clinical applications in treating amyotrophic lateral sclerosis (ALS, or Lou Gehrig's disease) if pure populations of precursor neural cells could be generated. We encapsulated undifferentiated human embryonic stem cells (hESC) in Matrigel in a 3D culture. hESC developed structures that resembled neural tubules after 4 days in culture and supported cells in colony formation. hESC simultaneously exhibited expression levels for all three germ layers (ectoderm, mesoderm, and endoderm) but stained with greatest intensity in the neural ectoderm (nestin stain). Cells showed positive neural staining including nestin, MAP2, B3-tubulin, Sox1, and TuJ suggesting neuronal differentiation. Additionally, neural tubules were co-localized with increased expression of HIF-1 alpha suggesting that oxygen tension may play a role in neuronal differentiation. Flow cytometry was used to quantify markers for cell undifferentiation and neuronal markers in isolated single cell populations over a 10 day culture in Matrigel. These results suggest that Matrigel could be used as a scaffold for 3D hESC culture and neuronal differentiation.

## A.C.2.0 Introduction

Tissue engineering approaches offer a unique treatment modality for amyotrophic lateral sclerosis (ALS, or Lou Gehrig's disease). One of the requirements of successful treatments is likely the ability of scaffolds to support neuronal differentiation and growth in a 3D environment. Recent studies have characterized some of the differences between 2D and 3D cell culture systems and have demonstrated that biophysical, biomechanical and biochemical forces and signals play a critical role in determining cellular organization and phenotypic expression<sup>177, 205, 206</sup>. These same interactions affect human embryonic stem cells (hESCs) differentiation and morphology<sup>207</sup>. Despite this knowledge, most hESC *in vitro* differentiation studies are carried out in 2D culture, either directly on mouse embryonic fibroblasts (MEFs) or on modified surfaces coated with ECM components such as Matrigel. Researchers have shown that coating a 2D culture plate with Matrigel allows hESCs to remain undifferentiated and pluripotent when grown in MEF conditioned media (CM) and low levels of human basic fibroblast growth factor (hbFGF). Most studies that have used Matrigels to encapsulate cells have not provided a truly 3D conformation because the relative thickness of Matrigel in most studies is small compared to the size of a cell colony<sup>208</sup>. Therefore, the effect of Matrigel in most of these studies is limited to providing ECM components.

One leading application of using 3D cultures is for use with human embryonic stem cell (hESC) culture because these cells are particularly sensitive to the effects of their microenvironment on cell differentiation<sup>209-213</sup>. hESC are used in research because of their clinical uses that involves the repair of damaged organs and for tissue



regeneration, including neuronal injury repair<sup>95,96</sup>. These cells have widespread applications in diseases such as Parkinsons, amyotrophic lateral sclerosis, and spinal cord injury following contact injury<sup>214,215</sup>. A major complication in bringing these therapies to the clinic is developing a system that has high levels of neurons in a mixed stem cell population<sup>216</sup>. hESC cell differentiation and pluripotency are regularly evaluated by undifferentiation markers including Oct4, SSEA4, and Nanog, and evaluated for neuronal cell characteristics by markers including nestin, MAP2, and beta tubulin<sup>217</sup>. The expression levels of these proteins can be induced by certain growth factors and cytokines, as well as by cell microenvironment scaffolds and binding proteins. Many of these matrix proteins and cytokines are present in Matrigel scaffolds and may direct differentiation<sup>218</sup>.

Our goal is to utilize Matrigel scaffolds for hESC encapsulation within a 3D scaffold, and to evaluate whether this matrix can be used to promote neuronal differentiation.

### **A.C.3.0 Methods**

*A.C.3.1 Cell culture and media:* Two NIH-registered hESC cell lines were used for all studies (H9 and H13, WiCell Research Institute, Madison, WI; p19-30). Human ESCs were grown on an inactivated mouse embryonic fibroblast (MEF) feeder layer in growth medium (80% KnockOut DMEM, supplemented with 20% KnockOut Serum Replacement, 4 ng/ml basic Fibroblast Growth Factor, 1 mM L-glutamine, 0.1 mM  $\beta$ -mercaptoethanol, 1% non-essential amino acids). Human ESCs were passaged every 4-6 days using 1mg/ml type IV collagenase for 20-30 minutes. To produce inactivated MEF, activated MEF (Chemicon) were cultured in 85% DMEM containing 15% FBS, and inactivated for 2 hours with DMEM containing 8ug/mL mitomycin-C (Sigma), detached with 0.25% trypsin, and seeded at a density of  $1.5-3.0 \times 10^5$  cells per well in a gelatin coated 6-well plate. All media components and reagents for hESCs culture were purchased from Invitrogen Corporation (Carlsbad, CA), except for defined FBS, which was purchased from Hyclone (Logan, UT). Cell culture methods were modified from those previously described<sup>105, 172, 219</sup>.

*A.C.3.2 Condition media production:* Mitomycin-C inactivated MEF cells were plated on gelatin coated 6-well plates at 2x normal density. MEF were allowed to attach to the plate for 24 hours, subsequently cultured in hESC media (replaced daily), and removed every 24 hours to produce condition medium as previously described<sup>105</sup>. This protocol was completed for up to 10 days of media collection for each plate. Condition medium was stored at -20 °C until use for up to one month.

*A.C.3.3 Matrigel hESC encapsulation and fixation:* Undifferentiated hESC were removed from culture and encapsulated within Matrigel scaffolds using a custom molding. hESC harvested from one well of a 6-well plate were resuspended in 1 ml Matrigel. 25-100 $\mu$ l of Matrigel was homogeneously poured in each molding and solidified at RT for 10 min. The resulting cell encapsulated scaffolds were transferred into the wells of a 24-well Ultralow adhesion plates (Corning) containing 1 ml of condition media. Condition media was changed daily. Scaffolds were removed from culture at pre-determined timepoints (0-20 days) and either fixed in Accustain (Sigma) formalin-free fixative for 20 minutes for histological sectioning and analysis (H&E and peroxidase), or placed in Tissue-Tek OCT gel (Sakura Finetechnical Co, Tokyo, JPN), frozen on dry ice, and stored at -80°C and cryostat sectioned for all immunofluorescent staining.

*A.C.3.4 Hematoxylin and Eosin (H&E) staining:* Matrigel sections stained with H&E were fixed and were prepared as described previously <sup>204</sup>. A Gemini automated (ThermoFisher Scientific; Waltham, MA) staining machine was used for all H&E. Briefly, tissue was dehydrated in graded ethanol (70 to 100%), embedded in paraffin and sectioned axially using a microtome (4 $\mu$ m). Tissue paraffin was removed with 3 changes of xylene, rehydrated with graded ethanol, stained with Harris Hematoxylin (Surgipath Medical; Richmond, IL) for four minutes, and then rinsed with water, 1% acid alcohol (1% HCl in 70% ethanol), and then water in series. Tissue was then stained for blue nuclei using Scott's Tap water substitute (Surgipath Medical; Richmond, IL) for one

minute, washed and ethanol/xylene dehydrated as previously, and mounted. Slides were photographed using an inverted Nikon light microscope.

*A.C.3.5 Immunofluorescence:* Cryosections were thawed and fixed with acetone for 5min at room temperature. After blocking with 5% FBS, sections were stained with a nestin primary antibody (1:100 dilution, one hour) and an anti-mouse-Cy3 secondary antibody (1:50 dilution, 30 minutes). Sections were then incubated with DAPI (1:200 dilution, 2 minutes) and mounted with fluorescent mounting medium (Dako). Negative controls lacking either a primary or secondary antibody were used to verify specificity and to determine minimal background levels. The immuno-labeled cells were examined using a Zeiss fluorescence microscopy (Zeiss, Germany).

*A.C.3.6 Immunohistochemistry and peroxidase staining:* Matrigel sections were embedded in paraffin prior to microtome sectioning (5µm slices). The EnVision and LSAB DakoCytomation kits were used for all immunohistochemically according to the manufacturer's directions. Briefly, paraffin was removed by a xylene-ethanol dehydration and permeabilized using 1 % Triton X100 (Sigma) with 1 % (w/v) BSA in PBS for 10 min. Sections were incubated with a primary antibody for each germ layer (CD34 at 1:20, nestin at 1:20-100, or alpha-fetoprotein at 1:200), HIF-1 alpha (1:50), or neuronal markers (nestin at 1:100, beta 3-tubulin at 1:20-200, TuJ at 1:50, Sox1 at 1:20-100, or MAP2 at 1:50-200). Primary antibodies were incubated with a Dako diluent (Dako) and incubated for 1 h at RT. The samples were then biotinylated for 30 minutes, incubated with streptavidin-HRP for 30 minutes, and then a DAB chromogen substrate until color

change was detected (~1-5 minutes). Samples were washed with PBS in between each incubation, and each set of samples was incubated with DAB for the same time for each antibody. Samples were then counterstained with a 1:4 dilution of Gill's hematoxylin solution (Electron Microscopy Science) for 2-3 min. Samples were mounted and photographed using a light microscope.

*A.C.3.7 Flow cytometry:* Cells that were removed from Matrigel were analyzed using a FACScan flow cytometer (Becton Dickinson) to measure fluorescence (488nm excitation, 530nm and 650nm emission). Cells were incubated with trypsin for 7 minutes at 37C, inactivated, and then with dispase (50U/mL) to produce a single cell suspension. A cell pellet was incubated with Intrastain fixative (Dako) for 15 minutes at RT, and subsequently permeabilized according to the manufacturer's directions. Cells were incubated with a fluorescent antibody including differentiation markers (Oct4-FITC, SSEA4-PE, or Nanog-FITC), and neuronal markers (nestin-PE, B3-Tubulin-FITC, or MAP2-FITC). Unbound antibody was removed by 3 washes in PBS and incubated with propidium iodide (5ug/mL), and cell populations were gated based on forward/side scatter and propidium iodide fluorescence to remove debris and dead cells from analysis. A total of at least 10,000 gated events were obtained for each sample. Data was analyzed using FlowJo software (Tree Star) to generate histograms of each sample.

## **A.C.4.0 Results and Discussion**

### *A.C.4.1 hESC encapsulation within Matrigel and morphology*

We hypothesized that Matrigel could be used to encapsulate stem cells, and that the growth factors and matrix proteins within the material may promote neuronal differentiation of undifferentiated human embryonic stem cells. Prior to these studies, Matrigel has been used primarily as a dilute material to plate 2D culture dishes, or as a partially embedded cell culture system. We instead utilized a custom molding and non-diluted Matrigel to encapsulate undifferentiated human embryonic stem cells. hESC in Matrigel showed cell spreading and the formation of tubule structures after a period of 4 days in culture by light microscopy (Figure 1). Cell spreading and protrusions were interconnected and resembled axon structures. This is in contrast to the characteristic morphology of undifferentiated hESC that grow together in colonies.

hESC that were embedded and directly analyzed by thin section H&E staining showed morphology that resembled undifferentiated cells, suggesting that the method of analysis did not lead to this morphology. This is in contrast to the distinct formation of neuronal tubule structures after 4 and 10 days in Matrigel culture (Figure 2). hESC continued to group into colonies and support each other, but organized into neural formations. Cells did not form single cell formation suggesting continued cooperation through cell signaling and matrix molecules that may further induce differentiation.

We then investigated whether morphology of encapsulated hESC was affected by the size of the Matrigel scaffold. We prepared gels of sizes between 25uL and 100uL with the same diameter and cultured hESC for between 4 and 10 days (Figure 3).

Scaffolds that were formed showed greater density in the overall scaffold and resulting cell colonies in 25uL gels than in larger 100uL gels, suggesting greater rates of proliferation in smaller scaffolds. This may be a function of oxygen or micronutrient consumption and resulting cell colonies. Overall, morphology was similar between scaffolds and more investigation is needed to fully quantify differences in the scaffolds.

#### *A.C.4.2 Expression of differentiation markers after Matrigel encapsulation*

We then further investigated differentiation in hESC during Matrigel encapsulation and culture. Matrigel scaffolds with hESC were cultured for 4-20 days and stained for each layer of the germ layers and compared with undifferentiated controls (Figure 4). hESC showed staining that was positive for each germ layer, however nestin and ectoderm positive staining was significantly more intense and localized within neuronal tubules than  $\alpha$ -Fetoprotein (endoderm) or CD34 (mesoderm). These data further suggest neuronal differentiation.

#### *A.C.4.3 Immunohistochemistry and neuronal differentiation*

We investigated neuronal differentiation to further investigate the presence of markers for neuronal differentiation. Matrigel scaffolds that were sectioned and stained showed positive staining for B3-tubulin after 4 days, for Sox1 after 20 days, for TuJ after 4 days, and MAP2 after 10 days in culture (Figure 5). Cell stains show positivity for neuronal markers localized in neuron tubules. Additionally, there did not appear to be visible or quantitative differences in expression levels between 4, 10, and 20 days in culture for any of the neuronal markers (data not shown). In general, B3-tubulin and TuJ

stains (both staining for tubulin but on different epitopes) showed positive but less intense staining than nestin. The positive results for nestin staining were also confirmed using immunofluorescence (Figure 6a). These results further give evidence for neuronal differentiation in Matrigel scaffolds.

We next explored possible mechanisms for neuronal differentiation. In addition to growth factors and matrix proteins that are present in Matrigel, oxygen tension could play a role in neuronal differentiation. We next stained for HIF-1 alpha to investigate localization. As predicted, we also observed high levels of this transcription factor localized within neurotubules. These results suggest that oxygen tension may play a critical role in neuronal differentiation and are consistent with previous studies<sup>220</sup>.

#### *A.C.4.4 Flow cytometry of differentiation and neuronal markers*

We next quantified relative differences in expression levels for markers of undifferentiated stem cells (nanog, Oct4, and SSEA4) and neuronal markers (nestin and MAP2) using flow cytometry. Cells were cultured for 0, 4, or 10 days in a Matrigel and then removed and analyzed as single cells in suspension (Figure 7). Cells showed relatively unchanged levels of expression of nanog and Oct4 expression, and higher levels of SSEA4 expression after Matrigel culture. The SSEA4 levels were not predicted and cannot be easily explained, but it should be noted that even undifferentiated cells have highly variable expression levels of SSEA4.

In contrast, hESC showed significantly higher levels of nestin and MAP2 over the culture period. Interestingly, undifferentiated cells showed a dual peak in expression of MAP2 suggesting high basal levels of this neuronal marker in undifferentiated cells.



Separate cell samples were stained with multiple antibodies for either neuronal or undifferentiation markers. Results for these experiments were similar to those presented for single antibody stains (results not shown). Cells were also stained with negative controls for each isotype antibody to investigate non-specific binding and showed only background levels of fluorescence (data not shown). Taken together, these results suggest a high fraction of neuronal markers and expression over the Matrigel culture.

### **A.C.5.0 Conclusions**

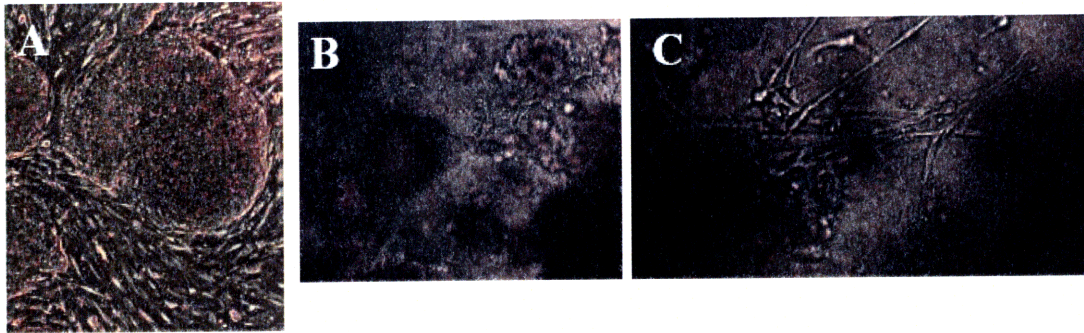
We have provided studies that demonstrate that hESC can be cultured by Matrigel encapsulation. Matrigel scaffolds promote the formation of neuronal tubules and express in these cells neuronal markers including nestin and MAP2. Cells furthermore showed HIF-1 alpha localization suggesting oxygen tension may play a role in neuronal differentiation. Flow cytometry confirmed quantitative differences in both markers for hESC undifferentiation and neuronal markers over a 10 day Matrigel culture.

### **A.C.6.0 Acknowledgements**

We would like to thank Heather Pressler for assistance with cell culture, and Weijia Zhang at the MIT Center for Cancer Research for histological analysis and H&E staining assistance. This work that was presented here in this appendix was partially conducted by Martin Schulz and used for his Master's thesis in Germany. Seth Townsend is supported by a National Science Foundation Graduate Research Fellowship.

## **A.C.7.0 Figure Legends**

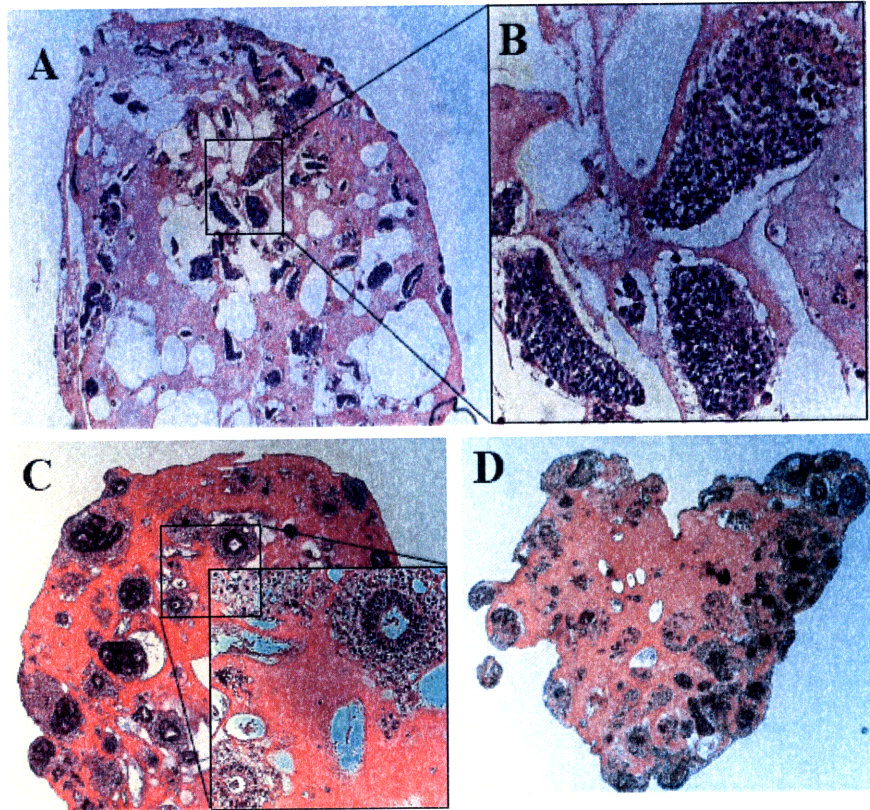
**Figure 1**



*A.C.7.1 Figure 1 – Light microscopy of hESC encapsulated within Matrigel: (a) undifferentiated hESC on a MEF feeder layer exhibiting characteristic colonies with elongated MEF. (b) Differentiated hESC encapsulated within a 3D Matrigel scaffold after 4 days in culture as visualized by light microscopy. (c) higher resolution image of hESC in Matrigel scaffolds after 4 days in culture showing characteristic cell spreading resembling neuronal tubules.*



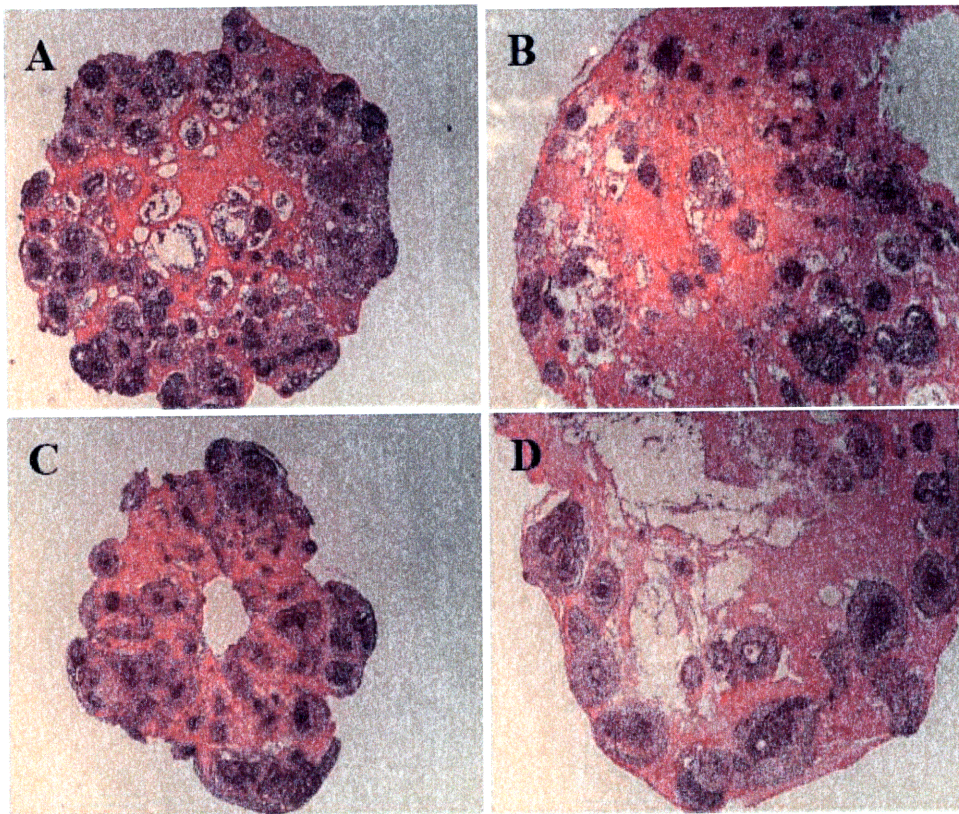
Figure 2



*A.C.7.2 Figure 2 – hESC encapsulated within Matrigel: (a) undifferentiated hESC encapsulated in Matrigel showing characteristic cell morphology. (b) region of interest in the enlarged region of (a). (c) hESC after 4 days of Matrigel encapsulation showing neuron tubule formation with an enlarged region of interest. (d) hESC after 10 days in culture exhibiting neuron tubule formation.*



**Figure 3**

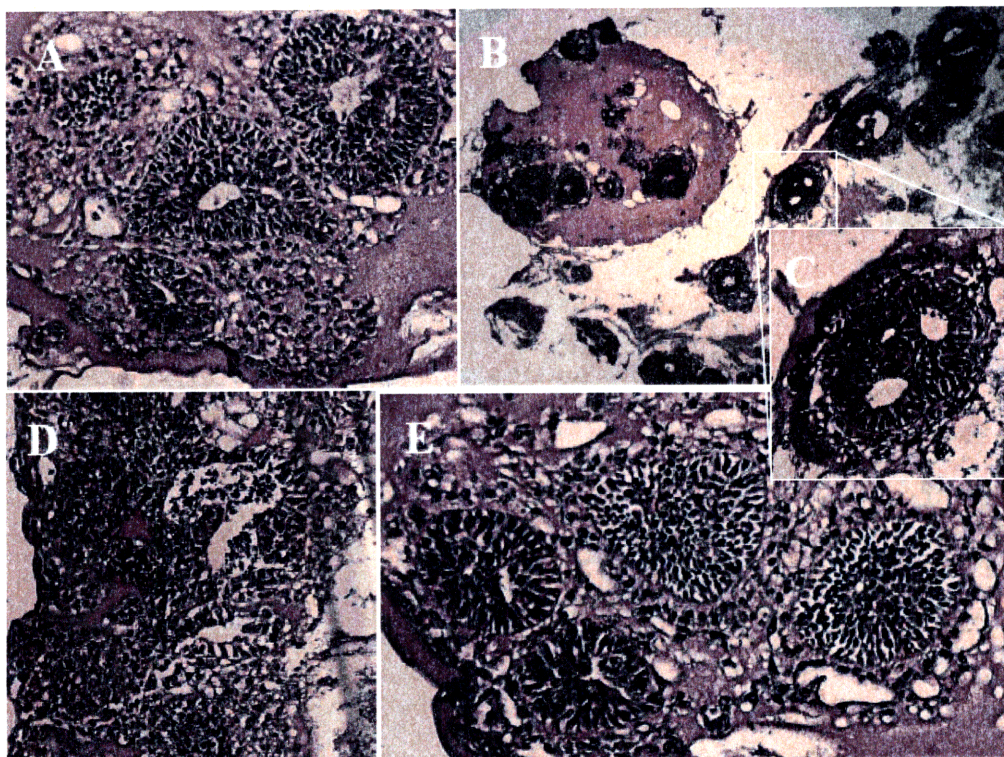


*A.C.7.3 Figure 3 – hESC encapsulated within Matrigel of different sizes affecting morphology: hESC encapsulated within Matrigels after 4 days (a, b) for a 25uL (a) and 100uL Matrigel scaffold (b), and after 10 days (c, d) for 25uL (c) and 100uL (d) scaffolds. The size of the Matrigel scaffold impacts overall cell morphology and density.*





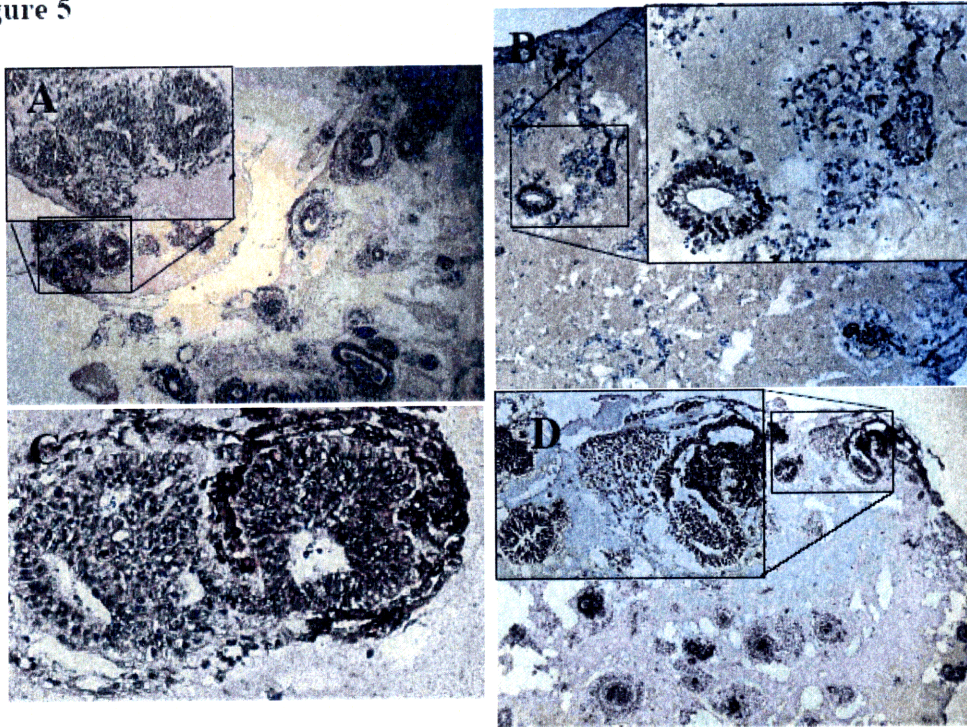
**Figure 4**



*A.C.7.4 Figure 4 – Germ layer staining of hESC encapsulated within Matrigel after 4 days in culture: (a) undifferentiated control cells, (b, c) nestin for ectoderm at 50x (b) and 200x (c) magnification, (d)  $\alpha$ -Fetoprotein for endoderm at 200x, and (e) CD34 for mesoderm at 200x. Cells show strong positivity for nestin relative to other germ layers.*



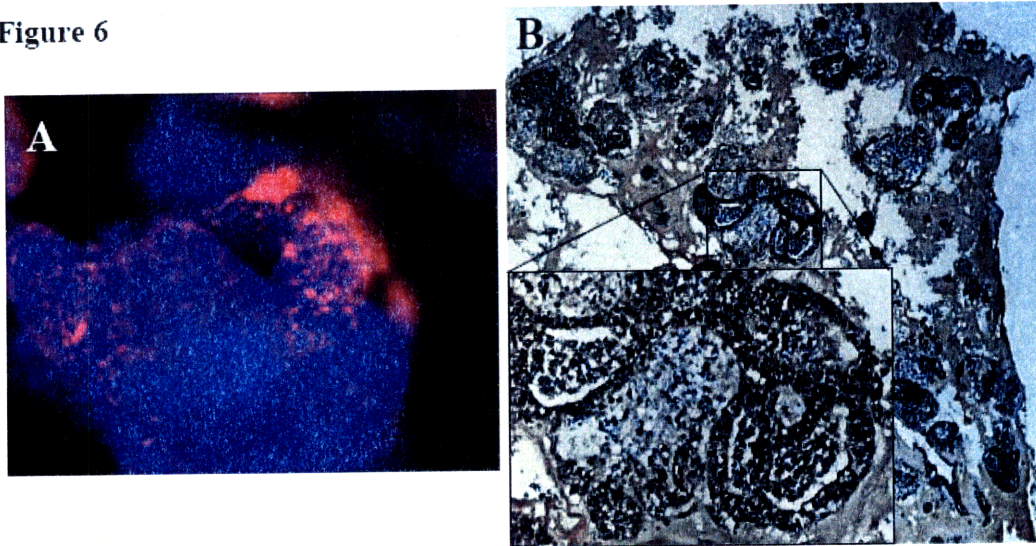
Figure 5



*A.C.7.5 Figure 5 – Neuronal staining of hESC encapsulated in Matrigel: (a) day 4 B3-tubulin, (b) day 20 Sox1, (c) day 4 TuJ, and (d) day 10 MAP2. Cell stains show positivity for neuronal markers localized in neuron tubules.*



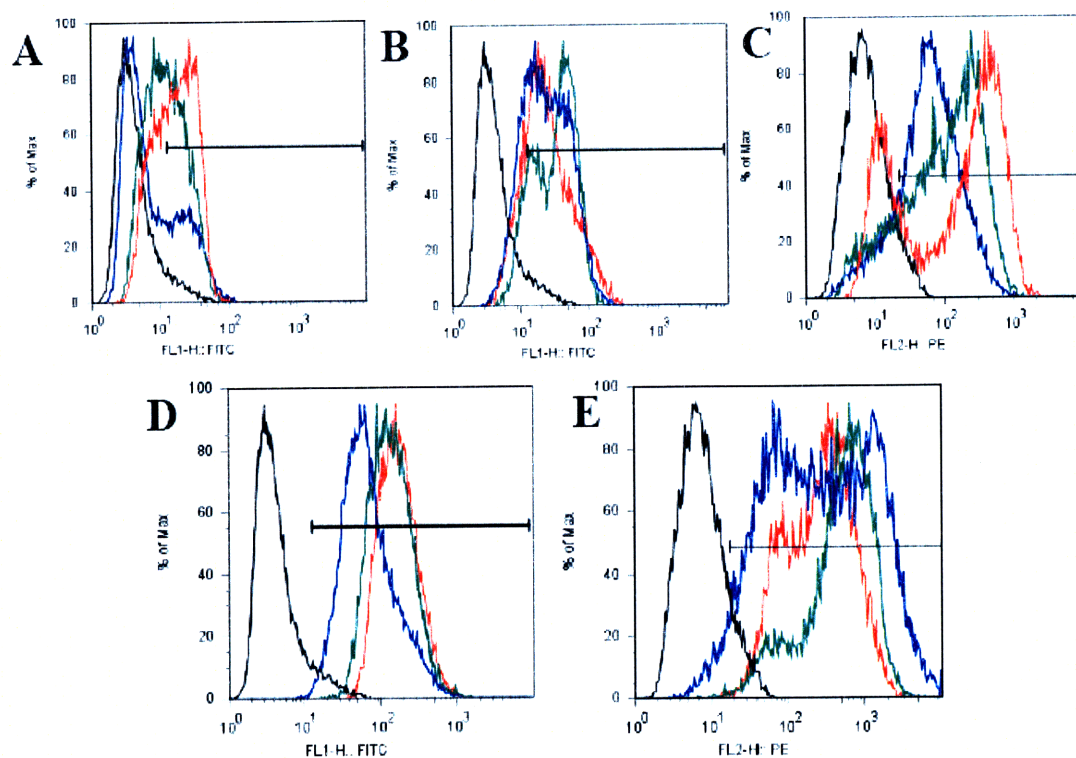
**Figure 6**



*A.C.7.6 Figure 6 – Immunofluorescent and immunohistochemistry staining of hESC in Matrigel: (a) immunofluorescent staining for DAPI (blue) and nestin (red) after 4 days in culture, and (b) HIF-1 $\alpha$  after 4 days in Matrigel culture. Nestin staining shows distinct clusters of neuronal marker positive staining, and HIF-1 $\alpha$  localization suggests the mechanism for neuronal differentiation in Matrigel.*



**Figure 7**



*A.C.7.7 Figure 7 – Flow cytometry of single cell hESC populations after Matrigel culture: Flow cytometry results of (a) Nanog, (b) Oct4, (c) SSEA4, (d) MAP2, and (e) nestin. Cell populations in each sample include unstained cells (black), undifferentiated cells (blue), day 4 Matrigel encapsulated cells (green), and day 10 Matrigel encapsulated cells (red). Each cell population includes only gated events and includes at least 10,000 counted cells.*





## Appendix D: Chemical structures and predicted NMR

Figure 1: PLGA-PEG-Biotin and PLGA-PEG-Biotin structure

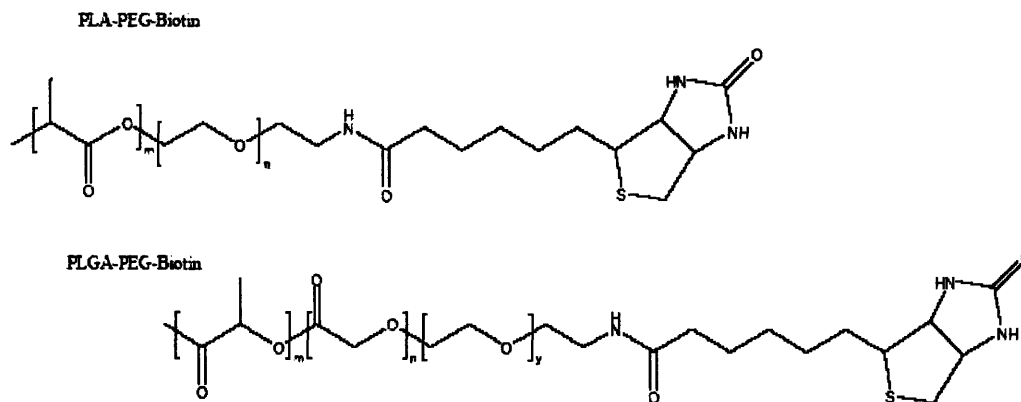


Figure 2: NHS, EDC, and Sulfo-NHS Structure

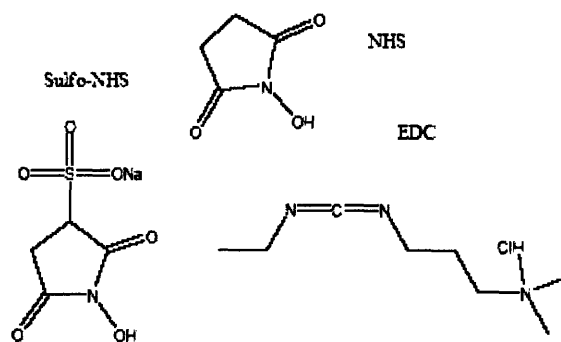


Figure 3: Sulfo-NHS-Biotin and NH<sub>2</sub>-PEG-Biotin Structure

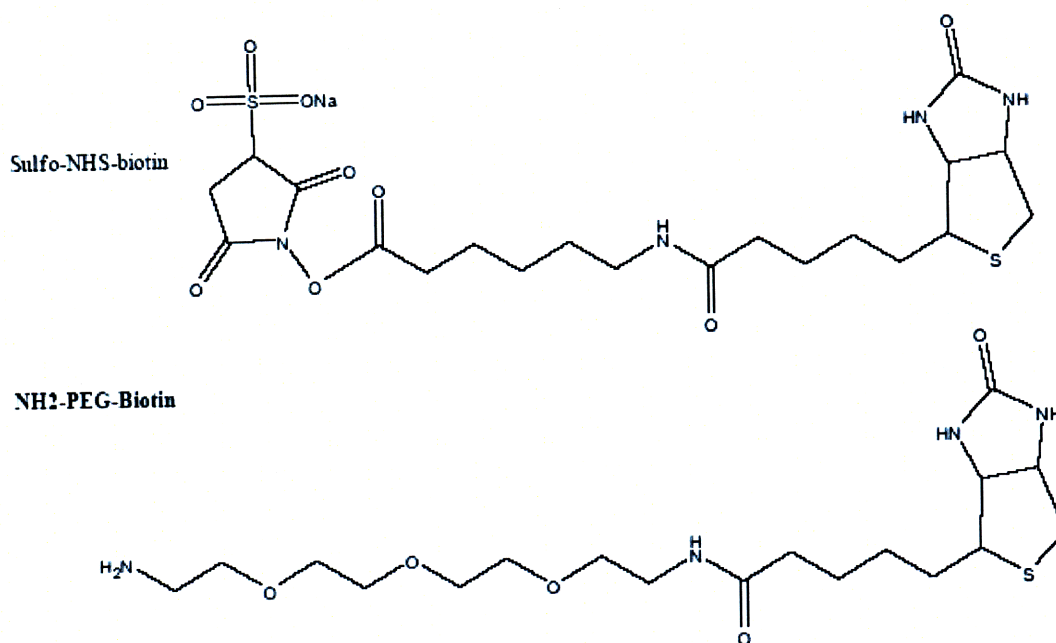
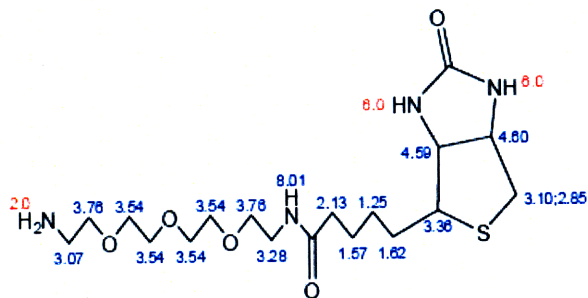


Figure 4: NH<sub>2</sub>-PEG-Biotin theoretical NMR



Estimation quality is indicated by color: good, medium, rough

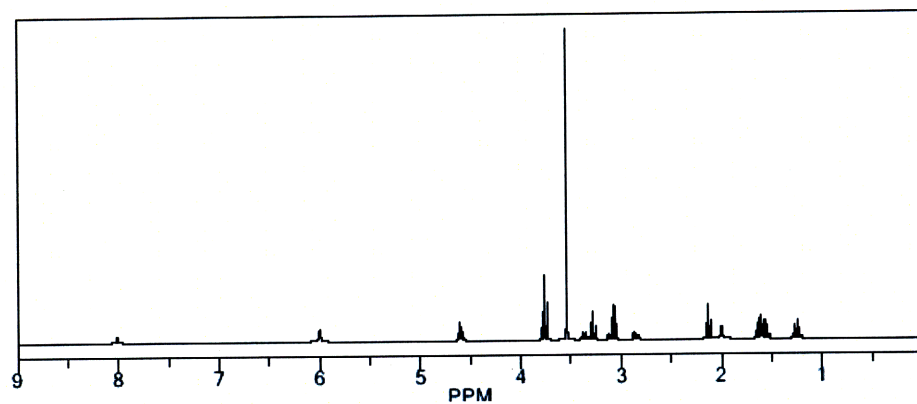
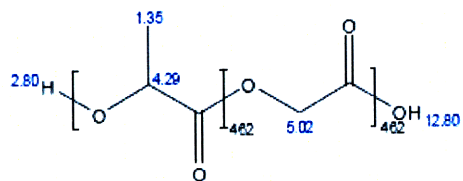


Figure 5: PLGA-COOH Theoretical NMR



Estimation quality is indicated by color: good, medium, rough

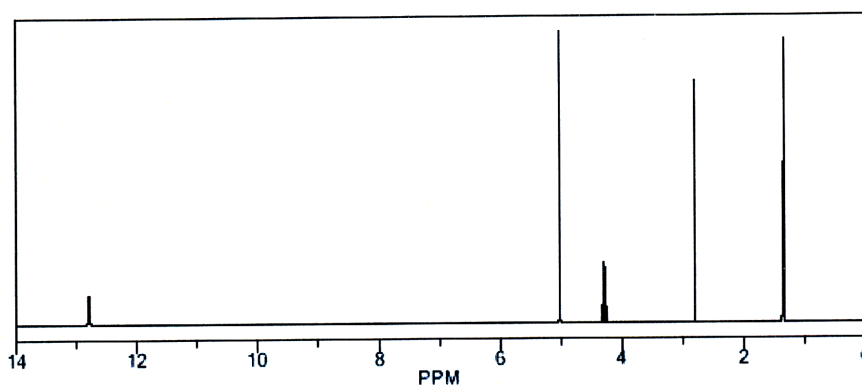
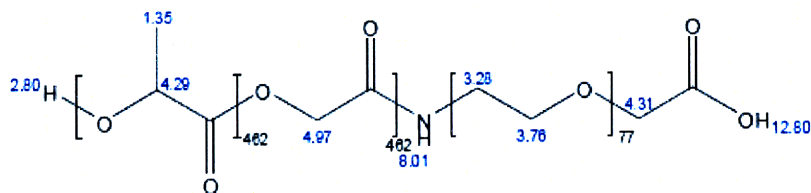


Figure 6: PLGA-PEG-COOH Theoretical NMR



Estimation quality is indicated by color: good, medium, rough

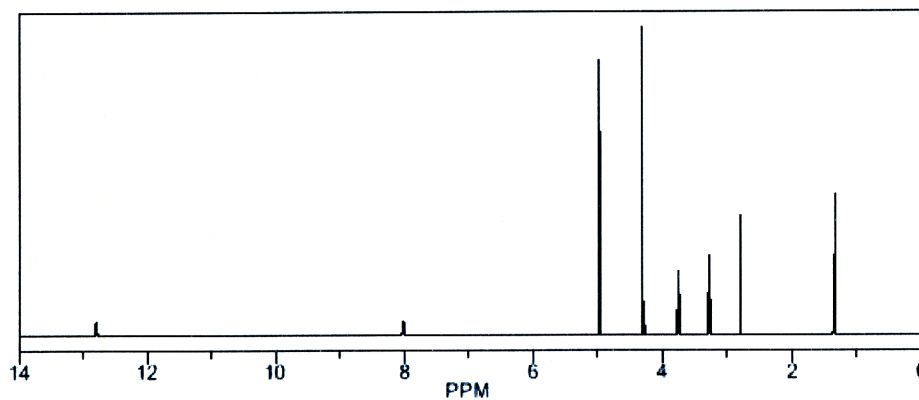
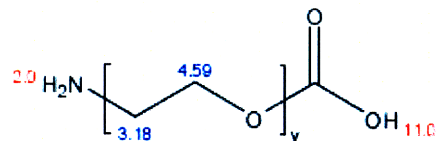


Figure 7: NH<sub>2</sub>-PEG-COOH Theoretical NMR



Estimation quality is indicated by color: good, medium, rough

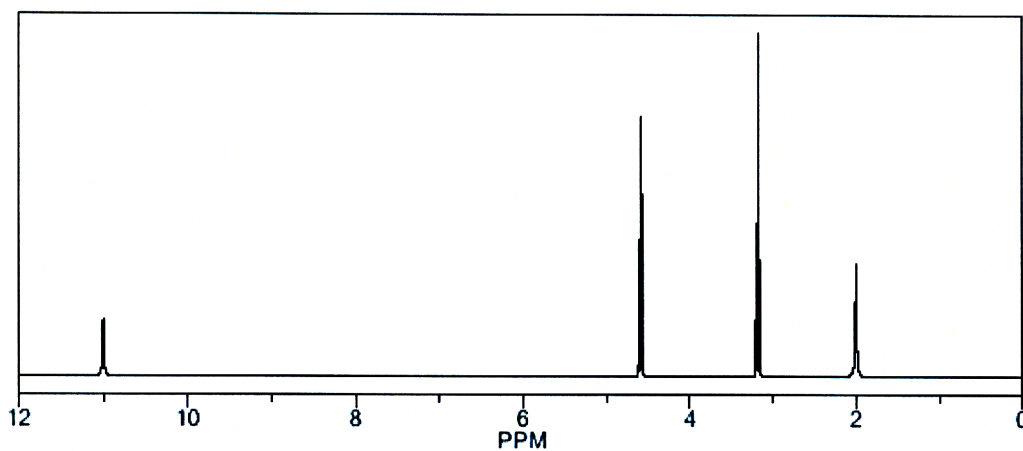
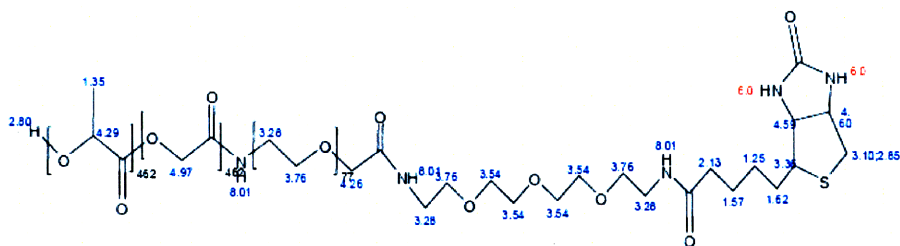


Figure 8: PLGA-PEG-Biotin Theoretical NMR



Estimation quality is indicated by color: good, medium, rough

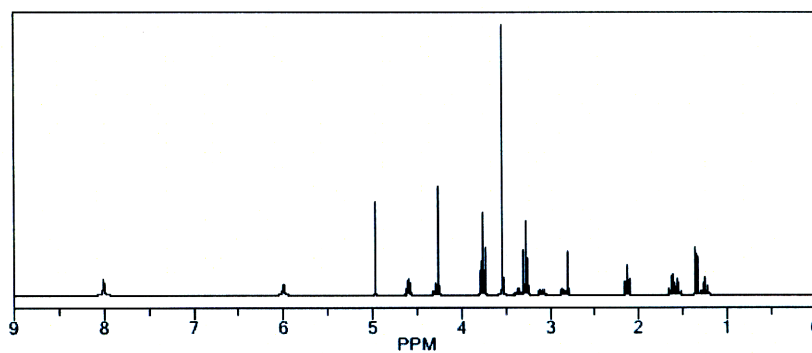
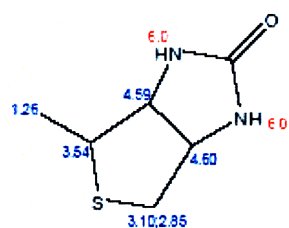


Figure 9: Biotin: Theoretical NMR



Estimation quality is indicated by color: good, medium, rough

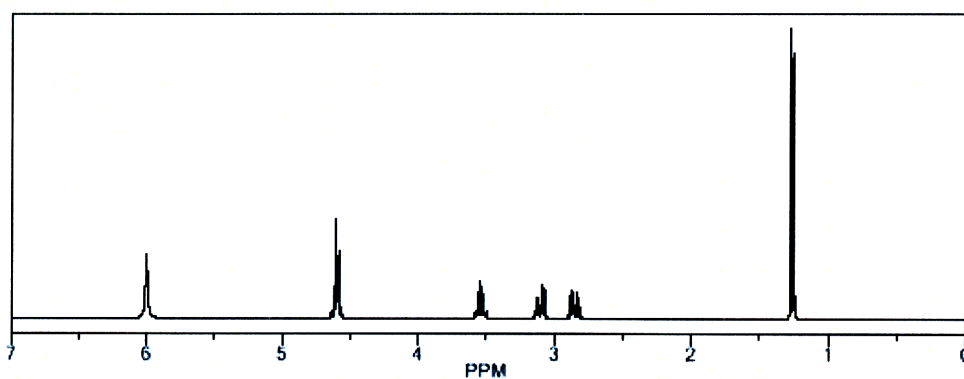
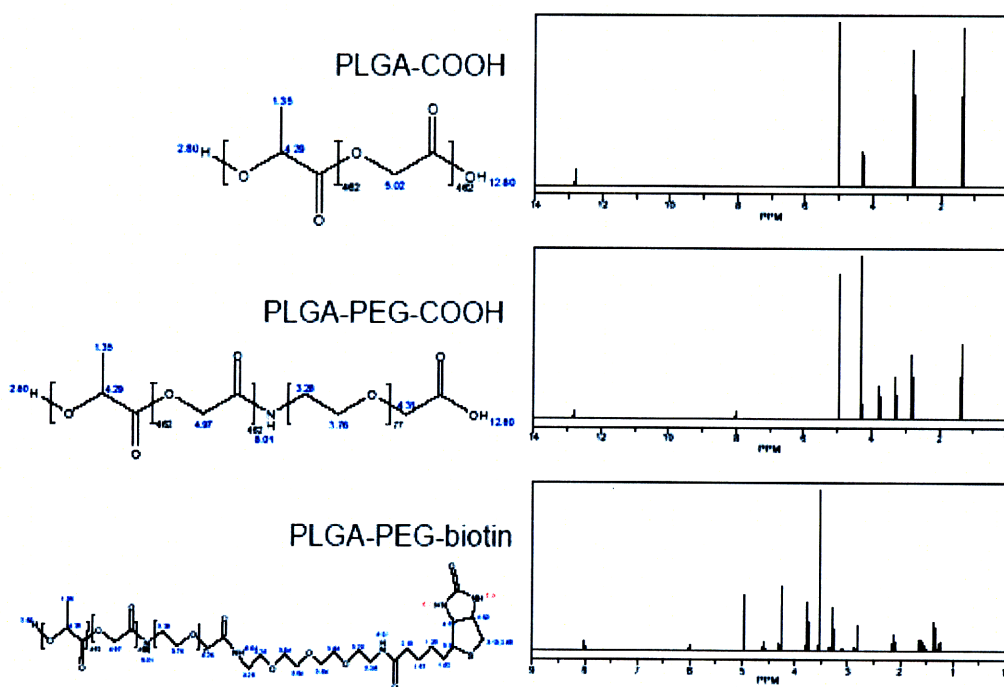
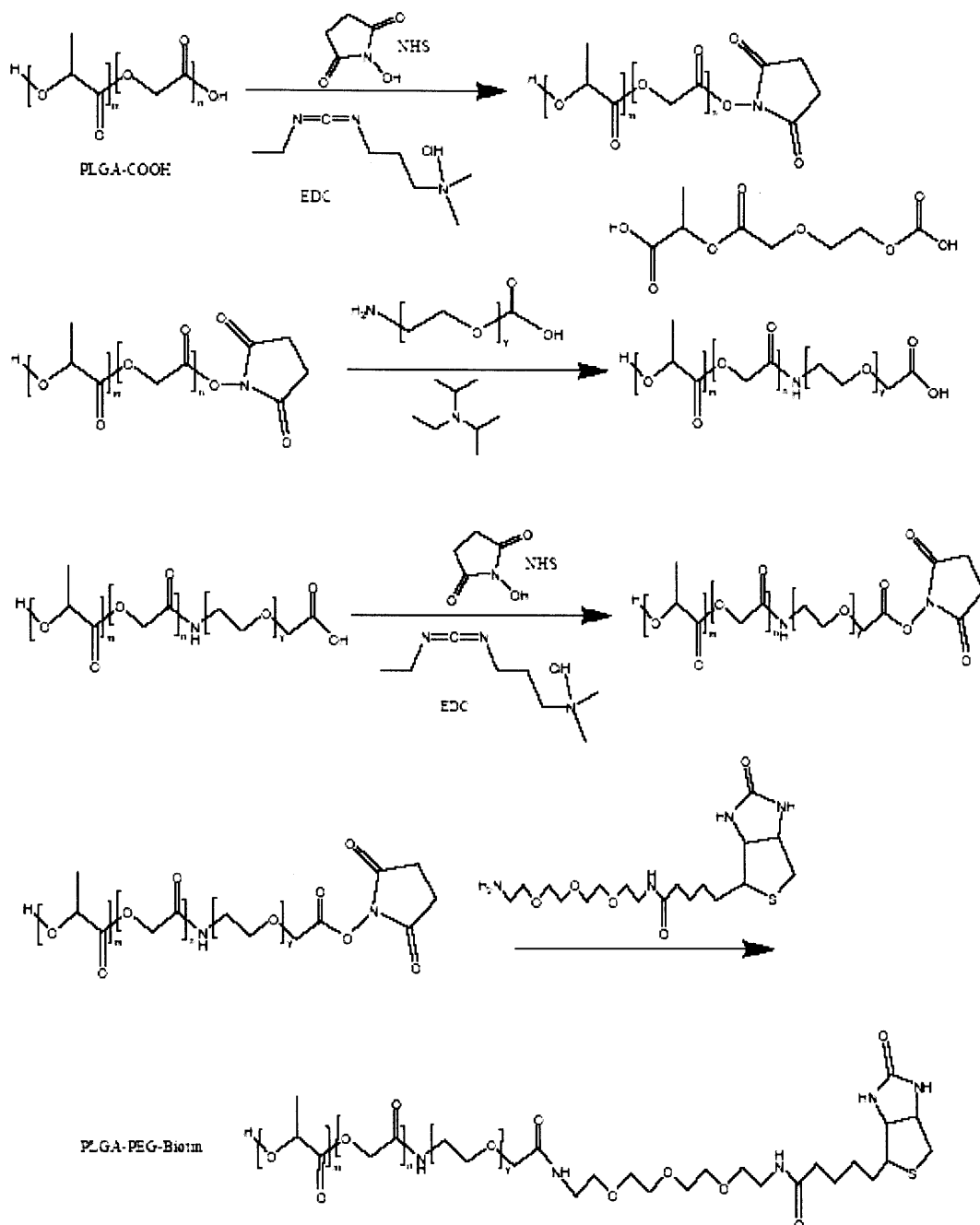


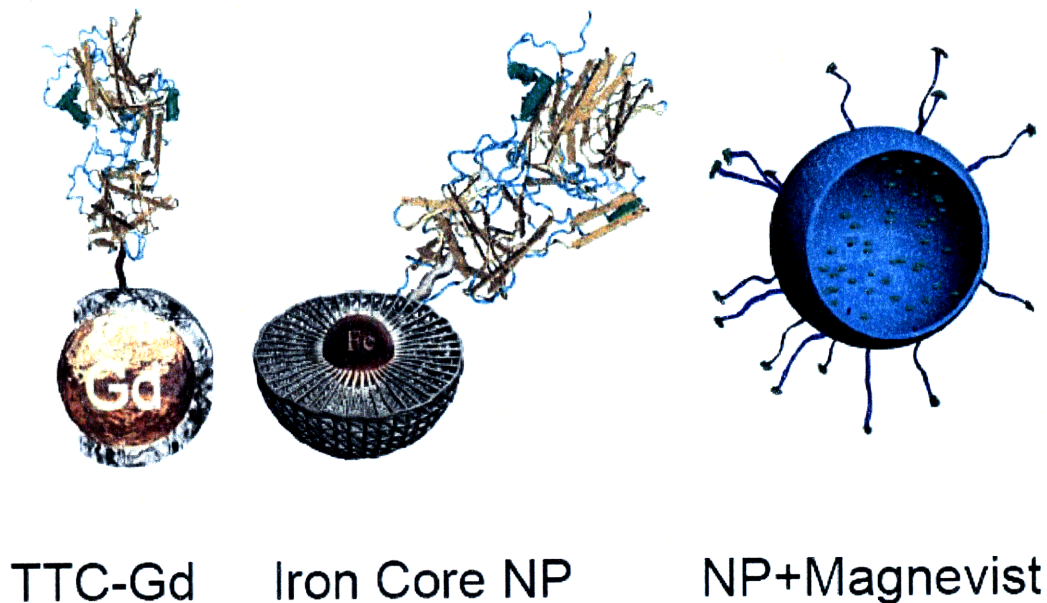
Figure 10: Summary predicted polymer NMR



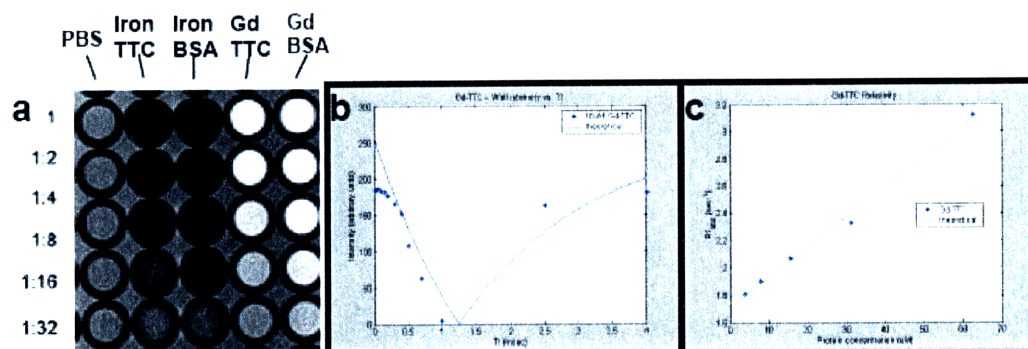
## Appendix E: Synthesis of PLGA-PEG-biotin



## Appendix F: Schematics of MRI contrast agent biomarkers



## Appendix G: Additional analysis of MRI relaxivity



*Gadolinium*

$$M_z(TI) = M_0 abs \left[ 1 - 2 \exp \left( \frac{-TI}{T_1} \right) \right]$$

$$R_{1,obs} = R_1 + R_{1,Gd} [Gd]$$

*Iron*

$$S(TE) = S_0 \left[ \exp(-TE/T_2) \right]$$

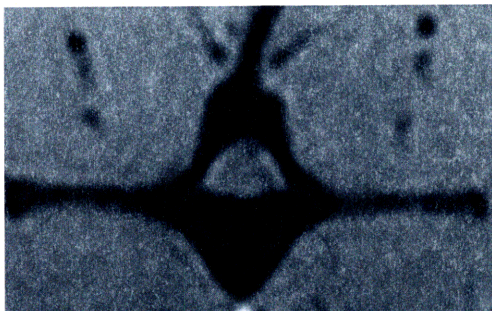
$$R_{2,obs} = R_2 + R_{2,Fe} [Fe]$$



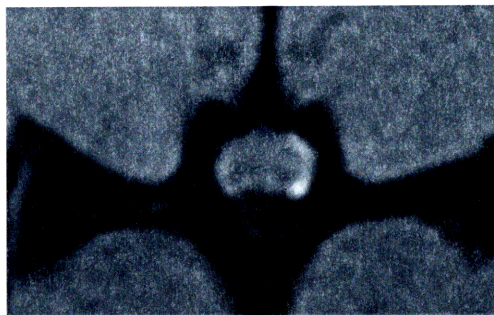
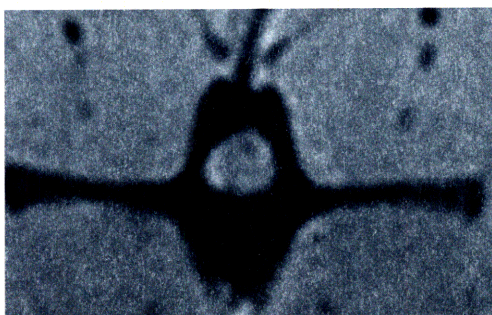
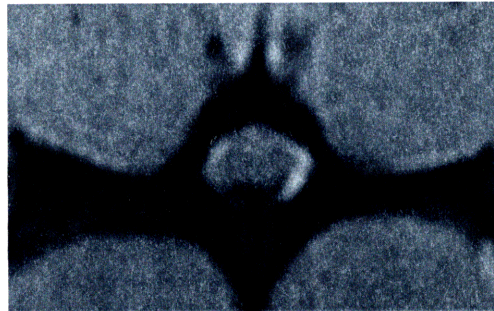


## Appendix H: 4.7T MRI Imaging (*in vivo*)

Thoracic



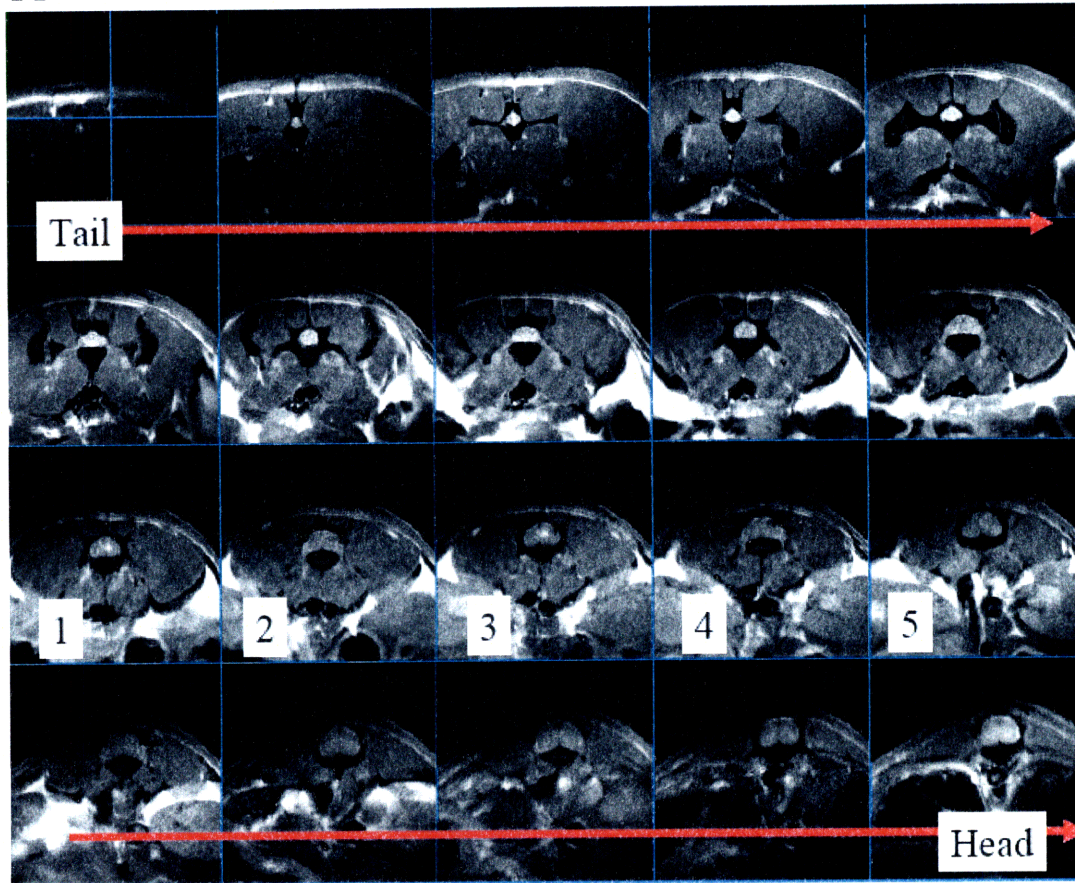
Lumbar



5/3/07

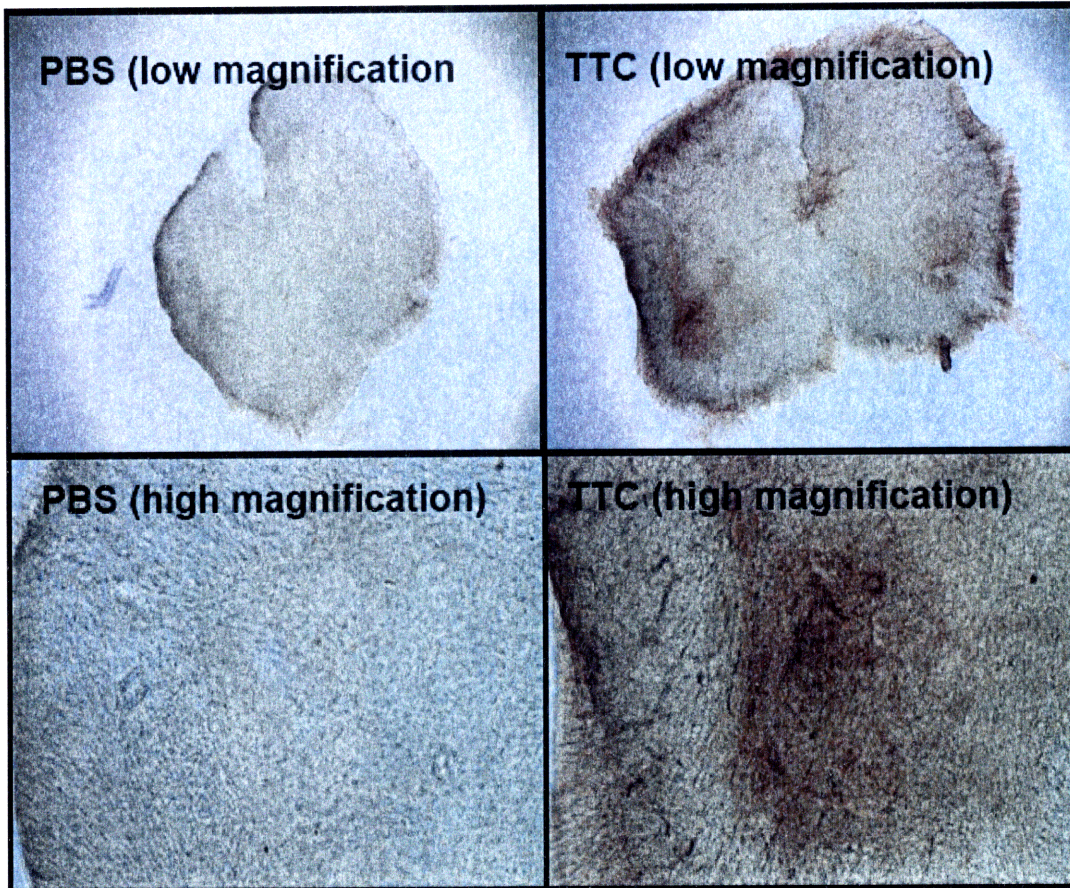


## Appendix I: 9.4T MRI Imaging (in vivo)





## Appendix J: Spinal cord staining of TTC transport (ex vivo)

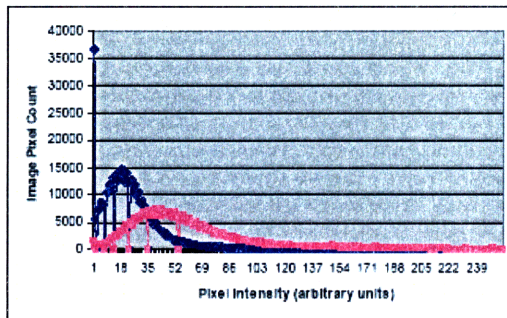




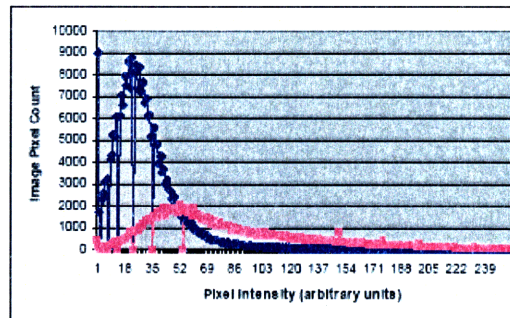
# Appendix K: Additional analysis of IHC and MRI transport quantification

## Immunohistochemistry

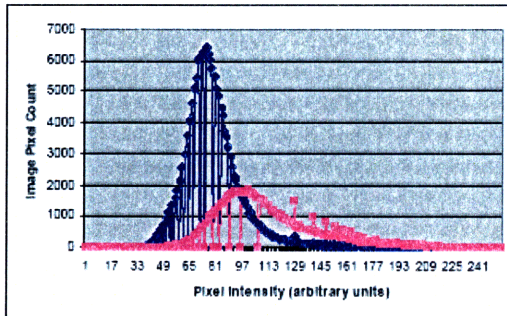
WT



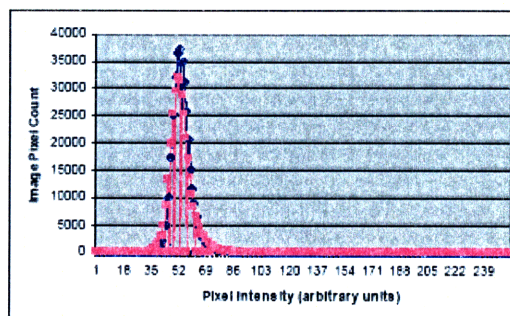
ALS60



ALS90



ALS120



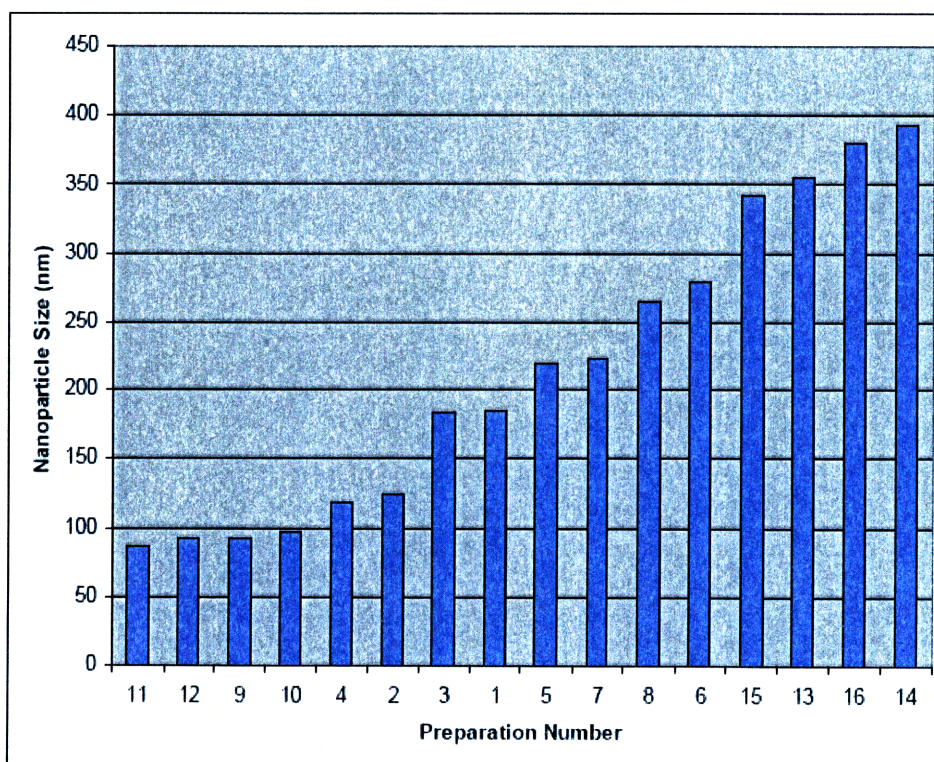




## Appendix L: Nanoparticle preparations to control size

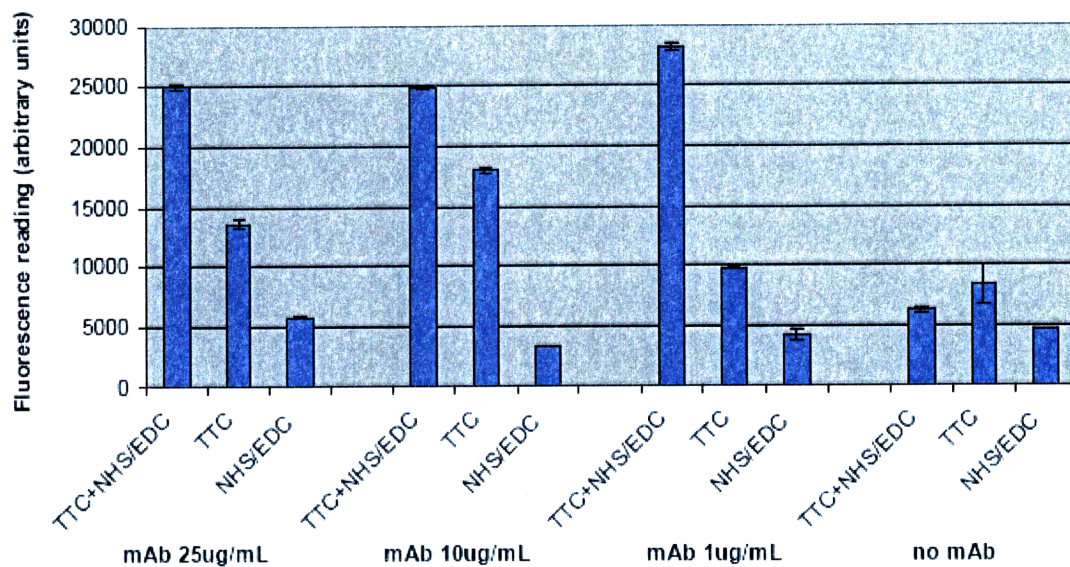
### Nanoparticle Preparation

Preparation	Solvent	Non-Solvent	Polymer	RPM	Size(nm)
1	DMSO	water	PLA	1200	n/a
2	DMSO	water	PLGA	1200	124.6
3	DMSO	water	PLA	2000	n/a
4	DMSO	water	PLGA	2000	119.3
5	DMSO	Ethanol	PLA	1200	219.3
6	DMSO	Ethanol	PLGA	1200	278.9
7	DMSO	Ethanol	PLA	2000	222.7
8	DMSO	Ethanol	PLGA	2000	264.1
9	DMSO	Methanol	PLA	1200	92
10	DMSO	Methanol	PLGA	1200	98.4
11	DMSO	Methanol	PLA	2000	86
12	DMSO	Methanol	PLGA	2000	91.9
13	DMSO	Isopropanol	PLA	1200	355.6
14	DMSO	Isopropanol	PLGA	1200	392.6
15	DMSO	Isopropanol	PLA	2000	342.1
16	DMSO	Isopropanol	PLGA	2000	380.6





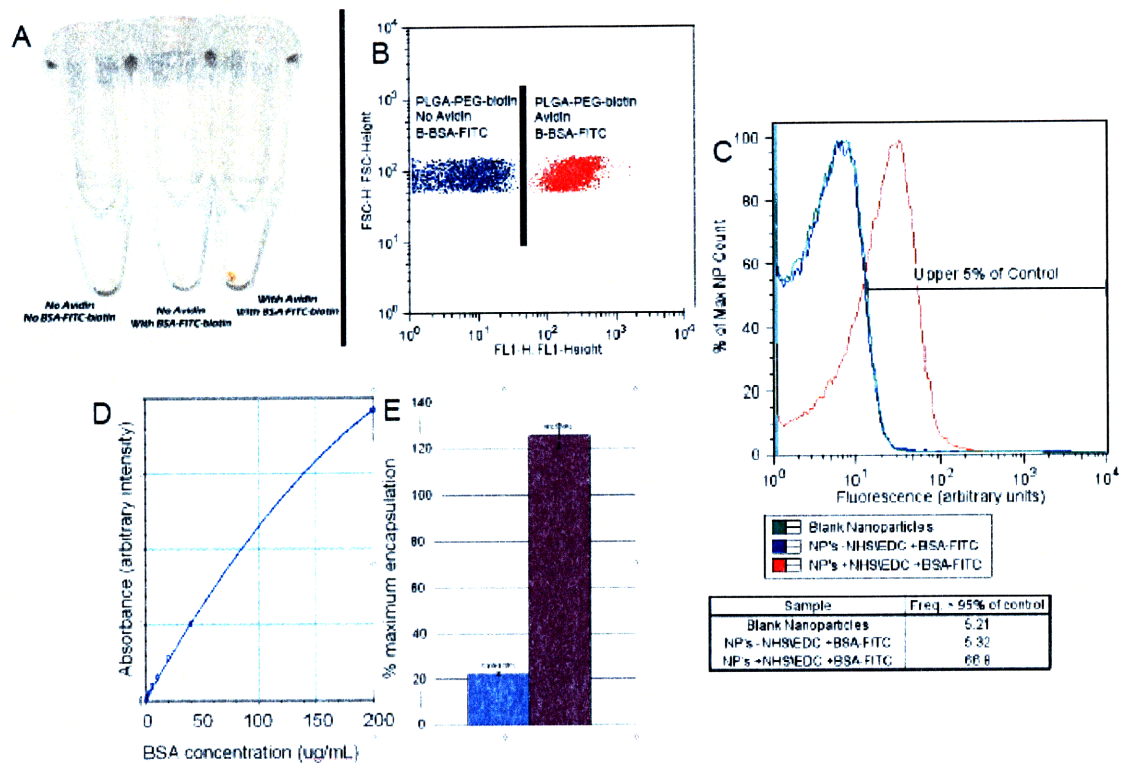
## Appendix M: Immunohistochemistry staining of TTC-conjugated nanoparticles



Monoclonal antibody: Roche mouse IgG for TTC  
Secondary antibody: Alexa Fluor 488 Goat anti-mouse IgG (10ug/mL)

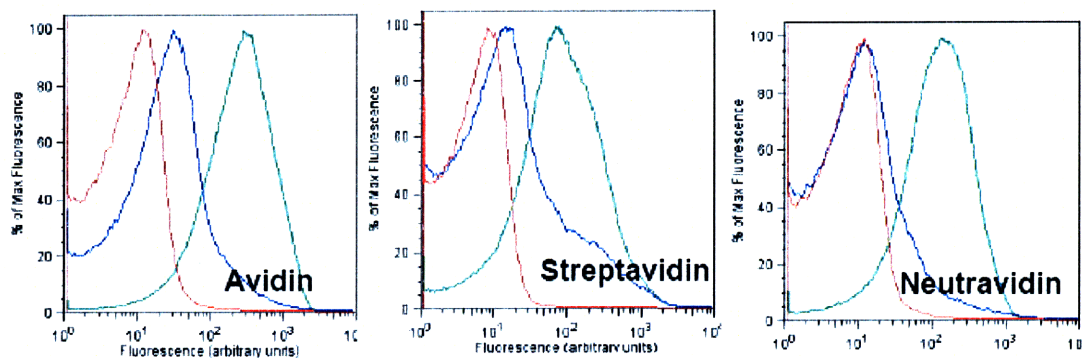


## Appendix N: Nanoparticle protein encapsulation and conjugation



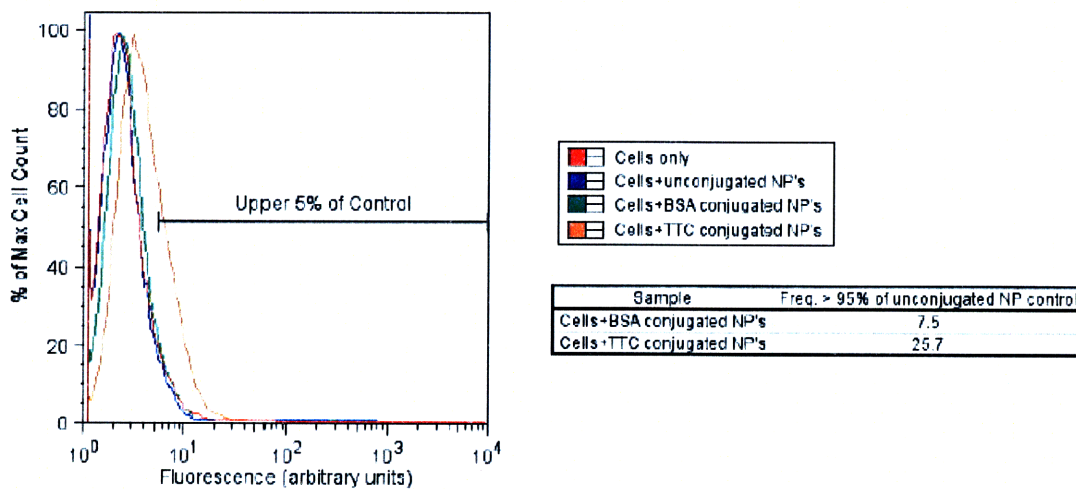


## Appendix O: Flow cytometry analysis of biotin binding proteins



## Appendix P: Cell binding of TTC-conjugated nanoparticles

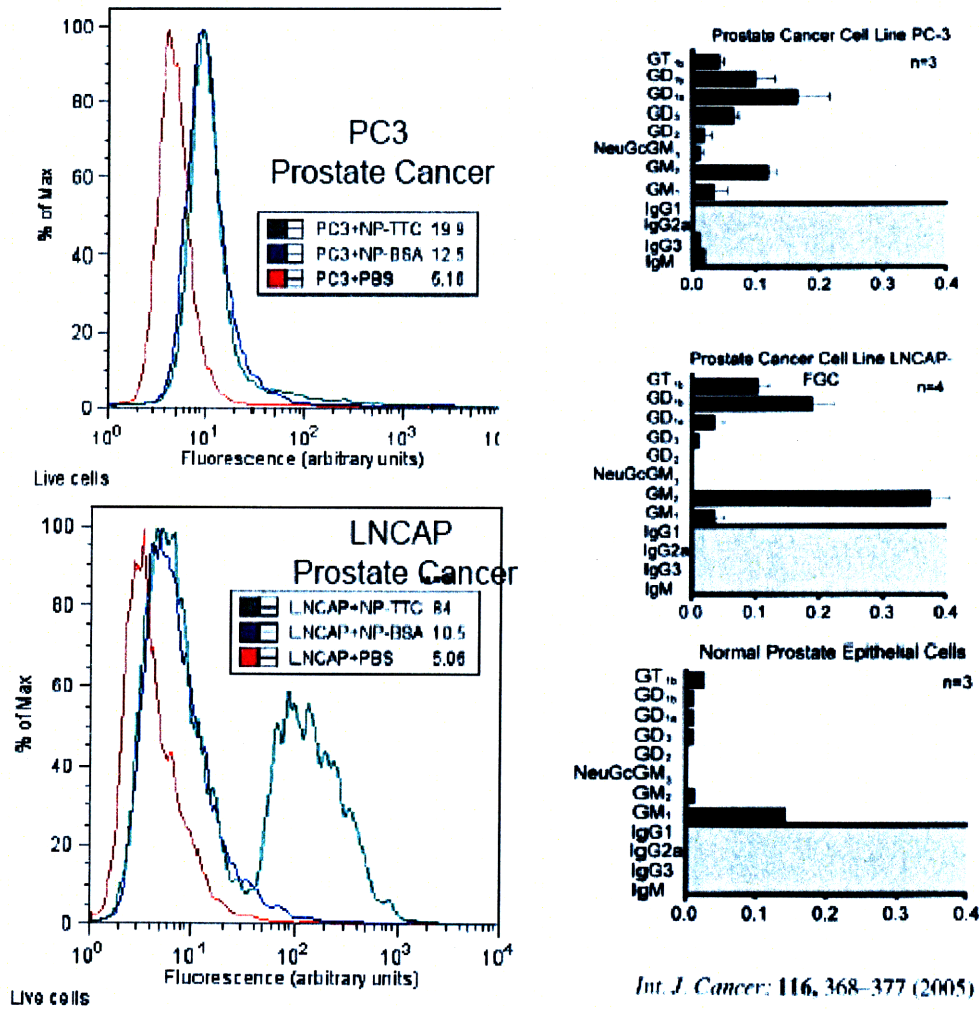
using NHS/EDC







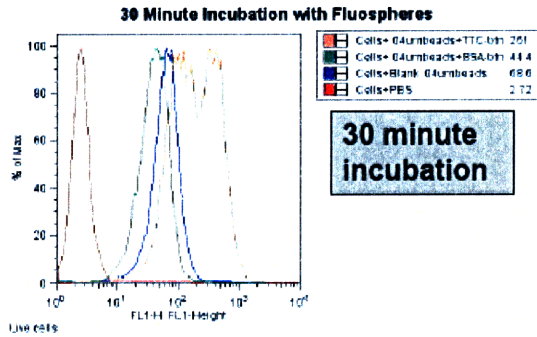
## Appendix Q: TTC nanoparticles binding to Prostate cancer



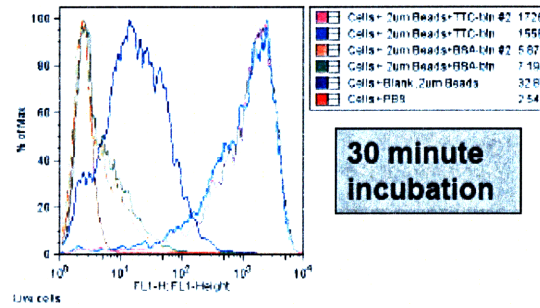


# Appendix R: TTC binding to neuroblastomas with polystyrene nanoparticles

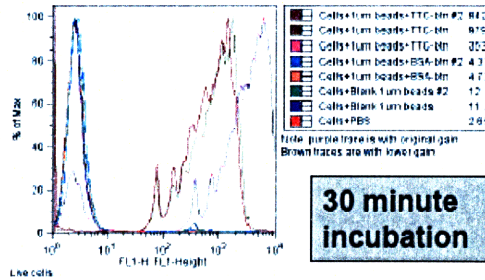
**40 nm beads**  
(~100nm in aqueous solution)



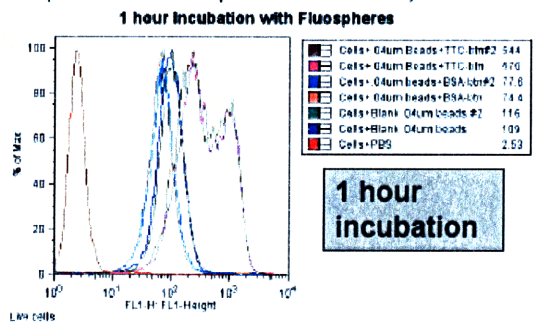
**200 nm beads**  
(~250nm in aqueous solution)



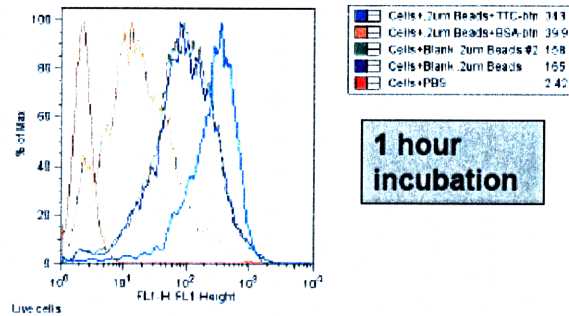
**1 micron beads**



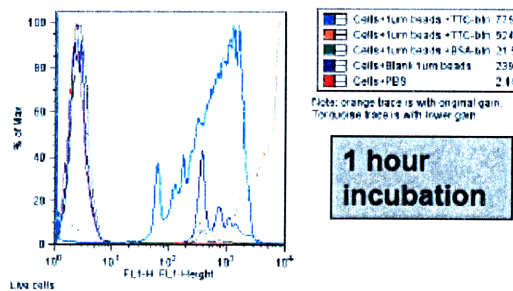
**40 nm beads**  
(~100nm in aqueous solution)



**200 nm beads**  
(~250nm in aqueous solution)

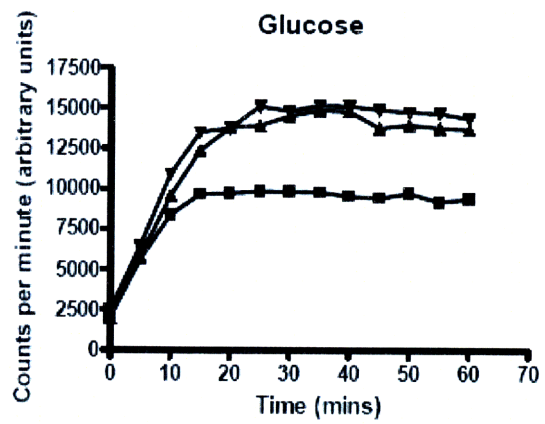
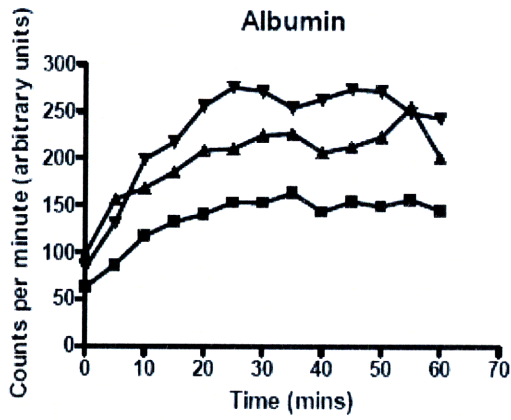
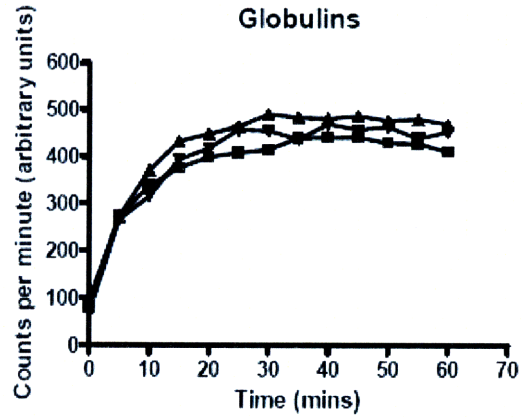
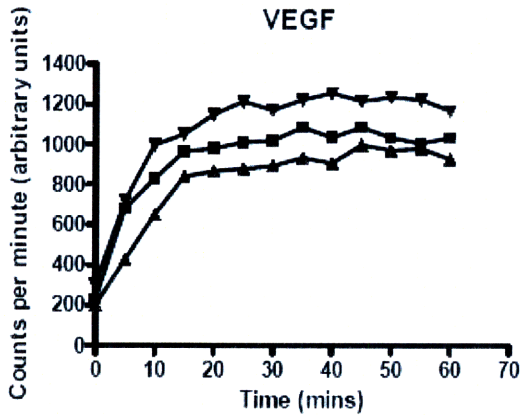
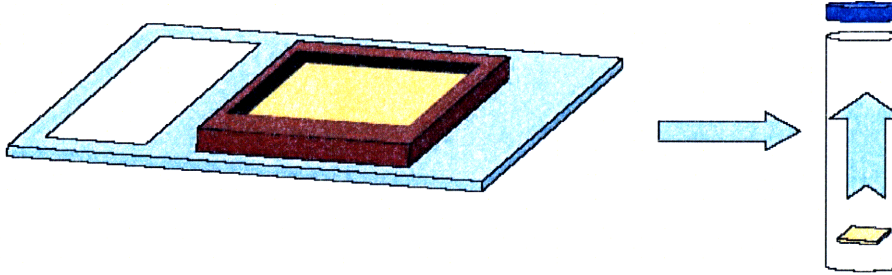


**1 micron beads**





# Appendix T: Diffusion through hydrogels





## Appendix T: Cancer Stem Cells

Researchers have suggested that normal stem cells may become cancer stem cells (CSCs) by either genotypic or phenotypic changes that could give rise to tumors <sup>221</sup>. They reason that normal stem cells share certain characteristics with cancer cells, specifically, high proliferation rates and immortality.

Alternatively, it has been postulated that cancer stem cells arise from progenitor cells that under normal conditions have a finite number of mitotic cycles, but acquire the ability to self-renew. Regardless of the source of CSC (which is still under debate and is a field of active research), investigators have identified a number of CSCs that share stem cell characteristics from humans, including hematopoietic <sup>222, 223</sup>, mammary <sup>224</sup>, prostate<sup>225</sup>, melanoma <sup>226</sup>, and brain <sup>227, 228</sup>.

Cells were isolated using fluorescence or magnetic techniques in these studies with markers that have previously been shown to be highly specific for stem cells.

Many of these cell lineages were capable of forming solid tumors, and could both provide new *in vitro* and *in vivo* models for cancer research and guide clinical therapeutic interventions. These topics are actively being researched and may provide insight into non-cancer applications such as neurodegenerative disease.

## Appendix U: References

1. Cudkowicz, M. E. et al. Trial of celecoxib in amyotrophic lateral sclerosis. *Ann Neurol* 60, 22-31 (2006).
2. DiBernardo, A. B. & Cudkowicz, M. E. Translating preclinical insights into effective human trials in ALS. *Biochim Biophys Acta* 1762, 1139-49 (2006).
3. Lindhorst, S. & Cudkowicz, M. Is pentoxifylline safe and effective in patients with amyotrophic lateral sclerosis? *Nat Clin Pract Neurol* 2, 364-5 (2006).
4. Traynor, B. J. et al. Neuroprotective agents for clinical trials in ALS: a systematic assessment. *Neurology* 67, 20-7 (2006).
5. Lechtzin, N. How beneficial is noninvasive ventilation in patients with amyotrophic lateral sclerosis? *Nat Clin Pract Neurol* 2, 356-7 (2006).
6. Lechtzin, N. Respiratory effects of amyotrophic lateral sclerosis: problems and solutions. *Respir Care* 51, 871-81; discussion 881-4 (2006).
7. Maragakis, N. J. & Rothstein, J. D. Mechanisms of Disease: astrocytes in neurodegenerative disease. *Nat Clin Pract Neurol* 2, 679-89 (2006).
8. Wong, P. C., Cai, H., Borchelt, D. R. & Price, D. L. Genetically engineered mouse models of neurodegenerative diseases. *Nat Neurosci* 5, 633-9 (2002).
9. Rosen, D. R. Mutations in Cu/Zn superoxide dismutase gene are associated with familial amyotrophic lateral sclerosis. *Nature* 364, 362 (1993).
10. Kirby, J. et al. Mutant SOD1 alters the motor neuronal transcriptome: implications for familial ALS. *Brain* 128, 1686-706 (2005).
11. Broom, W. J. et al. Variants in candidate ALS modifier genes linked to Cu/Zn superoxide dismutase do not explain divergent survival phenotypes. *Neurosci Lett* 392, 52-7 (2006).
12. Kawamata, C., Morita, M., Shibata, N. & Nakano, I. [Familial amyotrophic lateral sclerosis (FALS) with a novel SOD1 gene mutation: a clinicopathological study]. *Rinsho Shinkeigaku* 47, 211-6 (2007).
13. Zimmerman, M. C., Oberley, L. W. & Flanagan, S. W. Mutant SOD1-induced neuronal toxicity is mediated by increased mitochondrial superoxide levels. *J Neurochem* 102, 609-18 (2007).
14. Kunst, C. B., Mezey, E., Brownstein, M. J. & Patterson, D. Mutations in SOD1 associated with amyotrophic lateral sclerosis cause novel protein interactions. *Nat Genet* 15, 91-4 (1997).
15. Figlewicz, D. A. & Bird, T. D. "Pure" hereditary spastic paraplegias: the story becomes complicated. *Neurology* 53, 5-7 (1999).
16. Pasinelli, P. & Brown, R. H. Molecular biology of amyotrophic lateral sclerosis: insights from genetics. *Nat Rev Neurosci* 7, 710-23 (2006).
17. Shaw, P. J. Genetic inroads in familial ALS. *Nat Genet* 29, 103-4 (2001).
18. Dunussi-Joannopoulos, K., Weinstein, H. J., Arceci, R. J. & Croop, J. M. Gene therapy with B7.1 and GM-CSF vaccines in a murine AML model. *J Pediatr Hematol Oncol* 19, 536-40 (1997).
19. Haase, G. et al. Gene therapy of murine motor neuron disease using adenoviral vectors for neurotrophic factors. *Nat Med* 3, 429-36 (1997).



20. Aebischer, P. et al. Gene therapy for amyotrophic lateral sclerosis (ALS) using a polymer encapsulated xenogenic cell line engineered to secrete hCNTF. *Hum Gene Ther* 7, 851-60 (1996).
21. Miller, T. M. & Cleveland, D. W. Has gene therapy for ALS arrived? *Nat Med* 9, 1256-7 (2003).
22. Boillee, S. & Cleveland, D. W. Gene therapy for ALS delivers. *Trends Neurosci* 27, 235-8 (2004).
23. Azzouz, M. Gene Therapy for ALS: progress and prospects. *Biochim Biophys Acta* 1762, 1122-7 (2006).
24. Yokota, T. [Gene therapy of ALS with short interfering RNA]. *Brain Nerve* 59, 1187-94 (2007).
25. Ralph, G. S. et al. Silencing mutant SOD1 using RNAi protects against neurodegeneration and extends survival in an ALS model. *Nat Med* 11, 429-33 (2005).
26. Xie, J., Awad, K. S. & Guo, Q. RNAi knockdown of Par-4 inhibits neurosynaptic degeneration in ALS-linked mice. *J Neurochem* 92, 59-71 (2005).
27. Vila, M. & Przedborski, S. Targeting programmed cell death in neurodegenerative diseases. *Nat Rev Neurosci* 4, 365-75 (2003).
28. Anand, P. et al. Regional changes of ciliary neurotrophic factor and nerve growth factor levels in post mortem spinal cord and cerebral cortex from patients with motor disease. *Nat Med* 1, 168-72 (1995).
29. Subba Rao, K. Mechanisms of disease: DNA repair defects and neurological disease. *Nat Clin Pract Neurol* 3, 162-72 (2007).
30. Gros-Louis, F. et al. Absence of mutations in the hypoxia response element of VEGF in ALS. *Muscle Nerve* 28, 774-5 (2003).
31. Moreau, C. et al. Elevated IL-6 and TNF-alpha levels in patients with ALS: inflammation or hypoxia? *Neurology* 65, 1958-60 (2005).
32. Moreau, C. et al. Paradoxical response of VEGF expression to hypoxia in CSF of patients with ALS. *J Neurol Neurosurg Psychiatry* 77, 255-7 (2006).
33. Just, N. et al. High erythropoietin and low vascular endothelial growth factor levels in cerebrospinal fluid from hypoxemic ALS patients suggest an abnormal response to hypoxia. *Neuromuscul Disord* 17, 169-73 (2007).
34. Vande Velde, C. & Cleveland, D. W. VEGF: multitasking in ALS. *Nat Neurosci* 8, 5-7 (2005).
35. Storkebaum, E. et al. Treatment of motoneuron degeneration by intracerebroventricular delivery of VEGF in a rat model of ALS. *Nat Neurosci* 8, 85-92 (2005).
36. Kaspar, B. K., Llado, J., Sherkat, N., Rothstein, J. D. & Gage, F. H. Retrograde viral delivery of IGF-1 prolongs survival in a mouse ALS model. *Science* 301, 839-42 (2003).
37. Dobrowolny, G. et al. Muscle expression of a local Igf-1 isoform protects motor neurons in an ALS mouse model. *J Cell Biol* 168, 193-9 (2005).
38. Lepore, A. C. et al. Intraparenchymal spinal cord delivery of adeno-associated virus IGF-1 is protective in the SOD1G93A model of ALS. *Brain Res* 1185, 256-65 (2007).

39. Messi, M. L., Clark, H. M., Prevette, D. M., Oppenheim, R. W. & Delbono, O. The lack of effect of specific overexpression of IGF-1 in the central nervous system or skeletal muscle on pathophysiology in the G93A SOD-1 mouse model of ALS. *Exp Neurol* 207, 52-63 (2007).
40. Weinmann, H. J., Brasch, R. C., Press, W. R. & Wesbey, G. E. Characteristics of gadolinium-DTPA complex: a potential NMR contrast agent. *AJR Am J Roentgenol* 142, 619-24 (1984).
41. Laniado, M., Weinmann, H. J., Schorner, W., Felix, R. & Speck, U. First use of GdDTPA/dimeglumine in man. *Physiol Chem Phys Med NMR* 16, 157-65 (1984).
42. Widder, D. J., Greif, W. L., Widder, K. J., Edelman, R. R. & Brady, T. J. Magnetite albumin microspheres: a new MR contrast material. *AJR Am J Roentgenol* 148, 399-404 (1987).
43. Weissleder, R. et al. Ultrasmall superparamagnetic iron oxide: an intravenous contrast agent for assessing lymph nodes with MR imaging. *Radiology* 175, 494-8 (1990).
44. Weissleder, R., Reimer, P., Lee, A. S., Wittenberg, J. & Brady, T. J. MR receptor imaging: ultrasmall iron oxide particles targeted to asialoglycoprotein receptors. *AJR Am J Roentgenol* 155, 1161-7 (1990).
45. Daniel, K. D. et al. Multi-reservoir device for detecting a soluble cancer biomarker. *Lab Chip* 7, 1288-93 (2007).
46. Kim, G. Y., Josephson, L., Langer, R. & Cima, M. J. Magnetic relaxation switch detection of human chorionic gonadotrophin. *Bioconjug Chem* 18, 2024-8 (2007).
47. Matthews, P. M. & Talbot, K. Magnetic resonance spectroscopic imaging--of prognostic value in amyotrophic lateral sclerosis? *Nat Clin Pract Neurol* 3, 76-7 (2007).
48. Oberwittler, C., Masur, H., Ludolph, A. C. & Fahrenndorf, G. MRI in ALS. *Neurology* 42, 1641 (1992).
49. Midani, H., Truwit, C. L. & Parry, G. J. MRI in juvenile ALS: a patient report. *Neurology* 50, 1879-81 (1998).
50. Ellis, C. M. et al. Diffusion tensor MRI assesses corticospinal tract damage in ALS. *Neurology* 53, 1051-8 (1999).
51. Hecht, M. J. et al. MRI-FLAIR images of the head show corticospinal tract alterations in ALS patients more frequently than T2-, T1- and proton-density-weighted images. *J Neurol Sci* 186, 37-44 (2001).
52. Hecht, M. J. et al. Hyperintense and hypointense MRI signals of the precentral gyrus and corticospinal tract in ALS: a follow-up examination including FLAIR images. *J Neurol Sci* 199, 59-65 (2002).
53. Iwasaki, Y., Ikeda, K., Ichikawa, Y., Igarashi, O. & Kinoshita, M. MRI in ALS patients. *Acta Neurol Scand* 107, 426 (2003).
54. Lee, Y. C., Markus, R. & Hughes, A. MRI in ALS: corticospinal tract hyperintensity. *Neurology* 61, 1600 (2003).
55. Abe, K. MRI in ALS: corticospinal tract hyperintensity. *Neurology* 63, 596-7; author reply 596-7 (2004).
56. Angenstein, F. et al. Age-dependent changes in MRI of motor brain stem nuclei in a mouse model of ALS. *Neuroreport* 15, 2271-4 (2004).

57. Stommel, E. W. & Cohen, J. A. MRI in ALS: corticospinal tract hyperintensity. *Neurology* 63, 596-7; author reply 596-7 (2004).
58. Kassubek, J. et al. Global brain atrophy and corticospinal tract alterations in ALS, as investigated by voxel-based morphometry of 3-D MRI. *Amyotroph Lateral Scler Other Motor Neuron Disord* 6, 213-20 (2005).
59. Blain, C. R. et al. A longitudinal study of diffusion tensor MRI in ALS. *Amyotroph Lateral Scler*, 1-8 (2007).
60. Iwata, N. K. et al. Evaluation of corticospinal tracts in ALS with diffusion tensor MRI and brainstem stimulation. *Neurology* 70, 528-32 (2008).
61. Sivaraman, A. et al. A microscale in vitro physiological model of the liver: predictive screens for drug metabolism and enzyme induction. *Curr Drug Metab* 6, 569-91 (2005).
62. Brem, H. et al. Biocompatibility of a biodegradable, controlled-release polymer in the rabbit brain. *Sel Cancer Ther* 5, 55-65 (1989).
63. Kim, G. Y. et al. Resorbable polymer microchips releasing BCNU inhibit tumor growth in the rat 9L flank model. *J Control Release* 123, 172-8 (2007).
64. Langer, R., Brem, H. & Langer, L. F. New directions in CNS drug delivery. *Neurobiol Aging* 10, 642-4; discussion 648-50 (1989).
65. Langer, R., Brem, H. & Tapper, D. Biocompatibility of polymeric delivery systems for macromolecules. *J Biomed Mater Res* 15, 267-77 (1981).
66. Lesniak, M. S., Langer, R. & Brem, H. Drug delivery to tumors of the central nervous system. *Curr Neurol Neurosci Rep* 1, 210-6 (2001).
67. Li, Y. et al. In vivo delivery of BCNU from a MEMS device to a tumor model. *J Control Release* 106, 138-45 (2005).
68. Madrid, Y., Langer, L. F., Brem, H. & Langer, R. New directions in the delivery of drugs and other substances to the central nervous system. *Adv Pharmacol* 22, 299-324 (1991).
69. Langer, R. Drug delivery and targeting. *Nature* 392, 5-10 (1998).
70. Akinc, A., Anderson, D. G., Lynn, D. M. & Langer, R. Synthesis of poly(beta-amino ester)s optimized for highly effective gene delivery. *Bioconjug Chem* 14, 979-88 (2003).
71. Akinc, A., Lynn, D. M., Anderson, D. G. & Langer, R. Parallel synthesis and biophysical characterization of a degradable polymer library for gene delivery. *J Am Chem Soc* 125, 5316-23 (2003).
72. Anderson, D. G., Lynn, D. M. & Langer, R. Semi-automated synthesis and screening of a large library of degradable cationic polymers for gene delivery. *Angew Chem Int Ed Engl* 42, 3153-8 (2003).
73. Anderson, D. G. et al. A polymer library approach to suicide gene therapy for cancer. *Proc Natl Acad Sci U S A* 101, 16028-33 (2004).
74. Liu-Snyder, P. & Webster, T. J. Designing drug-delivery systems for the nervous system using nanotechnology: opportunities and challenges. *Expert Rev Med Devices* 3, 683-7 (2006).
75. Huynh, G. H., Deen, D. F. & Szoka, F. C., Jr. Barriers to carrier mediated drug and gene delivery to brain tumors. *J Control Release* 110, 236-59 (2006).

76. Pepinsky, R. B. et al. Improved pharmacokinetic properties of a polyethylene glycol-modified form of interferon-beta-1a with preserved in vitro bioactivity. *J Pharmacol Exp Ther* 297, 1059-66 (2001).
77. Calvo, P. et al. Long-circulating PEGylated polycyanoacrylate nanoparticles as new drug carrier for brain delivery. *Pharm Res* 18, 1157-66 (2001).
78. Ambruosi, A. et al. Biodistribution of polysorbate 80-coated doxorubicin-loaded [14C]-poly(butyl cyanoacrylate) nanoparticles after intravenous administration to glioblastoma-bearing rats. *J Drug Target* 14, 97-105 (2006).
79. Ambruosi, A., Yamamoto, H. & Kreuter, J. Body distribution of polysorbate-80 and doxorubicin-loaded [14C]poly(butyl cyanoacrylate) nanoparticles after i.v. administration in rats. *J Drug Target* 13, 535-42 (2005).
80. Alyautdin, R. N. et al. Delivery of loperamide across the blood-brain barrier with polysorbate 80-coated polybutylcyanoacrylate nanoparticles. *Pharm Res* 14, 325-8 (1997).
81. Gulyaev, A. E. et al. Significant transport of doxorubicin into the brain with polysorbate 80-coated nanoparticles. *Pharm Res* 16, 1564-9 (1999).
82. Silva, G. A. Nanotechnology approaches for drug and small molecule delivery across the blood brain barrier. *Surg Neurol* 67, 113-6 (2007).
83. Olivier, J. C. et al. Indirect evidence that drug brain targeting using polysorbate 80-coated polybutylcyanoacrylate nanoparticles is related to toxicity. *Pharm Res* 16, 1836-42 (1999).
84. Benn, S. C. et al. Tetanus toxin fragment C fusion facilitates protein delivery to CNS neurons from cerebrospinal fluid in mice. *J Neurochem* 95, 1118-31 (2005).
85. Townsend, S. A. et al. Tetanus toxin C fragment-conjugated nanoparticles for targeted drug delivery to neurons. *Biomaterials* 28, 5176-84 (2007).
86. Collard, J. F., Cote, F. & Julien, J. P. Defective axonal transport in a transgenic mouse model of amyotrophic lateral sclerosis. *Nature* 375, 61-4 (1995).
87. Breuer, A. C. & Atkinson, M. B. Fast axonal transport alterations in amyotrophic lateral sclerosis (ALS) and in parathyroid hormone (PTH)-treated axons. *Cell Motil Cytoskeleton* 10, 321-30 (1988).
88. Williamson, T. L. & Cleveland, D. W. Slowing of axonal transport is a very early event in the toxicity of ALS-linked SOD1 mutants to motor neurons. *Nat Neurosci* 2, 50-6 (1999).
89. Guo, Z., Kindy, M. S., Kruman, I. & Mattson, M. P. ALS-linked Cu/Zn-SOD mutation impairs cerebral synaptic glucose and glutamate transport and exacerbates ischemic brain injury. *J Cereb Blood Flow Metab* 20, 463-8 (2000).
90. Kieran, D. et al. A mutation in dynein rescues axonal transport defects and extends the life span of ALS mice. *J Cell Biol* 169, 561-7 (2005).
91. Tovar-y-Romo, L. B. & Tapia, R. Cerebral neurons of transgenic ALS mice are vulnerable to glutamate release stimulation but not to increased extracellular glutamate due to transport blockade. *Exp Neurol* 199, 281-90 (2006).
92. Bock, N. A., Paiva, F. F., Nascimento, G. C., Newman, J. D. & Silva, A. C. Cerebrospinal fluid to brain transport of manganese in a non-human primate revealed by MRI. *Brain Res* 1198, 160-70 (2008).

93. Mimeault, M. & Batra, S. K. Concise review: recent advances on the significance of stem cells in tissue regeneration and cancer therapies. *Stem Cells* 24, 2319-45 (2006).
94. Di Giorgio, F. P., Carrasco, M. A., Siao, M. C., Maniatis, T. & Eggan, K. Non-cell autonomous effect of glia on motor neurons in an embryonic stem cell-based ALS model. *Nat Neurosci* 10, 608-14 (2007).
95. Levenberg, S., Burdick, J. A., Kraehenbuehl, T. & Langer, R. Neurotrophin-induced differentiation of human embryonic stem cells on three-dimensional polymeric scaffolds. *Tissue Eng* 11, 506-12 (2005).
96. Levenberg, S. et al. Differentiation of human embryonic stem cells on three-dimensional polymer scaffolds. *Proc Natl Acad Sci U S A* 100, 12741-6 (2003).
97. Chung, B. G. et al. Human neural stem cell growth and differentiation in a gradient-generating microfluidic device. *Lab Chip* 5, 401-6 (2005).
98. Papanikolaou, T. et al. In vitro generation of dopaminergic neurons from adult subventricular zone neural progenitor cells. *Stem Cells Dev* 17, 157-72 (2008).
99. Galli, R., Gritti, A., Bonfanti, L. & Vescovi, A. L. Neural stem cells: an overview. *Circ Res* 92, 598-608 (2003).
100. Kennea, N. L. & Mehmet, H. Neural stem cells. *J Pathol* 197, 536-50 (2002).
101. Rappa, G. et al. Efficient expansion and gene transduction of mouse neural stem/progenitor cells on recombinant fibronectin. *Neuroscience* 124, 823-30 (2004).
102. Yamada, M., Uchida, K., Hayashi, T., Mine, Y. & Kawase, T. Vigorous neuronal differentiation of amplified and grafted basic fibroblast growth factor-responsive neurospheres derived from neuroepithelial stem cells. *Cell Transplant* 13, 421-8 (2004).
103. Gotz, M. & Barde, Y. A. Radial glial cells defined and major intermediates between embryonic stem cells and CNS neurons. *Neuron* 46, 369-72 (2005).
104. Vazin, T., Chen, J., Lee, C. T., Amable, R. & Freed, W. J. Assessment of Stromal-Derived Inducing Activity in the Generation of Dopaminergic Neurons from Human Embryonic Stem Cells. *Stem Cells* (2008).
105. Gerecht, S. et al. Hyaluronic acid hydrogel for controlled self-renewal and differentiation of human embryonic stem cells. *Proc Natl Acad Sci U S A* 104, 11298-303 (2007).
106. Svendsen, C. N. & Langston, J. W. Stem cells for Parkinson disease and ALS: replacement or protection? *Nat Med* 10, 224-5 (2004).
107. Vastag, B. Stem cells step closer to the clinic: paralysis partially reversed in rats with ALS-like disease. *Jama* 285, 1691-3 (2001).
108. Lepore, A. C. et al. Long-term fate of neural precursor cells following transplantation into developing and adult CNS. *Neuroscience* 142, 287-304 (2006).
109. Yan, J. et al. Extensive neuronal differentiation of human neural stem cell grafts in adult rat spinal cord. *PLoS Med* 4, e39 (2007).
110. Horner, P. J. et al. Proliferation and differentiation of progenitor cells throughout the intact adult rat spinal cord. *J Neurosci* 20, 2218-28 (2000).

111. Chi, L., Gan, L., Luo, C., Lien, L. & Liu, R. Temporal response of neural progenitor cells to disease onset and progression in amyotrophic lateral sclerosis-like transgenic mice. *Stem Cells Dev* 16, 579-88 (2007).
112. Hedlund, E., Hefferan, M. P., Marsala, M. & Isacson, O. Cell therapy and stem cells in animal models of motor neuron disorders. *Eur J Neurosci* 26, 1721-37 (2007).
113. Ziv, Y., Avidan, H., Pluchino, S., Martino, G. & Schwartz, M. Synergy between immune cells and adult neural stem/progenitor cells promotes functional recovery from spinal cord injury. *Proc Natl Acad Sci U S A* 103, 13174-9 (2006).
114. Silani, V., Cova, L., Corbo, M., Ciammola, A. & Polli, E. Stem-cell therapy for amyotrophic lateral sclerosis. *Lancet* 364, 200-2 (2004).
115. Suzuki, M. & Svendsen, C. N. Combining growth factor and stem cell therapy for amyotrophic lateral sclerosis. *Trends Neurosci* (2008).
116. Elisseeff, J., Ferran, A., Hwang, S., Varghese, S. & Zhang, Z. The role of biomaterials in stem cell differentiation: applications in the musculoskeletal system. *Stem Cells Dev* 15, 295-303 (2006).
117. Cimetta, E. et al. Enhancement of viability of muscle precursor cells on 3D scaffold in a perfusion bioreactor. *Int J Artif Organs* 30, 415-28 (2007).
118. Vunjak-Novakovic, G. et al. Dynamic cell seeding of polymer scaffolds for cartilage tissue engineering. *Biotechnol Prog* 14, 193-202 (1998).
119. Dar, A., Shachar, M., Leor, J. & Cohen, S. Optimization of cardiac cell seeding and distribution in 3D porous alginate scaffolds. *Biotechnol Bioeng* 80, 305-12 (2002).
120. Alvarez-Barreto, J. F., Linehan, S. M., Shambaugh, R. L. & Sikavitsas, V. I. Flow perfusion improves seeding of tissue engineering scaffolds with different architectures. *Ann Biomed Eng* 35, 429-42 (2007).
121. Wang, Y., Ameer, G. A., Sheppard, B. J. & Langer, R. A tough biodegradable elastomer. *Nat Biotechnol* 20, 602-6 (2002).
122. Wang, Y., Kim, Y. M. & Langer, R. In vivo degradation characteristics of poly(glycerol sebacate). *J Biomed Mater Res A* 66, 192-7 (2003).
123. Maxwell, M. M., Pasinelli, P., Kazantsev, A. G. & Brown, R. H., Jr. RNA interference-mediated silencing of mutant superoxide dismutase rescues cyclosporin A-induced death in cultured neuroblastoma cells. *Proc Natl Acad Sci U S A* 101, 3178-83 (2004).
124. Raoul, C. et al. Lentiviral-mediated silencing of SOD1 through RNA interference retards disease onset and progression in a mouse model of ALS. *Nat Med* 11, 423-8 (2005).
125. Miller, R. G., Mitchell, J. D., Lyon, M. & Moore, D. H. Riluzole for amyotrophic lateral sclerosis (ALS)/motor neuron disease (MND). *Cochrane Database Syst Rev*, CD001447 (2002).
126. Miller, R. G., Mitchell, J. D., Lyon, M. & Moore, D. H. Riluzole for amyotrophic lateral sclerosis (ALS)/motor neuron disease (MND). *Amyotroph Lateral Scler Other Motor Neuron Disord* 4, 191-206 (2003).
127. Miller, R. G., Mitchell, J. D., Lyon, M. & Moore, D. H. Riluzole for amyotrophic lateral sclerosis (ALS)/motor neuron disease (MND). *Cochrane Database Syst Rev*, CD001447 (2007).

128. Bonifacino, J. S. & Rojas, R. Retrograde transport from endosomes to the trans-Golgi network. *Nat Rev Mol Cell Biol* 7, 568-79 (2006).
129. Hyams, J. S. Organelle transport: retrograde step for microtubules. *Nature* 330, 106 (1987).
130. Hendry, I. A. & Hill, C. E. Retrograde axonal transport of target tissue-derived macromolecules. *Nature* 287, 647-9 (1980).
131. Banks, P. Retrograde transport in axons. *Nature* 287, 12-3 (1980).
132. Bilgen, M., Al-Hafez, B., Berman, N. E. & Festoff, B. W. Magnetic resonance imaging of mouse spinal cord. *Magn Reson Med* 54, 1226-31 (2005).
133. Bonny, J. M. et al. Nuclear magnetic resonance microimaging of mouse spinal cord in vivo. *Neurobiol Dis* 15, 474-82 (2004).
134. Herborn, C. U. et al. Clinical safety and diagnostic value of the gadolinium chelate gadoterate meglumine (Gd-DOTA). *Invest Radiol* 42, 58-62 (2007).
135. Marzella, L., Blank, M., Gelperin, K. & Johann-Liang, R. Safety risks with gadolinium-based contrast agents. *J Magn Reson Imaging* 26, 816; author reply 817 (2007).
136. Pedersen, M. Safety update on the possible causal relationship between gadolinium-containing MRI agents and nephrogenic systemic fibrosis. *J Magn Reson Imaging* 25, 881-3 (2007).
137. Francis, J. W. et al. Tetanus toxin fragment C as a vector to enhance delivery of proteins to the CNS. *Brain Res* 1011, 7-13 (2004).
138. Francis, J. W. et al. A survival motor neuron:tetanus toxin fragment C fusion protein for the targeted delivery of SMN protein to neurons. *Brain Res* 995, 84-96 (2004).
139. Francis, J. W., Hosler, B. A., Brown, R. H., Jr. & Fishman, P. S. CuZn superoxide dismutase (SOD-1):tetanus toxin fragment C hybrid protein for targeted delivery of SOD-1 to neuronal cells. *J Biol Chem* 270, 15434-42 (1995).
140. Alexander, G. M. et al. Effect of transgene copy number on survival in the G93A SOD1 transgenic mouse model of ALS. *Brain Res Mol Brain Res* 130, 7-15 (2004).
141. Heiman-Patterson, T. D. et al. Background and gender effects on survival in the TgN(SOD1-G93A)1Gur mouse model of ALS. *J Neurol Sci* 236, 1-7 (2005).
142. Matsumoto, A. et al. Disease progression of human SOD1 (G93A) transgenic ALS model rats. *J Neurosci Res* 83, 119-33 (2006).
143. Miana-Mena, F. J. et al. Optimal methods to characterize the G93A mouse model of ALS. *Amyotroph Lateral Scler Other Motor Neuron Disord* 6, 55-62 (2005).
144. Nobs, L., Buchegger, F., Gurny, R. & Allemann, E. Poly(lactic acid) nanoparticles labeled with biologically active Neutravidin for active targeting. *Eur J Pharm Biopharm* 58, 483-90 (2004).
145. Nobs, L., Buchegger, F., Gurny, R. & Allemann, E. Biodegradable nanoparticles for direct or two-step tumor immunotargeting. *Bioconjug Chem* 17, 139-45 (2006).
146. Gref, R., Couvreur, P., Barratt, G. & Mysiakine, E. Surface-engineered nanoparticles for multiple ligand coupling. *Biomaterials* 24, 4529-37 (2003).
147. Cannizzaro, S. M. et al. A novel biotinylated degradable polymer for cell-interactive applications. *Biotechnol Bioeng* 58, 529-35 (1998).

148. Weiss, B. et al. Coupling of Biotin-(poly(ethylene glycol))amine to Poly(D,L-lactide-co-glycolide) Nanoparticles for Versatile Surface Modification. *Bioconjug Chem* (2007).
149. Ben-Shabat, S., Kumar, N. & Domb, A. J. PEG-PLA block copolymer as potential drug carrier: preparation and characterization. *Macromol Biosci* 6, 1019-25 (2006).
150. Fischer, S., Foerg, C., Ellenberger, S., Merkle, H. P. & Gander, B. One-step preparation of polyelectrolyte-coated PLGA microparticles and their functionalization with model ligands. *J Control Release* 111, 135-44 (2006).
151. Pardridge, W. M. Blood-brain barrier delivery. *Drug Discov Today* 12, 54-61 (2007).
152. Kreuter, J. Nanoparticulate systems for brain delivery of drugs. *Adv Drug Deliv Rev* 47, 65-81 (2001).
153. Shi, N., Zhang, Y., Zhu, C., Boado, R. J. & Pardridge, W. M. Brain-specific expression of an exogenous gene after i.v. administration. *Proc Natl Acad Sci U S A* 98, 12754-9 (2001).
154. Lalli, G. & Schiavo, G. Analysis of retrograde transport in motor neurons reveals common endocytic carriers for tetanus toxin and neurotrophin receptor p75NTR. *J Cell Biol* 156, 233-9 (2002).
155. Shapiro, R. E. et al. Identification of a ganglioside recognition domain of tetanus toxin using a novel ganglioside photoaffinity ligand. *J Biol Chem* 272, 30380-6 (1997).
156. Sinha, K. et al. Analysis of mutants of tetanus toxin Hc fragment: ganglioside binding, cell binding and retrograde axonal transport properties. *Mol Microbiol* 37, 1041-51 (2000).
157. Panyam, J., Sahoo, S. K., Prabha, S., Bargar, T. & Labhasetwar, V. Fluorescence and electron microscopy probes for cellular and tissue uptake of poly(D,L-lactide-co-glycolide) nanoparticles. *Int J Pharm* 262, 1-11 (2003).
158. Cheng, J. et al. Formulation of functionalized PLGA-PEG nanoparticles for in vivo targeted drug delivery. *Biomaterials* 28, 869-76 (2007).
159. Fasman, D. G. *Practical Handbook of Biochemistry and Molecular Biology* (CRC Press, Boston, 1992).
160. Malouf, A. T., Schnaar, R. L. & Coyle, J. T. Characterization of a glutamic acid neurotransmitter binding site on neuroblastoma hybrid cells. *J Biol Chem* 259, 12756-62 (1984).
161. Lewis, W. et al. Fialuridine and its metabolites inhibit DNA polymerase gamma at sites of multiple adjacent analog incorporation, decrease mtDNA abundance, and cause mitochondrial structural defects in cultured hepatoblasts. *Proc Natl Acad Sci U S A* 93, 3592-7 (1996).
162. Piro, O. & Broze, G. J., Jr. Role for the Kunitz-3 domain of tissue factor pathway inhibitor-alpha in cell surface binding. *Circulation* 110, 3567-72 (2004).
163. Knapp, M., Segelke, B. & Rupp, B. The 1.61 Angstrom Structure of the Tetanus Toxin Ganglioside Binding Region: Solved by MAD and Mir Phase Combination. *Am. Crystallogr. Assoc.* 25, 90 (1998).
164. Chen, J. et al. MMDB: Entrez's 3D-structure database. *Nucleic Acids Res* 31, 474-7 (2003).



165. Pugliese, L., Coda, A., Malcovati, M. & Bolognesi, M. Three-dimensional structure of the tetragonal crystal form of egg-white avidin in its functional complex with biotin at 2.7 Å resolution. *J Mol Biol* 231, 698-710 (1993).
166. Costanzo, P. J., Patten, T. E. & Seery, T. A. Nanoparticle agglutination: acceleration of aggregation rates and broadening of the analyte concentration range using mixtures of various-sized nanoparticles. *Langmuir* 22, 2788-94 (2006).
167. Costanzo, P. J., Patten, T. E. & Seery, T. A. Protein-Ligand Mediated Aggregation of Nanoparticles: A Study of Synthesis and Assembly Mechanism. *Chem. Mater.* 16, 1775 -1785 (2004).
168. Farokhzad, O. C. et al. Targeted nanoparticle-aptamer bioconjugates for cancer chemotherapy in vivo. *Proc Natl Acad Sci U S A* 103, 6315-20 (2006).
169. Farokhzad, O. C. et al. Nanoparticle-aptamer bioconjugates: a new approach for targeting prostate cancer cells. *Cancer Res* 64, 7668-72 (2004).
170. Zhou, W. et al. Efficient intracellular delivery of oligonucleotides formulated in folate receptor-targeted lipid vesicles. *Bioconjug Chem* 13, 1220-5 (2002).
171. Gref, R. et al. Biodegradable long-circulating polymeric nanospheres. *Science* 263, 1600-3 (1994).
172. Gerecht, S. et al. A porous photocurable elastomer for cell encapsulation and culture. *Biomaterials* 28, 4826-35 (2007).
173. Abbott, A. Cell culture: biology's new dimension. *Nature* 424, 870-2 (2003).
174. Postovit, L. M., Seftor, E. A., Seftor, R. E. & Hendrix, M. J. A three-dimensional model to study the epigenetic effects induced by the microenvironment of human embryonic stem cells. *Stem Cells* 24, 501-5 (2006).
175. Lee, G. Y., Kenny, P. A., Lee, E. H. & Bissell, M. J. Three-dimensional culture models of normal and malignant breast epithelial cells. *Nat Methods* 4, 359-65 (2007).
176. Debnath, J. & Brugge, J. S. Modelling glandular epithelial cancers in three-dimensional cultures. *Nat Rev Cancer* 5, 675-88 (2005).
177. Ingber, D. E. Cellular mechanotransduction: putting all the pieces together again. *Faseb J* 20, 811-27 (2006).
178. Heidemann, S. R. & Wirtz, D. Towards a regional approach to cell mechanics. *Trends Cell Biol* 14, 160-6 (2004).
179. Gerecht-Nir, S. & Itskovitz-Eldor, J. Human embryonic stem cells: a potential source for cellular therapy. *Am J Transplant* 4 Suppl 6, 51-7 (2004).
180. Weissman, I. L. Translating stem and progenitor cell biology to the clinic: barriers and opportunities. *Science* 287, 1442-6 (2000).
181. Taqvi, S. & Roy, K. Influence of scaffold physical properties and stromal cell coculture on hematopoietic differentiation of mouse embryonic stem cells. *Biomaterials* 27, 6024-31 (2006).
182. Lutolf, M. P. & Hubbell, J. A. Synthetic biomaterials as instructive extracellular microenvironments for morphogenesis in tissue engineering. *Nat Biotechnol* 23, 47-55 (2005).
183. Haines-Butterick, L. et al. Controlling hydrogelation kinetics by peptide design for three-dimensional encapsulation and injectable delivery of cells. *Proc Natl Acad Sci U S A* 104, 7791-6 (2007).

184. Cushing, M. C. & Anseth, K. S. Materials science. Hydrogel cell cultures. *Science* 316, 1133-4 (2007).
185. Webb, A. R., Yang, J. & Ameer, G. A. Biodegradable polyester elastomers in tissue engineering. *Expert Opin Biol Ther* 4, 801-12 (2004).
186. Nijst, C. L. E. et al. (2007).
187. Drury, J. L. & Mooney, D. J. Hydrogels for tissue engineering: scaffold design variables and applications. *Biomaterials* 24, 4337-51 (2003).
188. Ferreira, L. S. et al. Bioactive hydrogel scaffolds for controllable vascular differentiation of human embryonic stem cells. *Biomaterials* (2007).
189. Gerecht, S. et al. (2007).
190. Chung, C. et al. Effects of auricular chondrocyte expansion on neocartilage formation in photocrosslinked hyaluronic acid networks. *Tissue Eng* 12, 2665-73 (2006).
191. Burdick, J. A. & Anseth, K. S. Photoencapsulation of osteoblasts in injectable RGD-modified PEG hydrogels for bone tissue engineering. *Biomaterials* 23, 4315-23 (2002).
192. Burdick, J. A., Chung, C., Jia, X., Randolph, M. A. & Langer, R. Controlled degradation and mechanical behavior of photopolymerized hyaluronic acid networks. *Biomacromolecules* 6, 386-91 (2005).
193. Amit, M. et al. Clonally derived human embryonic stem cell lines maintain pluripotency and proliferative potential for prolonged periods of culture. *Dev Biol* 227, 271-8 (2000).
194. Guillaume, D. J., Johnson, M. A., Li, X. J. & Zhang, S. C. Human embryonic stem cell-derived neural precursors develop into neurons and integrate into the host brain. *J Neurosci Res* 84, 1165-76 (2006).
195. Sumida, S. Transfusion and transplantation of cryopreserved cells and tissues. *Cell Tissue Bank* 7, 265-305 (2006).
196. Engler, A. J., Sen, S., Sweeney, H. L. & Discher, D. E. Matrix elasticity directs stem cell lineage specification. *Cell* 126, 677-89 (2006).
197. Sundback, C. A. et al. Biocompatibility analysis of poly(glycerol sebacate) as a nerve guide material. *Biomaterials* 26, 5454-64 (2005).
198. Low, J. A., Magnuson, B., Tsai, B. & Imperiale, M. J. Identification of gangliosides GD1b and GT1b as receptors for BK virus. *J Virol* 80, 1361-6 (2006).
199. Zhang, Y., Schlachetzki, F. & Pardridge, W. M. Global non-viral gene transfer to the primate brain following intravenous administration. *Mol Ther* 7, 11-8 (2003).
200. Shi, N. & Pardridge, W. M. Noninvasive gene targeting to the brain. *Proc Natl Acad Sci U S A* 97, 7567-72 (2000).
201. Riviere, C. et al. Magnetic targeting of nanometric magnetic fluid loaded liposomes to specific brain intravascular areas: a dynamic imaging study in mice. *Radiology* 244, 439-48 (2007).
202. John, M. et al. Effective RNAi-mediated gene silencing without interruption of the endogenous microRNA pathway. *Nature* 449, 745-7 (2007).
203. Gu, F. et al. From the Cover: Precise engineering of targeted nanoparticles by using self-assembled biointegrated block copolymers. *Proc Natl Acad Sci U S A* 105, 2586-91 (2008).

204. Sheehan, D. C. & Hrapchak, B. B. Theory and practice of histotechnology (Mosby, St. Louis, 1980).
205. Gerami-Naini, B. et al. Trophoblast differentiation in embryoid bodies derived from human embryonic stem cells. *Endocrinology* 145, 1517-24 (2004).
206. Liu, H., Collins, S. F. & Suggs, L. J. Three-dimensional culture for expansion and differentiation of mouse embryonic stem cells. *Biomaterials* 27, 6004-14 (2006).
207. Kleinman, H. K., Philp, D. & Hoffman, M. P. Role of the extracellular matrix in morphogenesis. *Curr Opin Biotechnol* 14, 526-32 (2003).
208. Battista, S. et al. The effect of matrix composition of 3D constructs on embryonic stem cell differentiation. *Biomaterials* 26, 6194-207 (2005).
209. Philp, D. et al. Complex extracellular matrices promote tissue-specific stem cell differentiation. *Stem Cells* 23, 288-96 (2005).
210. Mohr, J. C., de Pablo, J. J. & Palecek, S. P. 3-D microwell culture of human embryonic stem cells. *Biomaterials* 27, 6032-42 (2006).
211. Liu, H., Lin, J. & Roy, K. Effect of 3D scaffold and dynamic culture condition on the global gene expression profile of mouse embryonic stem cells. *Biomaterials* 27, 5978-89 (2006).
212. Zhang, S. Designer self-assembling Peptide nanofiber scaffolds for study of 3-d cell biology and beyond. *Adv Cancer Res* 99, 335-62 (2008).
213. Zhang, S., Gelain, F. & Zhao, X. Designer self-assembling peptide nanofiber scaffolds for 3D tissue cell cultures. *Semin Cancer Biol* 15, 413-20 (2005).
214. Pacary, E. et al. Synergistic effects of CoCl<sub>2</sub> and ROCK inhibition on mesenchymal stem cell differentiation into neuron-like cells. *J Cell Sci* 119, 2667-78 (2006).
215. Rawal, N., Parish, C., Castelo-Branco, G. & Arenas, E. Inhibition of JNK increases survival of transplanted dopamine neurons in Parkinsonian rats. *Cell Death Differ* 14, 381-3 (2007).
216. Ma, W. et al. CNS stem and progenitor cell differentiation into functional neuronal circuits in three-dimensional collagen gels. *Exp Neurol* 190, 276-88 (2004).
217. Ning, H., Lin, G., Lue, T. F. & Lin, C. S. Neuron-like differentiation of adipose tissue-derived stromal cells and vascular smooth muscle cells. *Differentiation* 74, 510-8 (2006).
218. Kleinman, H. K. & Martin, G. R. Matrigel: basement membrane matrix with biological activity. *Semin Cancer Biol* 15, 378-86 (2005).
219. Notarianni, E. & Evans, M. J. Embryonic stem cells : a practical approach (Oxford University Press, Oxford ; New York, 2006).
220. Feraud, O., Debili, N., Penninger, J. M. & Kroemer, G. Cavitation of embryoid bodies requires optimal oxidative phosphorylation and AIF. *Cell Death Differ* 14, 385-7 (2007).
221. Tan, B. T., Park, C. Y., Ailles, L. E. & Weissman, I. L. The cancer stem cell hypothesis: a work in progress. *Lab Invest* 86, 1203-7 (2006).
222. Bonnet, D. & Dick, J. E. Human acute myeloid leukemia is organized as a hierarchy that originates from a primitive hematopoietic cell. *Nat Med* 3, 730-7 (1997).

223. Lapidot, T. et al. A cell initiating human acute myeloid leukaemia after transplantation into SCID mice. *Nature* 367, 645-8 (1994).
224. Al-Hajj, M., Wicha, M. S., Benito-Hernandez, A., Morrison, S. J. & Clarke, M. F. Prospective identification of tumorigenic breast cancer cells. *Proc Natl Acad Sci U S A* 100, 3983-8 (2003).
225. Collins, A. T., Berry, P. A., Hyde, C., Stower, M. J. & Maitland, N. J. Prospective identification of tumorigenic prostate cancer stem cells. *Cancer Res* 65, 10946-51 (2005).
226. Fang, D. et al. A tumorigenic subpopulation with stem cell properties in melanomas. *Cancer Res* 65, 9328-37 (2005).
227. Hemmati, H. D. et al. Cancerous stem cells can arise from pediatric brain tumors. *Proc Natl Acad Sci U S A* 100, 15178-83 (2003).
228. Singh, S. K. et al. Identification of a cancer stem cell in human brain tumors. *Cancer Res* 63, 5821-8 (2003).